UNIVERSITY OF ADELAIDE LIBRARY 16/4/07



THE UNIVERSITY OF ADELAIDE
AUSTRALIA

Numerical Optimisation of Biomedical Implant Characteristics for Increased Service Life

David S. Thompson

B.E. Hons (Adelaide), 2000.

School of Mechanical Engineering

The University of Adelaide

South Australia 5005

Submitted for the degree of Doctor of Philosophy on the 1st of March 2006.

ABSTRACT

The research presented in this thesis focuses on the development of a numerical optimisation technique with the aim to decrease implant stress shielding which in turn could increase Total Hip Arthroplasty (THA) service life and reduce patient discomfort by employing a distributed stiffness along implant length.

THA is a frequently performed operation, in which the natural hip joint is replaced with a mechanical joint that requires implantation of a 'stem' within the femoral shaft. While THA is generally regarded as a successful method of restoring limb function, it is possible to improve current implant design and consequently increase service life to accommodate increasing human life expectancy and the decreasing age of THA recipients.

Initially, various numerical models of intact femora are constructed and studied in order to obtain an appreciation of the parameters (such as loading and boundary conditions) that influence solution accuracy. The results of which are the generation of accurate and efficient intact femoral numerical models, based on extracted cadaveric specimens.

Commercially available THA stems are assessed for their stress shielding (reduction in stress level post implantation) characteristics using the parameters specified within the previously constructed intact numerical models. The implanted femoral model containing the THA stem that demonstrated the most favourable stress shielding characteristics was used as a platform for numerical optimisation techniques.

Numerical optimisation techniques were applied to the implanted femoral model to generate homogeneous and distributed THA stem stiffness values that minimised stress shielding without exceeding maximum allowable stresses within the cement, which acts to locate and restrain the implanted THA stem.

The research presented here has found that through distributing stiffness along THA stem length, significant reductions in stress shielding can be achieved without exceeding maximum allowable stresses within the cement, possibly extending service life in comparison to homogeneous THA stems.

CONTENTS

ABSTRACT i

CONTENTS iii

LIST OF FIGURES AND TABLES ix

STATEMENT OF ORIGINALITY xv

ACKNOWLEDGEMENTS xvi

Chapter 1

INTRODUCTION 1

1.1 Total Hip Arthroplasty (THA) 1

1.1.1 Problems Associated with THA 2

1.2 THA Medical Procedure 4

1.3 Significance and Motivation 6

Chapter 2

LITERATURE REVIEW 9

2.1 THA Femoral Implant Characteristics 9

2.1.1 Cemented THA Stem Implantation 10

2.1.2 Cementless THA Stem Implantation 12

2.1.3 THA Stem Surface Finish and Implications in Cemented THA 13

2.1.4 Material Biocompatibility 17

2.1.5 Advances in THA Stem Design 18

2.2 Characteristics of Bone Material 20

2.2.1 Compact Bone Material Characteristics 21

2.2.2 Cancellous Bone Characteristics 23
2.2.2.1 Structure 23
2.2.2.2 Mechanical Properties 24
2.3 Numerical Models 29
2.3.1 Simplified Numerical Modelling Techniques 30
2.3.2 Modelling Femoral Bone Geometry 31
2.3.2.1 Generic Femoral Models 31
2.3.2.2 Subject-Specific Numerical Femoral Models 33
2.3.3 Numerically Modelling Bone Structure and Geometry 34
2.3.3.1 Numerically Modelling Compact Bone 34
2.3.3.2 Numerically Modelling Cancellous Bone 35
2.3.4 Numerically Modelling Material Interfaces 36
2.3.5 Numerically Modelling Femoral Loading 38
2.3.5.1 Femoral Loading Cycle 39
2.3.5.2 Modelling Muscle Inclusion 39
2.3.5.3 Femoral Loading Resulting from Muscular Wrapping 43
2.3.5.4 Femoral Joint Boundary Conditions 43
2.3.5.5 Muscular Loading Magnitude for Femoral Models 44
2.3.5.6 Modelling Muscular Load Attachment to the Femur 45
2.3.5.7 Changes in Femoral Loading Post Implantation 46
2.3.6 Choosing and Calculating Resultant Quantities 47
2.3.6.1 Mechanical Failure 47
2.3.6.2 Stress Shielding of Femoral Regions 47
2.3.6.3 Quantifying THA Stem Loosening 49
2.3.7 Femoral Model Mesh Characteristics 49
2.3.8 Solution Accuracy 50
2.3.9 Numerical Optimisation Techniques for THA Stem Analysis 50
2.3.9.1 Composite Materials and Optimisation 52
2.3.9.2 Numerical Modelling as a Tool for Optimisation 53
2.3.9.3 2-Dimensional Optimisation within Numerical Modelling 54
2.3.9.4 3-Dimensional Optimisation within Numerical Modelling 56
2.3.10 Modelling Adaptive Bone remodelling 58
2.4 Literature Review Summary 58

Chapter 3

PRELIMINARY NUMERICAL MODELLING OF THE INTACT FEMORAL SYSTEM 60

3.1 Introduction 60
3.2 Research Aim 60
3.3 Preliminary Intact Femoral Model Construction 61
3.3.1 Model Geometry Generation 61
3.3.2 Model Meshing 62
3.3.3 Material Characteristics 64
3.3.4 Model Loading 65
3.3.5 Model Solution 66
3.4 Model Validation 66
3.5 Conclusion 69

Chapter 4

UNDERSTANDING RESULTANT SENSITIVITY TO CHANGES IN MODEL CHARACTERISTICS 71

4.1 Introduction 71
4.2 Research Aim 72
4.3 Model Generation 72
4.3.1 Model Aquasition 73
4.3.2 Quantifying Resultant Trends 74
4.4 Choice of Loadstep 76
4.5 Refinement of Muscular Inclusion 79
4.6 Anatomically Accurate Distribuion of Muscular Load 82
4.7 Knee Restraint Boundary Condition 83
4.8 Model Verification 87
4.9 Conclusion 89

Chapter 5

GENERATION OF AN IMPLANTED FEMORAL MODEL USING ADVANCED MODELLING TECHNIQUES 93

5.1 Research Aim 93

5.2 Introduction 93

5.3 Methodology 96

5.3.1 Cadaveric Specimen Selection 96

5.3.2 Implant Selection 97

5.3.3 Surgical Extraction of the Cadaveric Femora 98

5.3.4 Numerical Model Generation for the Intact Femora 99

5.3.4.1 CT Scanning 99

5.3.4.2 Finite Element Model Generation 100

5.3.4.3 Intact Femoral Model Boundary Conditions 104

5.3.5 Numerical Models of Implanted Femora 104

5.3.5.1 Creation of THA Stem Meshes 104

5.3.5.2 Surgical Implantation of Cadaveric Femora 106

5.3.5.3 CT Scanning of Implantation of Cadaveric femora 107

5.3.5.4 Implanted Model Generation 108

5.3.5.4.1 Stem 'B' Implanted Femoral Model 108

5.3.5.4.2 Stem 'A' Implanted Femoral Model 109

5.3.5.5 Implanted Femoral Model Boundary Conditions 111

5.4 Analysis 112

5.5 Model Results and Discussion 112

5.5.1 Intact Femoral Models 113

5.5.2 Implanted Femoral Models 115

5.6 Model Verification 118

5.7 Conclusion 119

Chapter 6

OPTIMISATION OF IMPLANT CHARACTERISTICS FOR EXTENDED SERVICE LIFE 120

6.1 Introduction 120

6.2 Research Aim 121

6.3 Investigation into Stress Shielding and Maximum Cement Stress Response to Variation of Homogeneous THA Stem Stiffness 121

6.3.1 Research Methodology 121

6.3.2 Results 122

6.3.3 Discussion 124

6.4 Investigation into the Optimisation of THA Stem Stiffness Distribution.... 125

6.4.1 Research Methodology 126

6.4.2 Results 129

6.4.3 Discussion 132

6.4.4 Conclusion 137

Chapter 7

SUMMARY AND CONCLUSIONS 138

Chapter 8

FUTURE WORK 141

Glossary 143

References 146

Appendix A 154

Appendix B 167

LIST OF FIGURES AND TABLES

Figure 1.1: The diagram above shows normal and damaged hip joints and positioning of components within a THA (Mayo Foundation for Education and Research, 2005). 1

Figure 1.2: Simple stress shielding model. 3

Figure 2.1: Cement is packed into the cavity created in the femoral neck and shaft and then pressurised prior to inserting the THA stem (Sledge, 1998). 11

Figure 2.2: The THA stem is coated with cement prior to insertion to prevent blood and other contaminants at the cement-THA stem interface (Sledge, 1998). 11

Figure 2.3: Cross section through the upper femur displaying THA stem outline and some cement (Schaldach et al., 1976). 12

Figure 2.4: Surgical implantation of a cementless THA stem with surface coating technology. Forceful impaction is necessary to achieve the interference fit (Sledge, 1998). 13

Figure 2.5: Stress-Strain curves for 'wet' compact bone (Ashby et al., 1997). 22

Figure 2.6: Stress-Strain curves for 'wet' cancellous bone (Ashby et al., 1997). 25

Table 2.1: Dependence of cancellous bone strength behavior on anatomic site (Morgan et al., 2001). 26

Figure 2.7: Cross sectional view through the upper femur showing cancellous bone structure (Wolff et al., 1986). 28

Figure 2.8: Schematic sketch of the cancellous bone structure within the upper femur (Wolff et al., 1986). 28

Figure 2.9: Disturbed static stressing of bones by fixing a length of wire between both ends, (Wolff et al., 1986). 29

Figure 2.10: Resultant bone geomtery following the application of 'du Hamel's loop', (Wolff et al., 1986).

..... 29

Figure 2.11: Importation of the 'Standardised Femur' into Solid Edge V9, (2000). 32

Figure 2.12: Methods of generically modelling the cellular cancellous bone structure, (Ashby et al., 1997). 37

Figure 2.13: Muscular attachment areas of the femur - posterior view, (Cunningham and Romanes, 1986). 42

Figure 2.14: Muscular attachment areas of the femur - anterior view, (Cunningham and Romanes, 1986). 42

Figure 2.15: Optimal THA stem geometry and resulting SED within the cement found by (Huiskes & Boeklagen, 1989). 55

Figure 2.16: Traditional THA stem geometry with no collar/bone contact and resulting SED within the cement found by (Huiskes & Boeklagen, 1989). 55

Figure 2.17: 2-dimensional numerical model employed by Kuiper & Huiskes (1997), showing load cases and non-homogeneous bone density distribution. 56

Figure 2.18: Results showing THA stem-bone interfacial failure index and optimal THA stem stiffness distribution for a resorbed bone mass fraction of 7.5% (Kuiper & Huiskes, 1997). 56

Figure 2.19: Model meshed used by Katoozian & Davy (2000): (a) 3-dimensional model with joint loading; (b) initial implant geometry; (c) anterior-posterior view of the optimal implant geometry; (d) isometric view of the optimal implant geometry. 57

Figure 3.1: Internal and external contours defining the geometrical 'wire frame', (Rhinoceros V1.1, 2000). 62

Figure 3.2: Smoothed and unsmoothed model surfaces, (Rhinoceros V1.1., 2000). 63

Figure 3.3: Smoothed mesh including second-order hexahedral 'brick' elements in the femoral neck and shaft, and second-order tetrahedral 'brick' elements in the femoral head, (ANSYS V5.7.1., 2002). 64

Figure 3.4: Comparison of model resultant principal strains along an anterior path with those obtained

from Duda et al. (1998). 67

Figure 3.5: Contour plot of Von Mise's equivalent strain profile for the model, (ANSYS V5.7.1., 2002). 68

Figure 4.1: Left femur model mesh obtained from the 'VAKHUM' project (Van Sint Jan, 2002). 73

Figure 4.2: Contour plot of Young's Modulus distribution within the model. 74

Figure 4.3: Paths (purple) along which results are recorded for graphical representation. 75

Table 4.1: Joint reaction and muscular loading data (Duda et al., 1998). 78

Table 4.2: Resultant avererage Von Mise's Equivalent Strain Energy Density along paths of interest for load regimes. 79

Figure 4.4: Von Mise's Equivalent Strain Energy Density along paths of interest for 45 % gait cycle load regime. Spike in Von Mise's Equivalent Strain Energy Density on the lateral path is attributed to muscular loading on that particular node. 80

Table 4.3: Muscular group inclusion within specific solutions. 81

Table 4.4: Solution change from complete muscular loading regime generated by reduced muscular inclusions. 81

Figure 4.5: Muscular loading applied as point loading and distributed loading. 83

Figure 4.6: Comparison between point and distributed muscular loading for medial and lateral paths. Distributed loading eliminates the 'spike' in results generated with point loading on the lateral path. ... 84

Figure 4.7: Comparison between point and distributed muscular loading for anterior and posterior paths. 85

Figure 4.8: Reduced length femoral model. Purple indicated regions of interest and red indicates restraint location. 85

Table 4.5: Restraint condition details and results. 86

Table 4.6: Comparison between average Von Mise's Equivalent Strain Energy Density along paths for given

element types. 88

Figure 4.9: Comparison between average Von Mise's Equivalent Strain Energy Density along the posterior path for given element types. 89

Figure 4.10: Von Mise's equivalent strain solution contour plot for the final model. 90

Figure 4.11: Von Mise's Equivalent Strain Energy Density for the final model. 91

Figure 5.1: The CPT THA stem, subsequently referred to as stem 'A', has a double-tapered geometry with a highly polished surface finish. The pictured CPT stem is a retrieved specimen with scratches and is no longer highly polished 94

Figure 5.2: The Spectron THA stem, subsequently referred to as stem 'B', has a collared stem geometry with grooves and a grit blasted surface finish. 95

Figure 5.3: X-ray image showing the pelvic region of the cadaveric specimen chosen for this research. 98

Figure 5.4: Explanted embalmed cadaveric femora with excess soft tissue removed. 99

Figure 5.5: CT scan through the femoral heads of the cadaveric femora. 100

Figure 5.6: Young's Modulus contour plot for the right-hand intact femoral model showing cross sectional variation. 102

Figure 5.7: Left-hand and right-hand intact femoral model meshes. The use of cubic elements gives a jagged surface. 103

Figure 5.8: Model mesh for stem 'A', neglecting some geometric detail in regions exterior to the cement. 105

Figure 5.9: Model mesh for stem 'B', neglecting some geometric detail in regions exterior to the cement. Although included, the image does not clearly show grooves in the stem. 105

Figure 5.10: Right-hand cadaveric femur with surgically implanted stem 'A'. 106

Figure 5.11: Left-hand cadaveric femur with surgically implanted stem 'B'. 107

Figure 5.12: This CT scan of the implanted femora includes 'diffraction artefacts' that darken regions within the image giving a false indication of bone density. 107

Figure 5.13: Cross-section through the left-hand implanted femur mesh indicating bone, cement and THA stem locations within the mesh. 109

Figure 5.14: Young's Modulus contour plot showing material stiffness differential at the bone-cement interface. 109

Figure 5.15: Model mesh for the left-hand femur implanted with stem 'B'. 110

Figure 5.16: Model mesh for the right-hand femur implanted with stem 'A'. 111

Figure 5.17: Resulting Von Mise's Equivalent Strain Energy Density, plotted along all paths for the intact left-hand femoral model. Silhouette in the plots background indicates path region along femur. 113

Figure 5.18: Resulting Von Mise's Equivalent Strain Energy Density, plotted along all paths for the intact right-hand femoral model. 114

Figure 5.19: Comparison of percentage change in Von Mise's Equivalent Strain Energy Density distribution along the Medial path following implantation. 116

Figure 5.20: Comparison of percentage change inVon Mise's Equivalent Strain Energy Density Distribution along all paths caused by the bonded THA stems. 118

Figure 6.1: Variations in Von Mise's Equivalent Strain Energy Density and maximum cement stress for variations in homogeneous THA stem stiffness. The results are normalised with the CoCr results. 123

Figure 6.2: Change in Von Mise's Equivalent Strain Energy Density distribution from the intact condition along all paths for both the CoCr and titanium THA stems. 124

Figure 6.3: Sections within the THA stem that have different stiffness. 127

Figure 6.4: Information flow process during the ANSYS design optimisation procedure. 129

Table 6.1: Changes in SSI's with constant CSI's using homogeneous and optimised THA stem stiffness distributions. 130

Table 6.2: Distribution of Young's Modulus along THA stem length. 130

Figure 6.5: Change in Von Mise's Equivalent Strain Energy Density distribution within the upper femoral shaft from the intact condition along all paths for both a homogeneous CoCr THA stem and an optimal non-homogeneous THA stem producing a identical maximum stresses within the cement. 131

Figure 6.6: Change in Von Mise's Equivalent Strain Energy Density distribution within the upper femoral shaft from the intact condition along all paths for both a homogeneous titanium THA stem and an optimal non-homogeneous THA stem producing a identical maximum stresses within the cement. 132

Table A.1: Mechanical properties of 'wet' compact human and bovine bone (Ashby et al., 1997). 154

Table A.2: Muscular loading magnitudes and directions developed by Cheal et al. (1992), and modified by Duda et al. (1998) to give a more accurate four-phase gait cycle. 155

Figure A.1: Comparison of model resultant principal strains along a medial path with those obtained from Duda et al. (1998). 156

Figure A.2: Comparison of model resultant principal strains along a lateral path with those obtained from Duda et al. (1998). 157

Figure A.3: Von Mise's Equivalent Strain Energy Density along paths of interest for 10 % gait cycle load regime. 158

Figure A.4: Von Mise's Equivalent Strain Energy Density along paths of interest for 30 % gait cycle load regime. 159

Figure A.5: Von Mise's Equivalent Strain Energy Density along paths of interest for 70 % gait cycle load regime. 160

Figure A.6: Preparation of the femoral canal allowing implantation of stem 'A' (the CPT THA stem). 161

Figure A.7: Cement filling the cavity within the femoral canal. 161

Figure A.8: Implantation of stem 'B' (the Spectron THA stem). 162

Figure A.9: Implanted cadaveric femora. 163

Figure A.10: Comparison of percentage change in Von Mises Equivalent Strain Energy Density

distribution along the Anterior path. **164**

Figure A.11: Comparison of percentage change in Von Mises Equivalent Strain Energy Density distribution along the Posterior path. **165**

Figure A.12: Comparison of percentage change in Von Mises Equivalent Strain Energy Density distribution along the Lateral path. **166**

STATEMENT OF ORIGINALITY

This work contains no material which has been accepted for the award of any other degree or diploma in any university or other tertiary institution and, to the best of my knowledge and belief, contains no material previously published or written by another person, except where due reference has been made in the text.

I give consent to this copy of my thesis, when deposited in the University Library, being available for loan and photocopying.

David S. Thompson, 1st March 2006.

ACKNOWLEDGEMENTS

This research has been undertaken with the support of the University of Adelaide School of Mechanical Engineering and the CSIRO Division of Manufacturing & Infrastructure Technology (CMIT).

Firstly, I would like to acknowledge and thank my parents John and Judy Thompson for their constant support and commitment to my education.

The supervision of Dr Michael Painter and Dr Ben Cazzolato is gratefully acknowledged. These supervisors generously assisted me with direction and advice throughout the duration of this research, in particular with the preparation of this document. Dr Mike Painter must be thanked in addition for his excellent problem solving discussions that were frequently undertaken.

I would like to thank Alek Bachorski and Alex Dunstone with whom I shared an office during the course of my research for their contributions in productive research discussions and maintaining an enjoyable environment.

Further, I would like to thank Professor Trevor Hearn of Flinders University and Dr John Costi of the University of Vermont for examining this doctoral thesis. Their insightful comments were very useful in improving the quality of this thesis.

Lastly, I would like to express my appreciation to Joanne for her love, support and encouragement during the preparation of this thesis.

Chapter 1

INTRODUCTION

1.1 Total Hip Arthroplasty (THA)

A total hip replacement is performed to alleviate pain and debilitation caused by arthritis, fractures, dislocations, congenital deformities, and other hip related problems.

Total Hip Arthroplasty (THA), involves replacing damaged surfaces on the hip joint surface with smooth artificial surfaces. The surgeon removes the head and the neck of the femur and replaces them with a substitute ball and stem. A 'cup' or 'socket' is placed into the damaged socket. The ball and stem fit into this cup, creating a new movable joint. These can be seen in Figure 1.1.

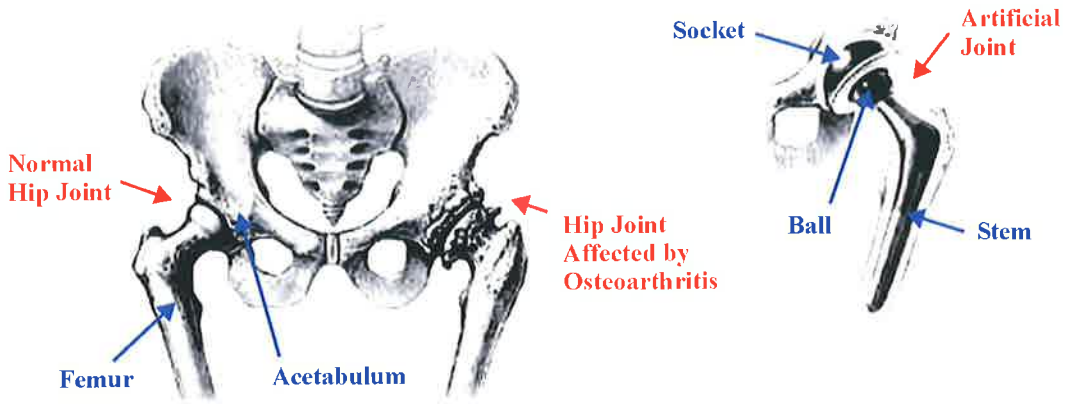


Figure 1.1: The diagram above shows normal and damaged hip joints and positioning of components within a THA (Mayo Foundation for Education and Research, 2005).

The operation usually takes around two hours. The hospitalisation time is relatively short, often about five or six days. Full recovery takes about 4 to 6 months in most cases. THA is one of the most successful procedures in orthopaedic surgery with respect to restoration of limb function and relief of pain (Cheal et al., 1992; Baleani et al., 2000).

Medical implantation is a well-established and advanced research field. Vast quantities of literature exist, but this encompasses conflicting views and approaches, and indicates there is scope for improvement in both surgical technique and implant design.

1.1.1 Problems Associated with THA

Countless THA techniques and components exist today, with the majority of component manufacturers claiming their products are superior. Numerous complications exist with this surgery, many of which can be partly attributed to implant material incompatibility with the natural hip system and implant system design. Of the 800,000 hip replacements performed each year worldwide, 1-10% will fail depending on the implant design (Simoes et al., 2000).

Apart from infection, aseptic loosening (loosening occuring in the absence of clinical or microbiological evidence of infection) is the major post surgery concern associated with THA. Aseptic loosening is caused by both mechanical and biological factors. Mechanical failure of the implant or cement, introduction of wear debris to material interfaces, interfacial motion and stress shielding are all phenomena that lead to a biological response in the bone causing resorption and the eventual loosening of the implant (Joshi et al., 2000).

Stress shielding within the femur occurs when regions of bone experience a reduction in stress level following implantation. Much of the load bypasses upper femoral regions and is carried through the stiff metallic THA stem to lower regions within the femur. Severity of stress shielding is a product of load orientation and magnitude, interface characteristics, implant geometry, cement mantle geometry, and material characteristics. The problem is mainly caused

by the inherent mismatch of implant and bone stiffness (Bedzinski et al., 1998). The concept of stress shielding is illustrated in Figure 1.2.

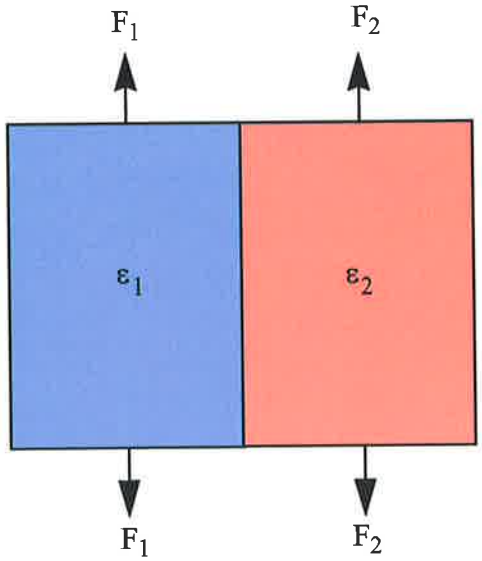


Figure 1.2: Simple stress shielding model.

The stress shieldng model in Figure 1.2 is governed by the following relationships;

$$\varepsilon = \varepsilon_1 = \varepsilon_2 \tag{1.1}$$

$$F_1 = \sigma_1 A_1 = \varepsilon_1 E_1 A_1 = \varepsilon E_1 A \tag{1.2}$$

$$F_2 = \sigma_2 A_2 = \varepsilon_2 E_2 A_2 = \varepsilon E_2 A \tag{1.3}$$

$$\frac{F_1}{F_2} \propto \frac{E_1}{E_2} \tag{1.4}$$

Within this analysis, ε represents strain (mm/mm), F represents force (N), σ represents stress (N/mm^2), E represents Young's modulus (N/mm^2) and A represents area (mm^2). Equation 1.1 describes the identical strain within the two equally sized bonded materials for a given force. Due to dissimilar strengths, the materials have different stresses for the given strain. This causes the proportion of load shared by the two bonded materials to be a function of the difference in material stiffness, as described in Equation 1.4, and so the stiffer material experiences more load and the less rigid material experiences less load.

This stress shielding causes bone resorption due to the process of adaptive bone remodeling, defined within Wolff's Law (Wolff, 1986). This resorption can also result from mechanical failure of the supporting tissue at the implant-bone or cement-bone interface (Cheal et al., 1992). Resorption of bone from around the prosthesis inevitably causes loosening, leading to THA failure. Failure of THA components causes significant pain and discomfort, to the patient, requiring difficult and occasionally unsuccessful revision surgery.

1.2 THA Medical Procedure

The pioneering surgeon Sir John Charnley led the era of modern THA in the late 1950s. Charnley's original concept of a 'low-friction arthroplasty' has survived in virtually all its original form. Countless attempts have been made to improve upon that design, however many have not been successful.

Current THA may be cemented in which the metal implant is attached to the bone using 'glue', uncemented, or a hybrid combination. The most widespread type is an uncemented socket and a cemented femoral stem. Bearing surfaces used include ultra high-density polyethylene, stainless steel, chrome-cobalt, and more recently, ceramics.

Surgical techniques are honed with years of effort. The orthopaedic surgeon is required to approach surgery in a systematic and flexible fashion, and be prepared for unexpected

occurrences. Also, because total hip surgery is increasingly being performed on younger patients, the surgeon needs to allow for future revisions when executing the primary procedure. Orthopedic surgeons should not attempt to limit the opportunity for future surgery through the removal of excess bone. Surgeons require understanding of the implant system being used, often choosing it on the basis of personal experience and prior clinical performance.

During the initial consultation, the surgeon evaluates the soft tissues around the hip, searching for abnormalities. X-rays are taken at specific angles, and used to 'template' standard implant sizes. Conducting this preoperatively ensures correct fitment of the implant and also alerts the surgeon to anatomical variations. Variation in bone size and shape is common, so there is a requirement for ranging implant sizes.

In most circumstances, the acetabulum (opening on each side of a pelvis that allows for the insertion of a ball-like proximal end of each femur) will use an uncemented implant with a surface of either beads, fibre mesh, or a rough plasma-sprayed surface. Stems (femoral implant component) may be anatomic or non-anatomic in design, may have a polished or rough surface finish, and like the socket, may have a coating of hydroxyapatite. Hydroxyapatite is a complex crystal of calcium phosphate, and is a significant mineral component of bone and teeth. It is used to provide superior bonding between implant and bone on uncemented implants. Prosthetic options and choices should be evaluated, taking into consideration the age and activity level of the patient as well as host bone quality.

The operation commences with a large incision made in the hip to adequately expose and retract tissues. After dislocation, the acetabulum is reamed to accept the socket. If an uncemented socket is to be used, a larger recess is machined. The acetabulum socket is then installed.

The femoral head is removed, and the intramedullary canal located. Femoral bone quality is assessed and a decision finalised about cementation of the femoral component. If adequate stability of the implant cannot be achieved in a cementless approach or if the bone stock is

inadequate, then cemented implantation is preferred. Many surgeons prefer cemented THA stems regardless.

Installation of the femoral implant requires attention to alignment. Some implants have adjustable alignment control as a feature of the femoral component. The hip is relocated and the range of motion, stability, offset, and leg lengths assessed. When an uncemented implant is used, wire is often wound around the femoral shaft in order to prevent inadvertent fracture upon insertion, as the impact of driving the femoral component often splits bone. If a cemented implant is being used, the intramedullary canal (hollow in the femoral shaft) is prepared in a fashion similar to the acetabulum. A cement restrictor and stem centraliser are inserted within the intramedullary canal. Finally, the cement (often mixed with a special mixing system such as a vacuum or centrifugal) is inserted with a gun and pressurized seal.

It is critical to check the hip for positions of instability. In most cases, dislocation would be due to inadequate restoration of leg length, which can be corrected by removing the modular head and inserting a longer neck (if possible), assuming the implant is correctly positioned.

The severed muscles are then reattached, with bone anchors used to accomplish adequate fixation. Mobility is limited immediately after surgery, however partial weight bearing is often accomplished within days after surgery.

1.3 Significance and Motivation

Reliable restoration of human limb function for those who have damaged joints is important. This restoration of limb function provides an improvement to quality of life through elimination of pain, suffering and immobility. Restoration of limb function is valuable; however serious issues arise if the implant system fails before the life expectancy of the patient. Current implant systems generate stress shielding of bone within the upper femur, limiting the service life of the

implant greatly. Creation of an implant system that does not stress shield bone is essential if extended implant system service life is desired.

Increasing human life expectancy and decreasing age of THA recipients necessitate an extension of THA service life. An increase in THA service life will reduce the requirement for costly and difficult revision surgery and eliminate additional trauma experienced during that revision surgery. Improved implant system design will provide extended service life and save significant cost considering the vast number of implants produced on a yearly basis. Improvements in manufacturing technology allow for advancement in the design of implant systems endeavouring to achieve extended service life. Advanced numerical simulation provides a valuable tool for improvement in implant design.

The THA modelling system developed in this research is state-of-the-art, having superior refinement to existing models. Previous numerical methods neglect many environmental conditions to the extent that results cannot confidently be correlated to the real life system. This modelling technique will generate solutions that can be related to the real life system effectively. Biomedical implant design does not lend itself to trial and error design methodology, increasing the desire to implement simulation techniques. Development of this numerical simulation technique allows for evaluation of both existing implant system technology and development of new technology that minimises stress shielding.

Current implant system design is usually a process of simple geometry evolution. The numerical simulation technique developed here will allow for optimisation of both implant geometry and material properties, generating an implant system that is more compatible with the human body. Modern manufacturing technology has the ability to produce implants with optimised stiffness distribution, effectively enabling control of stress shielding. Designing for this manufacturing technology through the use of modulus optimisation will produce implants that do not significantly stress shield volumes of bone, and so considerably extend implant service life.

The following chapters describe the processes used to develop the numerical optimisation technique that generates the required optimal THA stem stiffness distributions. Initially, simplistic modelling is conducted to allow familiarisation with the natural and implanted femoral environment. A model sensitivity analysis is then conducted to find suitable model characteristics that enable efficient and accurate modelling. Once these are understood, an accurate, implanted femoral model is constructed and used to design a novel implant with optimum graded elastic modulus for reduced stress shielding by comparison to other models. Whilst it is not possible to accurately correlate the amount of bone adaptation caused by a quantity of stress shielding, it is known that reducing stress shielding does in turn lessen bone adaptation, which is vital for enhanced THA survival.

Chapter 2

LITERATURE REVIEW

2.1 THA Femoral Implant Characteristics

The femoral THA prosthesis is an extremely important device, engineered to function as a compromise between performance and expense. The environment surrounding the implant is both biologically and mechanically complicated. The consequences of poor implant system performance are painful, expensive and disabling. Designing implant systems for this biological environment is difficult.

The necessary strength of the implant, as in other mechanical systems, is usually determined from the expected loading conditions. However uncertainty about the importance of occasionally applied loads that are higher in value relative to those loads applied on a frequent basis is the major difficulty associated with the design of prosthetic devices (Paul, 1999). If the applied loading conditions are too conservative during design, the implant will become oversized and exaggerate stress shielding issues.

A prosthetic implant should adequately transfer stress at the bone-implant interface to guarantee long-term mechanical stability. Nonphysiological stress transfer may cause pressure necrosis and/or resorption at the bone-implant interface or implant delamination (Callaghan, 1995).

Complete stem-bone bonding will lead to a noticeable increase in stress shielding (McNamara et al., 1997), however failure to achieve adequate implant fixation will lead to excessive micromotion, pain and eventual failure.

Two methods of THA stem fixation further complicate loading transfer. Cementless or 'press-fitted' implants stress the surrounding bone to achieve fixation, and have a different load transfer pattern than cemented implants. Extensive research has been conducted to resolve which fixation method is superior, however, at present no clear answer has been found. A more appropriate solution may be to select a fixation technique that best suits individual circumstances such as bone quality and age of the recipient.

2.1.1 Cemented THA Stem Implantation

Cemented femoral implantation has traditionally been the most common form of fixation. The implantation technique is generally not as complex and critical as with cementless implantation techniques, and it therefore has some advantages. The cement acts as a load transferring cushion, distributing load from the shaft to the bone over an increased area (Callaghan, 1995). Figure 2.1 and Figure 2.2 show the application of cement to the femur and THA stem during surgery respectively. The typical cement volume and THA stem location can be seen in Figure 2.3.

Although there have been many cemented THA stem designs available over the last 30 years, few have had superior clinical results than the smooth faced stainless steel Charnley and Exeter designs (Callaghan, 1995). More recent cemented implantation techniques have improved implant to bone bond quality, however this implantation technique is not recommended for everyone. Attributes associated with a reduced implant system service life for cemented implants include individuals with ages below 55, weight above 80kg, active lifestyle and male gender (Callaghan, 1995).

Cemented implantation techniques also have undesirable characteristics. The high temperature of polymerization of the cement when curing has been linked with bone damage (Markov et al., 1998). Furthermore, cement fatigue and material separation detract from this design.

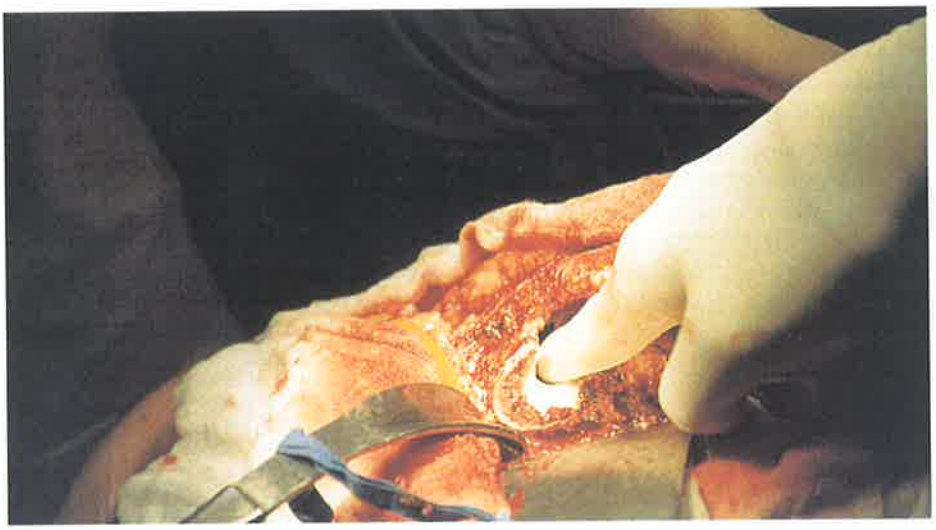


Figure 2.1: Cement is packed into the cavity created in the femoral neck and shaft and then pressurised prior to inserting the THA stem (Sledge, 1998).



Figure 2.2: The THA stem is coated with cement prior to insertion to prevent blood and other contaminants at the cement-THA stem interface (Sledge, 1998).

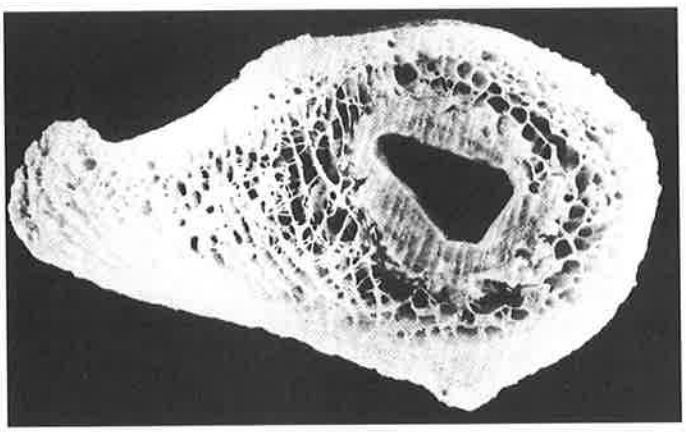


Figure 2.3: Cross section through the upper femur displaying THA stem outline and some cement (Schaldach et al., 1976).

Katoozian et al. (2000), reported that within a cemented femoral implant environment, a succession of creep and relaxation takes place within the polymer. Katoozian et al. (2000), indicated that 100 days after implantation, 70% of the residual stresses that maintain bonding at the interface are relieved, and total stress relief will occur after 1 year, giving an interface that is no longer rigidly bonded.

Cemented implants have value for specific individuals, however cemented implant system design advancement is more limited than the cementless variety. Increasing implant technology may eliminate the use of cement to achieve implant fixation, however issues such as poor bone quality in some individuals require the use of cemented implant systems. Cementless femoral implants stress the bone to achieve fixation, and risk of bone fracture escalates in individuals with poor bone quality. Hence there will continue to be a market for cemented implants.

2.1.2 Cementless THA Stem Implantation

Cementless femoral implants have become increasingly popular in recent times. Cementless implantation was primarily developed in an attempt to overcome problems associated with cement (Joshi et al., 2000), particularly in young active patients where cemented implantation

seems to fail more regularly (Callaghan, 1995). Cementless femoral implants offer simpler revision surgery than cemented implantation further adding to their appeal.

Unlike in cemented implantation, the quality of initial fitment is crucial with cementless implants as intimate contact is required along the interface (Joshi et al., 2000). Porous implant coatings are often employed to encourage bone growth into the implant, often with the addition of bioactive coatings and treatments. Figure 2.4 shows implantation of a cementless THA stem with surface coating technology.

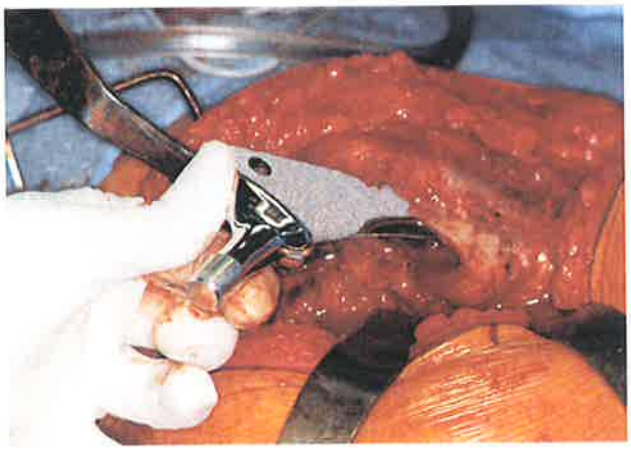


Figure 2.4: Surgical implantation of a cementless THA stem with surface coating technology. Forceful impaction is necessary to achieve the interference fit (Sledge, 1998).

2.1.3 THA Stem Surface Finish and Implications in Cemented THA

Cemented THA stems must maintain stability in order to achieve long term success (Speirs et al., 2000, Verdonschot et al., 1998, Harris 1992, Verdonschot & Huiskes 1997). Failure to maintain stability is the major cause of cemented THA stem failure (Hinrichs et al., 2003, Nuño & Avanzolini, 2002). Most cemented THA stems available within the global market use one of two major stabilisation mechanisms to achieve fixation. Stems with a matt or rough surface finish are designed to mechanically bond with cement, while stems with a polished or smooth

surface finish that generally taper towards the distal end intend to slide and migrate within the cement and achieve fixation through a wedging motion.

During the 1970's, cemented THA stems became commonly available with an increased surface roughness (Collis & Mohler, 1998). This subtle transformation towards a coarser stem surface finish occurred without initial clinical or laboratory studies assisting the direction of prosthesis engineering (Collis & Mohler, 1998), raising uncertainty about its merit.

Eliminating separation or debonding of the THA stem from the cement is important (Harris, 1992), and is a requirement for extended survival of cemented THA (Verdonschot & Huiskes, 1997). As stem-cement separation occurs, stresses within the cement mantle are elevated (Verdonschot & Huiskes, 1997), and wear particles are produced. Once debonded, stems with rougher surface finishes produce more wear particles than polished stems (Verdonschot et al., 1998), accelerating the failure process (Verdonschot & Huiskes, 1997). Retrieval studies support this hypothesis, suggesting that cemented THA stem loosening is initiated at the cement-stem interface (Verdonschot et al., 1998).

Cemented polished, collarless, double tapered THA stems do not compromise cement as they generate 'taper lock', that is they slip distally achieving stability within the cement (Speirs et al., 2000), and generate compressive stresses within the cement-stem interface (Norman et al., 2001). Preservation of the cement is of great importance, and could be the basis for the Swedish Hip Register finding polished stems clinical superior to matt stems (Verdonschot et al., 1998).

It has been suggested that in a long term situation, the strong cement-implant bond associated with rough THA stem surfaces may have undesirable effects on the bone-cement bond (Ling, 1992), resulting from a dissimilar loading mode within the cement compared to polished THA stem systems. Polished THA stems transfer load to cement primarily through compression, which can be transferred without a reliable bond (Ling, 1992). Rough surface THA stems permit

tensile load transmission to the cement and risk cement fracture (Ling, 1992). This leads to the belief that designing THA stems that require tensile cement bonding is unwise (Ling, 1992).

Conversely, studies involving cemented THA stems conducted by Harris et al. (1992) found it unnecessary for the cement-metal interface to slip to protect the cement-bone interface, with bonding of both surfaces achievable even after more than 17 years. This approach requires the cement to function as an adhesive, and not as a grout, as originally intended by Charnley (Collis & Mohler, 1998).

The personal experience of Collis et al. (1998) indicates that cemented THA stems with roughened surfaces loosened faster than those with polished surfaces. Since April 1993, Collis has personally implanted 454 cemented polished THA stems only, with no radiographic findings of loosening or need for revision to October 1998. Collis et al. (1998) also analysed three prior studies that investigated the influence of surface finish on cemented THA stems, all with sample size greater than 100. Only two of these studies examined implants that had similar geometry with both rough and polished THA stem surfaces. Of these two studies, it was found that the incidence of revision for both surfaces was similar, however osteolysis was more prevalent and the need for revision more urgent with the loosening associated with rough surface finish implants.

Hinrichs et al. (2003) conducted a retrospective study into the survival rate of the same cemented titanium alloy THA stem with different surface finishes. Within this investigation there were 220 smooth surface finish stems (mean follow-up 11 years, 4 months) and 343 rough stems (mean follow-up 5 years and 10 months). Results from this study find 18 cases of revision in the polished surface finish stem group, and 30 cases in the rough surface finish stem group. This leads to the conclusion that with a significantly shorter follow-up time, there is clearly a higher incidence of the need for revision with the rough surface finish cemented THA stems.

Howie et al. (1998) investigated the loosening of 20 matt and 20 polished cemented THA stems with identical tapered non-modular stem designs of the Exeter type. After 9 years, four matt stems and no polished stems were revised due to loosening. Howie et al. (1998) concluded that different surface finish stems behave differently in cement, and that the surface finish determines the way that loads are transmitted into the cement and into the bone. It was also noticed that polished stems subsided early within the cement mantle, but did not loosen in agreement with the findings of Speirs et al. (2000) and Norman et al. (2001).

Barker et al. (1999) investigated the differences in load transfer associated with rough and polished collarless, double tapered stems in cemented hemiarthroplasty using both experimental and numerical sheep models. This study concluded that implants with both surface finishes generated significant postoperative proximal stress shielding that was not reduced after nine months of remodelling. It was also found that differences in stem surface finish caused no detectable strain variation within the proximal femur after nine months within the animal model. This was possibly caused by a strong cement fixation of stems with both surface finishes (Baker et al., 1999). This may also explain discrepancies in the role that cemented stem surface finish plays in load transmission found between this research and the findings of others such as Howie et al. (1998), Norman et al. (2001), Ling (1992) and Verdonschot et al. (1998).

Perhaps the most significant indicator for determining superior THA stem surface finish is the well documented success in a clinical environment of the original polished smooth stemmed Charnley prosthesis (Collis & Mohler, 1998). This implant has displayed good performance over one of the longest follow-up periods. Its stainless steel cemented THA stem has polished surface and tapered geometry. Revision rates for this implant are lower than most other implants with shorter follow-up periods (Collis & Mohler, 1998). Advances in cementing techniques (both materials and delivery systems) had not yet occurred and were not available for many subjects implanted with the original Charnley prosthesis, further emphasising the implants success.

In cemented implants, reducing the THA elastic modulus may amplify the rate of loosening when combined with a rough surface finish. Increased flexibility of titanium alloy THA stems with rough surface finish can overload cement which can debond under load, whereas the polished stems simply subside while maintaining stability (Hinrichs et al., 2003). Hinrichs et al. (2003) believes that cemented titanium alloy THA stems with a rough surface finish should not be recommended due to their high rate of loosening, whereas a polished surface is important in achieving long term THA durability.

Contact without motion must be maintained between cement and THA stem surface if the production of wear particles is to be avoided and long-term clinical success of THA achieved. This has been achieved with both cemented polished and rough surface finish THA stems, although polished stems appear to have a higher clinical success rate. Study into the level of stress shielding generated by cemented THA stems from both fixation design philosophies will provide more information surrounding the likelihood of clinical success.

2.1.4 Material Biocompatibility

The human body is an extremely harsh environment for foreign materials, as body fluids can significantly change the biological and mechanical properties of implanted material (Callaghan, 1995). Implant materials require sufficient strength, biocompatibility and biostability if long term success is to be achieved.

Chronic inflammatory reactions can occur when foreign material is introduced into the body. The degree of biological response is principally dependent on the nature of the implanted material (Callaghan, 1995). Conventionally we define three types of biomaterials: biotolerant, bioinert, and bioactive.

Stainless steel is a biotolerant material, and usually a thin fibrous tissue layer is produced at the bone-implant interface. Irritation of the surrounding tissue due to chemical products produced

by leeching from the implant causes this fibrous tissue layer to develop. These biotolerant materials are relativley cheap.

Cobalt alloys, titanium, and aluminum oxide are bioinert, and allow direct bone contact. This is referred to as osseointergration at the implant-bone interface under favorable mechanical conditions (Callaghan, 1995). Osseointergration is achievable due to the nonreactive environment surrounding the implant. These materials are moderately expensive.

Bioactive materials such as calcium phosphate ceramics facilitate direct chemical bonding at the implant bone interface. It is believed that the presence of free calcium and phosphate compounds at the implant surface is responsible for the chemical bond (Callaghan, 1995). The application of bioactive materials to the THA stem surface further increases expense.

Unfortunately cost is a major influence when choosing a THA stem. Bioinert implants with bioactive coatings is superior, however their high cost detracts from their appeal for the majority of patients.

2.1.5 Advances in THA Stem Design

Currently, THA stem design is advancing rapidly. Improved design and manufacture has reduced the risk of implant fracture (Baleani et al., 1999). Innovative materials and manufacturing techniques are constantly improving implant engineering. Composite materials seem to offer improved mechanical characteristics, and their acceptance within the marketplace seems only a matter of time. The orthopaedic industry has closely followed the aerospace industry in utilizing high performance metal alloys for implants, so it seems a natural progression that composite materials will be used (Simões et al., 2000).

The engineering of modern implants is increasingly aiming to reduce stress shielding. It is generally accepted that more flexible implants are required to reduce stress shielding and to minimise the excessive bone remodelling process around the implant (Bedzinski et al., 1998).

Studies have shown that flexible stems transfer load to the upper regions of the femur, thereby reducing stress shielding (Simões et al., 2000), and load the proximal end of the femur in a manner similar to the natural state (Joshi et al., 2000). Implant flexibility could be accomplished through the manipulation of material properties or through changes to implant geometry.

Gross et al. (2001) has demonstrated a reduction in stress shielding through the use of a hollow implant. By varying hollow implant internal geometry, isotropic materials such as stainless steel or titanium can be used to manufacture implants that vary in stiffness along their length. This is a relatively low cost alternative to changing the material modulus along the implant length.

Manufacturing an implant by combining materials of different stiffness can also meet the requirements of stress shielding through controlling the implant stiffness (Simões et al., 2000). Cheal et al. (1992) found that "Carbon fiber-reinforced polymer (CFRP) and carbon (CFRC) composites appear to be especially promising due to their high degree of tissue biocompatibility and the mechanical properties of these materials." Functionally graded materials also look promising for controlling stiffness.

Although flexible implants are desired, there are associated problems. More flexible prosthesis generate increased bone-prosthesis interfacial movement, which leads to high levels of failure due to the unstable fibrous tissue that forms at the interface (Simões et al., 2000).

Numerous implant designs have attempted to achieve a natural bone loading state through inclusion of external geometrical features. Munting et al. (1995) designed a femoral implant that is fixed to the lateral side of the proximal femur by means of a bolt and employs fins along the medial border to provide resistance to torsional moments. Experimental results for this implant show minimal micromotion, and short-term clinical studies show low initial failure rates (Joshi et al., 2000). Joshi et al., (2000) proceeded to improve upon the original design by employing cables rather than a stiff bolt through the brittle bone.

In summary, it is recognised that modification to the implants elastic stiffness can be used to control stress shielding. Variation of the structural stiffness could be achieved through manipulation and grading of material or through manipulation of geometry. At this point there is no known exact pattern of the relationship between THA stiffness and stress shielding.

2.2 Characteristics of Bone Material

Bone is a highly developed material, generated as a function of its mechanical requirements. Bone exhibits varying mechanical properties throughout the body, although its composition is the same. These varying mechanical properties are achieved through structural variation.

The mechanical properties of bone are related to the bone's anatomical function, and specific to the individual, age, history of disease and magnitude of physical activity. Bone is constructed as an elaborate laminate of hard, dense 'compact' or 'cortical' bone, covering a cellular porous 'cancellous' or 'spongy' bone. This structural design allows for economical load bearing, with peak stresses minimised through the dispersion of loading over large joint surface areas.

Bone is a composite of fibrous organic matrix, containing proteins (mostly collagen), filled with inorganic calcium compounds and amorphous calcium phosphate. It is the calcium compounds that are responsible for stiffness. The quantities of these constituents within compact and cancellous bone are almost identical, with only density differentiating the two bone types.

Bone sections that have a density less than $0.7 g/cm^3$ are classified as cancellous (Ashby et al., 1988). The amount of cancellous bone reduces in patients with bone conditions such as osteoporosis. The mechanical properties of cancellous bone beneath load bearing surfaces influences the distribution of the loading forces, and hence cancellous bone degeneration leads to changes in the loading distribution.

2.2.1 Compact Bone Material Characteristics

Figure 2.5 shows the stress-strain behavior of 'wet' compact bone. Bone is classified as 'wet' if it is fresh, and has not lost any moisture content. As the material loses moisture, its mechanical properties are altered until the point where completely 'dry' bone does not yield at all. When loaded in the longitudinal direction compact bone is linear-elastic to a strain of 0.7%, and yields plastically to strains of 3%, in both tension and compression, however in the transverse direction, wet compact bone is less strong, less stiff and less ductile, and fails in tension at strains of 0.6% (Ashby et al., 1988).

Mechanical properties of 'wet' compact human bone can be seen in Table A.1 in Appendix A (Ashby et al., 1997) along with bovine bone which although not used within this research was included for comparison. Van Rietbergen et al. (1999) concluded that cortical bone has a safety factor of approximately 2 for forces associated with daily activity. Apart from excessive values found in a few locations, the maximum stress found in his experiments (60.2 MPa) was less than half of the reported tissue fatigue strength (100-140 MPa) from Choi and Goldstien, (1992).

Human bones behave in a viscoelastic manner. Impact loading such as a heel strike causes the bone to resist the initial impact with a higher stiffness than if the loading were sustained. A slower rate of loading causes relaxation of the water molecules and collagen, producing a lower stiffness.

The ultimate compressive strength, σ_b, can be found using a model derived by Carter & Hayes (1976), given by Equation 2.1:

$$\sigma_b = 68\varepsilon^{0.06}(\rho^2) \qquad \textbf{(2.1)}$$

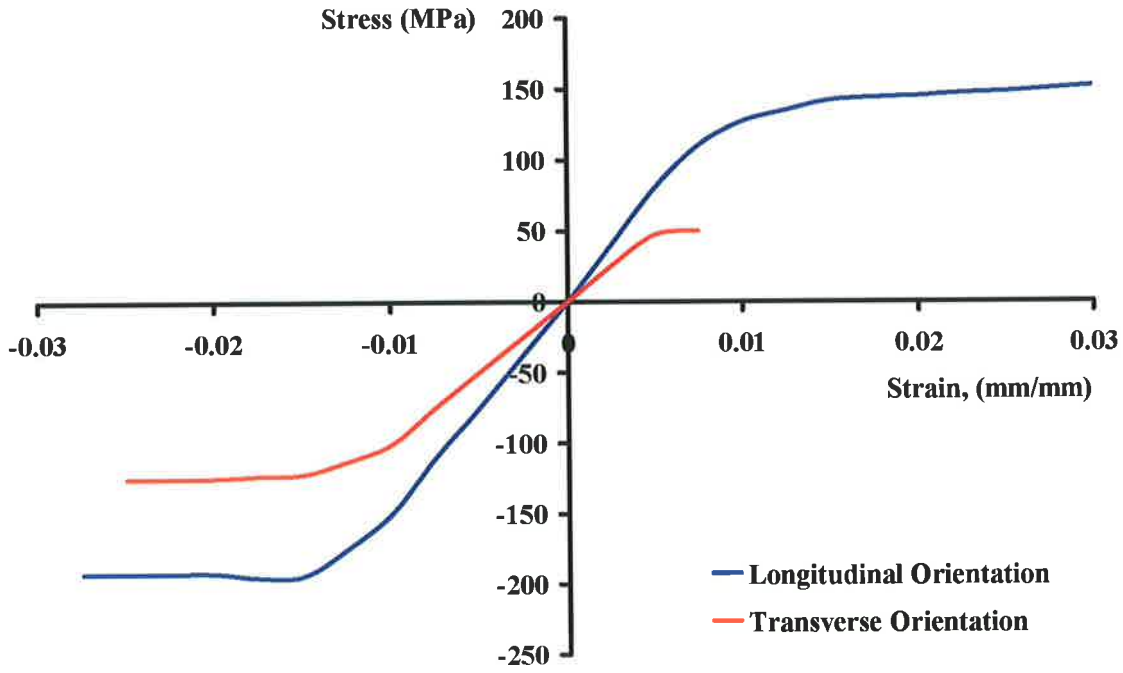


Figure 2.5: **Stress-Strain curves for 'wet' compact bone (Ashby et al., 1997).**

Equation 2.1 is a function of strain rate $\varepsilon(1/s)$ and apparent density $\rho(g/cm^3)$, and is valid for cortical and cancellous bone. A distinction between axial and transverse directions is not available in literature to date (Wirtz et al., 2000).

The stress relaxation of cortical bone (change in stiffness under constant displacement), $E(t)$, can generally be expressed as Equation 2.2 with the Kohlrausch-Williams-Watts (KWW) function and an exponential decay function:

$$E(t) = E_0\left\{A_1 \exp[-(t/\tau_1)^{\beta}] + A_2 \exp(-t/\tau_2)\right\} \qquad \textbf{(2.2)}$$

$$(A_1 + A_2 = 1,\ 0 < A_1, A_2 \leq 1,\ 0 < \beta \leq 1)$$

In this equation, E_0 is is the initial stiffness value $E(0)$, τ_1 and τ_2 are characteristic times, A_1 and A_2 are portions of the relaxation process described by the KWW function and the exponential function respectively, and β is a parameter describing the shape of the relaxation modulus. The KWW function cannot be used for all response times, since Goto et al., (1999), found the existence of a new relaxation in the short time response region $(t < 2-3s)$, which was not represented by the formulae.

Using viscoelastic material properties within numerical models is not common. The KWW formula could be implemented within a numerical stress analysis, allowing for change in bone stiffness with loading rate. Usually impact or instantaneous loading occurs on the femur, eliminating the need for the use of this stiffness relaxation phenomenon, however modelling of the hip system under non-impact style loading would require consideration of this. Hence, implant design based on impact loading is more relevant and represents a 'safer' design strategy.

2.2.2 Cancellous Bone Characteristics

2.2.2.1 Structure

Cancellous bone geometry is defined by its relative density, which in turn is related to the magnitude of loading within a specific location. In regions subject to lower loading the cancellous bone cells have lower density and are open, resembling a network of connecting rods. In more highly stressed regions the relative density increases, the rods widen, becoming more plate-like. As loading increases the relative density increases further, the plates thicken until they touch, producing almost closed cells (Ashby et al., 1988).

The alignment of the rods and plates also follow stress trajectories within the bone. The proportions of the principal stresses within the bone control the level of structural anisotropy, which adheres to Wolff's law of adaptive bone remodelling. Within the femoral head, the principal stresses are approximately equiaxial, resulting in cancellous bone structure with regular cell proportions (Ashby et al., 1988).

2.2.2.2 Mechanical Properties

Cancellous bone is mechanically and architecturally anisotropic (Corwin, 1997). The density of compact bone and individual structures that form cancellous bone is similar, forming a basis for the widely held view that the properties of the trabeculae are the same as those for compact bone. However, although cancellous and compact bone is essentially composed of the same material, voids within the cancellous bone produce vastly different mechanical properties. It is the size and location of these voids (the morphology of the cellular structure) that alter the mechanical properties. The enormous variability associated with bone creates a difficulty when predicting material properties compared to other cellular structures such as wood and foam, which exhibit similar stress-strain characteristics (Ashby et al., 1988).

Figure 2.6 shows the behavior of varying density ($\rho/\rho s$) cancellous bone under compressive loading, where ρ and ρs are the densities of the porous media and solid matrix. Compressive load applied to the low-density cancellous bone initially gives a small strain, with elastic deformation of the cell walls giving an overall linear-elastic response. This linear-elastic response terminates in the collapse of the cell walls, giving a long, horizontal plateau in the stress strain curve until the cell walls touch. Ashby et al. (1988) believes that these cell walls fail due to elastic buckling, with failure occurring according to the cell wall slenderness ratio. Obviously, long walled cells fail initially, due to their weaker bending strength. Brittle failure of the cell wall occurs when the bone is dry, and it has been suggested that elastic buckling and shear failure may also contribute to the failure of the cell walls. The stress rises steeply as cell wall collapse is prevented, caused by contact with other cell walls (Ashby et al., 1988).

Tensile loading is experimentally more difficult to measure. Exceeding 1% tensile strain, the cancellous bone trabeculae structure is irreversibly damaged, with trabeculae progressively failing as the stress-strain curve drops (Ashby et al., 1988). Tensile loading in cancellous bone generally does not occur in practice, and so is irrelevant.

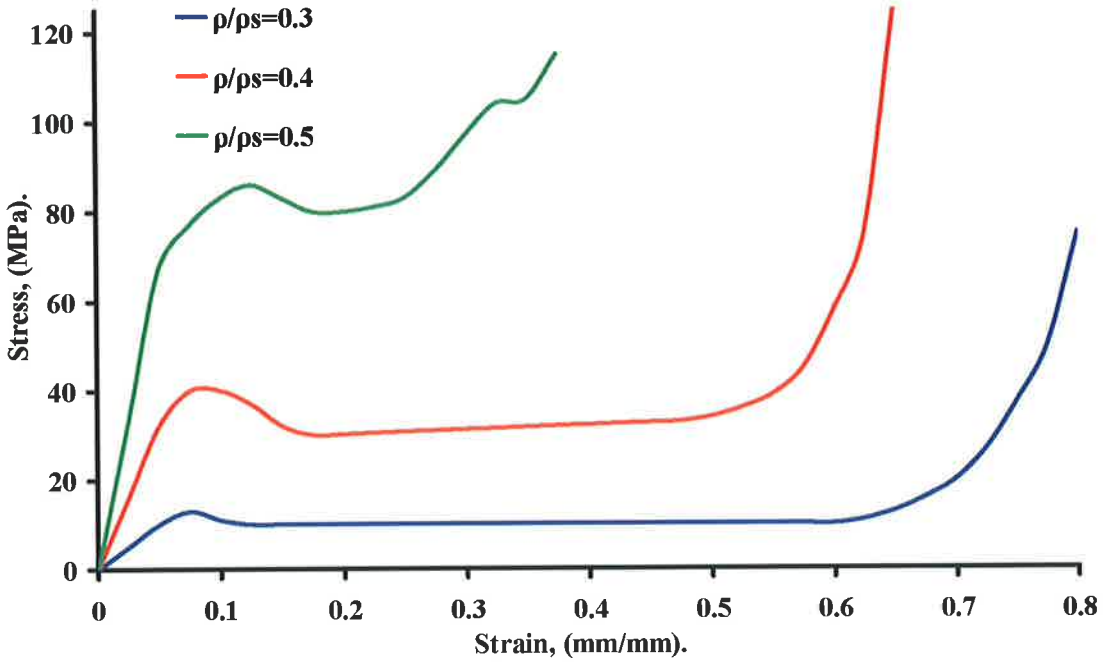


Figure 2.6: Stress-Strain curves for 'wet' cancellous bone (Ashby et al., 1997).

Data for Young's Modulus and the compressive strength of stress orientated cancellous bone plotted against density is limited, however it can be said that density is fundamental to the strength and stiffness of cancellous bone. The anisotropic nature of cancellous bone is evident from the differences in longitudinal and transverse strength (see Figure 2.5).

Morgan et al. (2001) conducted a study investigating the dependence of cancellous bone strength behavior on anatomic site. This is useful when producing site-specific finite element models. Cancellous bone material was gathered from 61 individuals, aged 67±15 years, and tested for uniaxial tensile and compressive yield properties. The compressive yield strain was greater in the femoral neck than all other sites tested. This research concluded that the yield strains for human cancellous bone differs among anatomic sites, however the yield strain may be considered uniform within a site despite substantial variation in elastic modulus and yield stress. The results from Morgan et al. (2001) can be seen in Table 2.1:

Table 2.1: Dependence of cancellous bone strength behavior on anatomic site (Morgan et al., 2001).

Anatomical Site	Mode of Loading	Apparent Density, (g/cm^3).	Young's Modulus, (MPa).	Yield Strain, (mm/mm).	Yield Stress, (MPa).
Greater Trochanter	Compression	0.22 ± 0.05	622 ± 302	0.70 ± 0.05	3.21 ± 1.83
	Tension	0.22 ± 0.04	597 ± 330	0.61 ± 0.05	2.44 ± 1.26
Femoral Neck	Compression	0.58 ± 0.11	3230 ± 936	0.85 ± 0.10	17.14 ± 6.15
	Tension	0.54 ± 0.12	2700 ± 772	0.61 ± 0.03	10.93 ± 3.08

Determining the hard tissue properties of cancellous bone using traditional methods involves machining test specimens for mechanical evaluation, however this technique is labor intensive and problematic due to possible damage caused by machining (Jacobs et al., 1999). This could explain the large strain variation in the results published by Morgan et al. (2001).

Healthy bone physically adapts to its mechanical environment. A change in load distribution and corresponding stress distribution in the remaining bone occurs folowing THA stem implantation. The volumes that experience an increase in stress may experience an increase in bone mass, while the volumes that experience a decrease in stress experience a decrease in bone mass (Joshi et al., 2000). This is referred to as adaptive bone remodelling, and is significant.

In the 1890's, surgeon and German anatomist Julius Wolff (1836-1902) discovered and published his theory of adaptive bone remodelling, commonly referred to as Wolff's Law; "The law of bone remodelling is the law according to which alterations of the internal architecture are clearly observed and following mathematical rules, occur as a consequence of primary changes in shape and stressing or in the stressing of bones". Wolff's famous book "The law of bone remodelling" was translated to English and reprinted in 1986.

After THA stem implantation adaptive bone remodelling occurs according to Wolff's Law. Usually, the bending displacements in the bone surrounding the implant are reduced due to the relatively high flexural modulus of the implant. This reduction in bending 'unloads' the outer fibres in the bone, leading to a state of stress shielding (Joshi et al., 2000).

Modelling this bone adaptation, or at least quantifying it is important when assessing implant attributes. Identification of locally high or low strain values, which may lead to bone resorption, is essential for both implant design and simulations of bone modelling processes (Duda et al., 1998).

It is widely accepted that cancellous bone geometry is a function of its mechanical environment, primarily the static loading encountered during normal activity. The geometric nature of the proximal femur generates regions of compressive and tensile stresses when loaded. Hence, the bone in the lateral side is stretched, while the bone in the medial side is compressed.

Wolff (1986) stated that bone generation "solves a mathematical problem and has given a wonderful demonstration of tension and compression lines", referring to the proximal femur. He likened bone growth to the way that an engineer builds a bridge, striving to achieve the most efficient solution, as is evident in Figure 2.7 and the corresponding schematic representation Figure 2.8. Examining larger species skeletal specimens proves that the density of cancellous structure is dependent on the required loading. Large weight transfer requires a high-density cancellous structure.

Physical experimentation is required to understand the process of bone remodelling. Early physical experimentation into disturbed static stressing of bones included influencing bone growth by fixing a length of wire between both ends of a young 'long' bone. Wolf (1986) conducted this experiment with juvenile rabbit tibias, using wires to influence bone growth over 48-51 days of developing. He found that specimens generated distortions the width of the wire, extending from the wire fixation points towards the bone extremities (Wolff, 1986). The

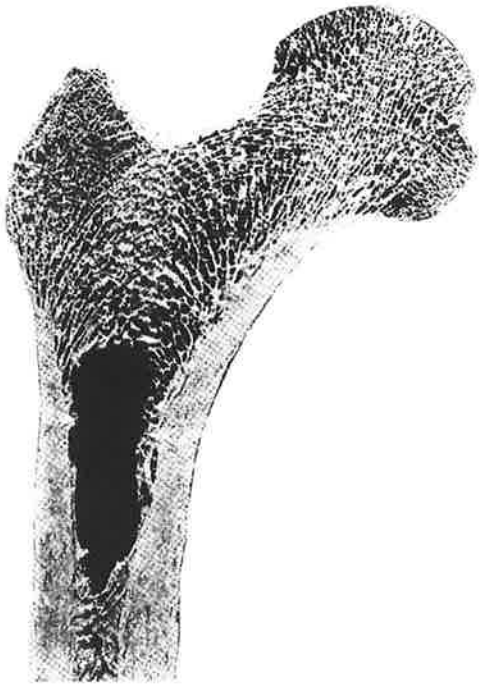


Figure 2.7: Cross sectional view through the upper femur showing cancellous bone structure (Wolff et al., 1986).

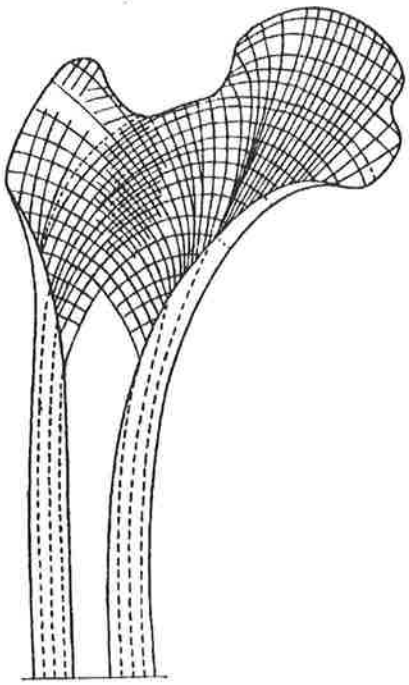


Figure 2.8: Schematic sketch of the cancellous bone structure within the upper femur (Wolff et al., 1986).

manipulated bones distorted considerably, bending permanently in the direction controlled by the wire. The profile of cancellous bone within the distorted region also changed from the normal profile in order to strengthen the bone for the unnatural loading. These bone adaptations are evident in Figure 2.9.

Another method included the use of 'du Hamel's loops' with tubular bones. 'du Hamel's loops' are metallic bands that are attached to the circular bones early in their development, and influence the diameter that the bone is allowed to grow. This manipulates localised cancellous and compact bone density. See Figure 2.10.

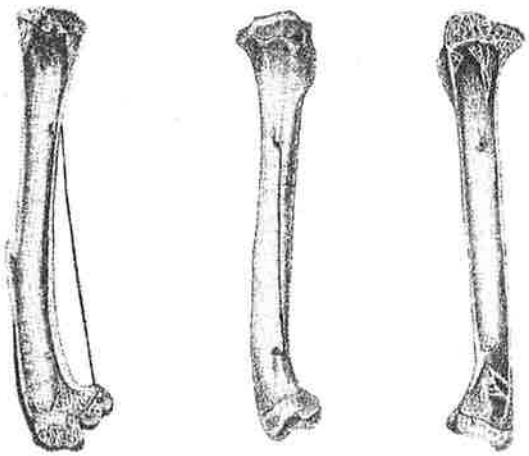


Figure 2.9: Disturbed static stressing of bones by fixing a length of wire between both ends, (Wolff et al., 1986).

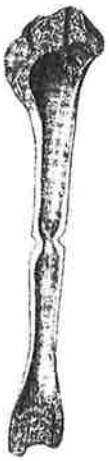


Figure 2.10: Resultant bone geomtery following the application of 'du Hamel's loop', (Wolff et al., 1986).

Kaneps et al. (1997) conducted a study in which young adult canines had their forelimb immobilised, resulting in significant loss of mechanical properties in the humerous and cancellous bone, relative to others that were not immobilized. The cancellous bone had a greater reduction in mechanical properties than the cortical bone. Some canines were remobilized for a further 32 weeks, with the final 16 weeks including treadmill exercise, resulting in complete recovery of mechanical properties. This illustrates that the adaptive nature of healthy bone is a function of its mechanical environment.

2.3 Numerical Models

Finite Element Analysis (FEA) is commonly employed for the performance prediction of components or systems when subjected to external constraints, and has rapidly made an impact in biomedical engineering applications.

Numerical modelling is particularly useful for analysing both THA components and surgical techniques. Finite element models allow analysis of in vivo situations without the need for

invasive surgery. This simulation technique allows assessment of the consequences of varying factors such as implant size, shape and placement. Short and long-term success of hip surgery depends heavily upon initial fixation; and such simulations can help orthopaedic surgeons to develop improved preoperative plans. The substantial volume and cost of these implants warrants efforts to optimize surgical results through computer simulations (O'Toole III et al., 1995).

Computer simulations can save time and money through optimising designs and reducing the need for extensive physical prototyping. Numerical modelling enables a prosthetic implant designer to reduce the product development cycle time by providing a virtual design and testing environment for analysing the device performance, confirming functionality and fatigue life without the use of human test subjects. Numerical modelling is also becoming increasingly recognised as an analysis tool by standards control groups, helping to streamline the design approval process.

2.3.1 Simplified Numerical Modelling Techniques

Simplification of the implant and surrounding mechanical environment leads to major reductions in computational effort and is often necessary in practice due to the complexity of the real system. Although the simplified system does not give an accurate representation of the real life system, it is much easier to model and faster to solve than the complex geometry of the prosthesis implanted in the femur (Gross et al., 2001). Simplified modelling is frequently conducted, and produces useful comparative information about the effects of different design features on the levels of stress in the system.

Initial simplified modelling is advantageous when introducing a new element type or solution technique. Solution trends are easily distinguished and solutions may be verified against empirical formulae when basic geometry is used. Gross et al. (2001) modelled the cement, implant and bone as isotropic materials, all with a circular cross-section, producing a method for finding the basic factors that influence stresses within the system.

Simplified modelling is useful when initially determining solution trends and model characteristics. However, oversimplification can lead to solutions not applicable to the complex real life system. The current trend is to adopt a generic femoral geometry to use when constructing simplified femoral models, maintaining solution relevance to the real mechanical environment. These models use an isotropic material to represent the cortical bone, providing more realistic geometry than a hollow cylinder. Once meshed, the solution time is not significantly higher than for a cylindrical model.

2.3.2 Modelling Femoral Bone Geometry

2.3.2.1 Generic Femoral Models

The use of a generic femoral geometry when simulating THA generates solutions that can be correlated to most individuals. One particular generic femoral geometry has been created for use in research, and made available worldwide, under the 'Standardised Femur Program' (Viceconti et al., 1996) which is shown in Figure 2.11. On September 15th, 1995, the 'Standardised Femur' model data files were made available to anyone for downloading upon completion of a transfer agreement form. This data allows every researcher to use a common geometry to generate Finite Element Models, allowing validation with other similar research (Viceconti et al., 1996).

The 'Standardised Femur' has a bone geometry that is representative of the average specimen. The 'Standardised Femur' was constructed as a 3D surface model of a femoral bone analogue (mod. #3103) produced by Pacific Research Labs (Vashon Island, Washington, USA). This geometry represents a femur with only a slight anterior bow and a fairly straight intramedullary canal (Duda et al., 1998).

The file is available in Initial Graphics Exchange Specification (IGES) format, and is composed of a Non-Uniform Rational B-Splines (NURBS) solid model of the 'Standardised Femur'. NURBS are industry standard tools for the representation and design of geometry, allowing simple importation into most commercially available codes.

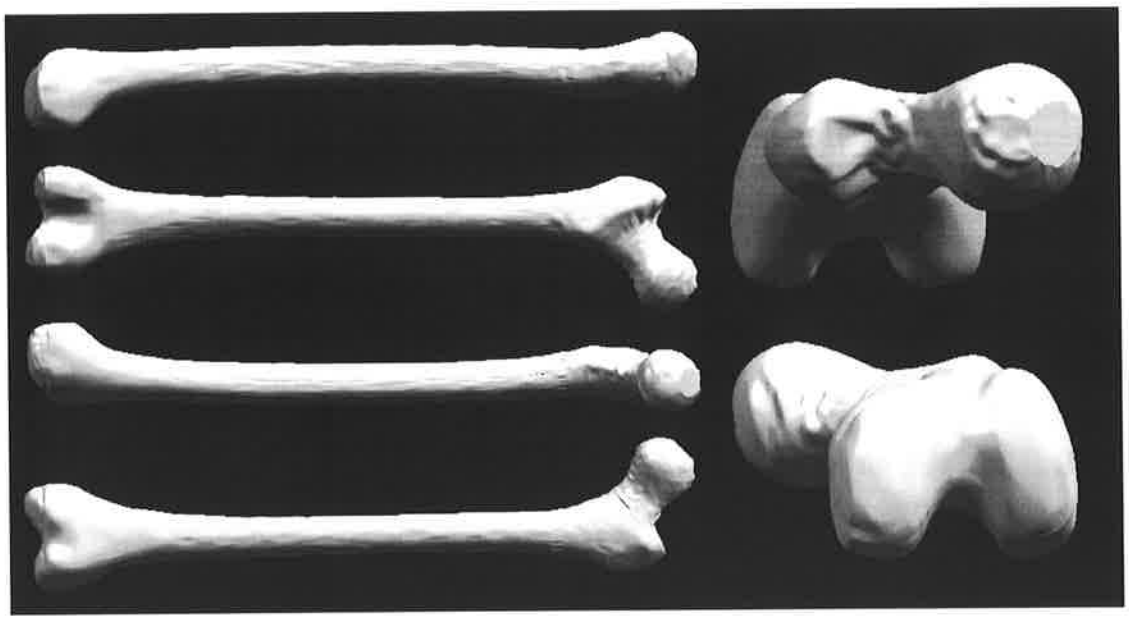


Figure 2.11: Importation of the 'Standardised Femur' into Solid Edge V9, (2000).

Common reference geometry allows for numerical studies to be replicated and made more credible (Viceconti et al., 1996). Another advantage of the 'Standardised Femur' is the large body of research previously conducted with this geometry can be used to calibrate and verify other models.

Physical models based on the femoral bone analogue (mod. #3103) are also widely used in research. This composite bone from which the 'Standardised Femur' geometry was derived is made of glass fiber reinforced epoxy, and is designed to mimic the mechanical behavior of human femoral bone. This negates dealing with biological material and sourcing appropriate speciemens, whilst developing research that can be directly compared and validated within the broader research community.

Although use of the 'Standardised Femur' geometry within research is encouraged and constructive, there are limitations. The geometry replicates only the volume of glass fiber reinforced epoxy material found in the analogue. Consequently the model's inner surface is a measure of the thickness of this composite material, and not a true representation of cortical

bone. There is no geometry representing cancellous bone, as the analogues simply have this void filled with polyurethane foam. Hence investigations into cancellous bone cannot thoroughly be made with the 'Standardised Femur' geometry.

The ultimate advancement would be to make available an average sized femur model that has both cortical and cancellous bone definition, allowing for more involved research into femoral stressing.

2.3.2.2 Subject-Specific Numerical Femoral Models

Subject-specific numerical modelling could potentially fulfill an important role within the hospital system, quickly estimating clinical outcomes of numerous surgical techniques. Subject-specific modelling of the proximal femur could possibly determine the level of stress shielding, and corresponding bone loss for individuals following THA (Weinans et al., 2000).

Subject-specific analyses generally utilise geometry obtained from computed tomography (CT scans). This spatial density data obtained using CT scans could provide the data to create models with inhomogeneous material properties. Automated conversion of CT data to numerical models would result in a simple method of establishing the most suitable implant design and implantation technique for an individual. This modelling procedure could also predict the bone remodelling process, and estimate the useful THA service life. While individual parts of this process have been 'established'remodelling, the concept has not yet been fully realised.

It has been noted that the amount of bone lost through the adaptive bone remodelling process is primarily related to the initial quantity of bone stock of the individual, illustrating the importance of subject-specific modelling (Weinans et al., 2000). This variability of bone density and subsequent bone strength between individuals could lead to substantial differences in calculated stresses and strains upon the application of generic loading. This would possibly influence the subsequent bone adaptation (Weinans et al., 2000). Therefore it is crucial to adopt

a loading scheme relevant to the specific individual if qualitative measures of adaptive bone remodelling are to be made.

Weinans et al. (2000) conducted subject-specific numerical modelling of canine femurs to determine the sensitivity of stress shielding to model loading and the bone density-elastic modulus relationship. However with constant input parameters there was little variation in stress shielding between individuals. It may be concluded that stress shielding is relatively insensitive to change in bone geometry, although in the particular subject group examined the geometry did not change significantly. However, major differences are encountered when comparing the geometry and bone density of human femurs of different age and sex. Hence when analysing a subject-specific femoral environment, subject-specific loading is also required.

Subject-specific numerical models are not necessarily required when conducting research aimed at generic trends, however it is important to be aware of the potential changes that result due to population variability. Results generated from a subject-specific model are not necessarily applicable to the general population, due to individual geometric and material properties. Conversely, no generic geometry currently exists for numerical models simulating both cortical and cancellous bone and so research investigating cancellous bone will require the generation of a subject-specific model. The introduction of a freely available generic model similar to the 'Standardised Femur' incorporating cancellous bone would be highly advantageous to the research community.

2.3.3 Numerically Modelling Bone Structure and Geometry

2.3.3.1 Numerically Modelling Compact Bone

Compact bone is usually numerically modelled as an isotropic material. Density-modulus relationships can be used to represent an anisotropic material. However this is more a collection of isotropic materials distributed throughout the model, with global rather than directional

strength characteristics. The generic 'Standard Femur' modelling requires the use of homogeneous compact bone material, as only a single volume defining the bone exists.

2.3.3.2 Numerically Modelling Cancellous Bone

Cancellous bone is commonly excluded from numerical simulations due to complexity, and in certain circumstances is of questionable worth. Masses of cancellous bone are removed during THA, limiting the amount and value of the remaining cancellous bone within a numerical analysis, unlike the intact femoral condition.

Modelling cancellous bone structure using simplistic geometries allows for the mechanics of deformation to be analysed. While this style of modelling may not be able to accurately predict material properties, obvious trends in properties varying with relative density can be discovered (Ashby et al., 1988).

A structure approximating cancellous bone can be generated through the arrangement of elements in specific patterns, to produce a porous block with a density dependant upon the relative number of elements used.

Beaupre & Hayes (1985) imitated porosity using stacked cubic cells, each containing a spherical void. The diameter of the spherical void determines the relative density. When the cubic cells containing a medium spherical void are stacked, a system of perforated plates is produced, and cubic cells with large spherical voids produce a system of rods.

Although these modular 'ideal' structures can represent porosity accurately, their generic nature is unable to replicate the strength and stiffness characteristics of real cancellous bone. Directional density parameters must also be incorporated, to provide corresponding directional stiffness qualities.

Figure 2.12.a shows the system of rods generated to imitate relatively low-density cancellous bone, while Figure 2.12.b shows the system of plates generated to imitate relatively high-density cancellous bone. These models are different to the concepts introduced by Beaupre & Hayes, as the stacking of these elements is staggered. This model allows for the analysis of bending within the cell walls (Ashby et al., 1988). Figure 2.12.c and Figure 2.12.d represent stress-orientated bone. An array of prismatic tubes within Figure 2.12.c is generated when cancellous bone is formed under axial stresses. Biaxial loading stimulates the growth of plate like cancellous bone structure in Figure 2.12.d, separated by thin spacers. The plates are orientated in the direction of the largest principal stress.

Incorporating an ideal modular cancellous structure within femoral geometry to accurately replicate the true variation of cancellous bone is impractical, and better suited to simplified geometries and loading regimes.

Another way to model cancellous bone used highly accurate 'micro-models' to duplicate the properties of cellular structures. Once the micro-model response to loading is known, it is used to develop elements within a macro model, efficiently replicating the cellular structure response.

2.3.4 Numerically Modelling Material Interfaces

Interfacial modelling is required at the boundaries between bone, cement and implant. The choice of interfacial modelling technique is important, as contact problems are highly nonlinear and require significant computer resources to solve. The method of implant fixation (i.e. cemented/non-cemented, polished/rough surface, tapered geometry) has a significant influence on the choice of interfacial modelling technique.

If interfacial solution information and load transfer is not essential, then simply changing material properties across the material interface can simply represent a fully bonded condition. This modelling technique requires the least effort.

Figure 2.12: Methods of generically modelling the cellular cancellous bone structure, (Ashby et al., 1997).

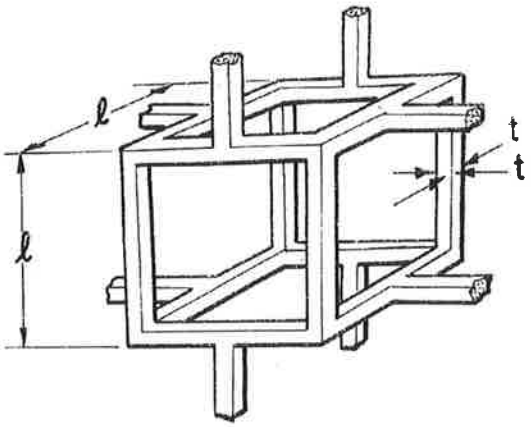


Figure 2.12.a

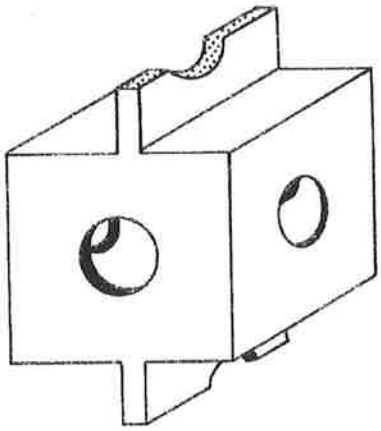


Figure 2.12.b

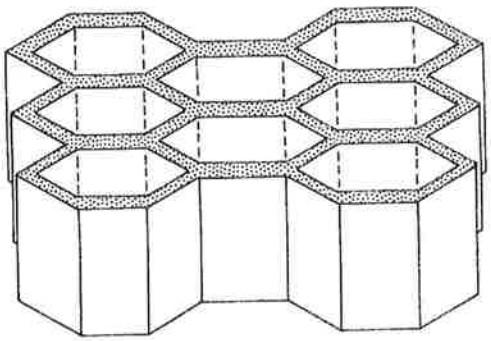


Figure 2.12.c

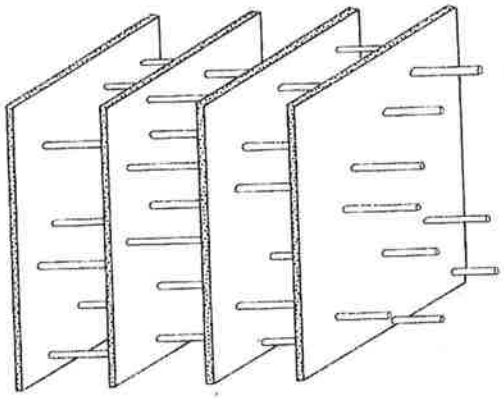


Figure 2.12.d

Contact based models have significant impediments. Regions of contact are usually unknown before the problem is solved. Surfaces can come into and go out of contact with each other in an erratic and sudden manner, depending on input parameters. Friction also needs to be accounted for in contact problems. Multiple friction laws and models exist, all being nonlinear. Solution convergence can be difficult, due to the chaotic nature of frictional response.

The two basic types of contact elements are node-to-node and face-to-face elements. Face-to-face elements are more accurate due to their flexibility in terms of modelling and simulation.

Face-to-face elements do not require structured meshes representing gap elements (Viceconti et al., 2000). The low computational demand of frictionless node-to-node contact elements makes them a good choice for explorative studies, however the micromotion predicted by these models should only be considered a rough approximation (Viceconti et al., 2000). Viceconti et al. (2000) used face-to-face contact elements to simulate the frictional contact between bone and implant and the press fit cycle. These were found to be sufficiently accurate in predicting the primary stability of a cementless implant. These results were used by Viceconti et al. (2000) to decide whether micromotion may or may not jeopardise the implant osseointergration.

Caution must be taken when modelling contact without the support of *vitro* experimentation (Viceconti et al., 2000). Experimental results allow for calibration of parameters such as normal contact stiffness and convergence tolerance, which would otherwise be unknown.

2.3.5 Numerically Modelling Femoral Loading

Accurate model loading is paramount when undertaking FEA. Unfortunately, accurate model loading is somewhat ill understood. The highly complex femoral loading system which occurs in nature is not realistically reproducible within numerical or experimental analyses. A system of equilibrium exists between the forces exerted by the soft and hard tissues of the thigh (Duda et al., 1997). Acquiring precise muscular force magnitudes and directions is difficult, which explains why the current knowledge of musculo-skeletal loading still is relatively limited (Heller et al., 2001).

Advanced investigation of issues such as bone remodelling or implant subsidence requires mandatory use of physiological loading conditions (Bergmann et al., 2001). Inaccurate or oversimplified loading generates unrealistic solutions, rendering the modelling process invalid.

2.3.5.1 Femoral Loading Cycle

Realistic loading requires replication of commonly experienced activities. Conditions that replicate walking and stair climbing should be used to test implants (Bergmann et al., 2001), as the incidence of other activities is small during normal living conditions, particularly post THA.

Dividing the walking gait cycle into steps such as heel-strike, mid-stance and toe-off allows multiple individual static analyses to be conducted rather than one computationally intensive transient solution. The loading generated by muscle forces and inertia during normal walking can reach peaks of four times the subject's body weight, generally during the heel-strike phase (Barbour et al., 1995). Throughout the gait cycle, the femur experiences alternating rather than one-sided bending when changing stages (Duda et al., 1997).

Joshi et al. (2000) attempted to generate a simplistic 'standard' loading by averaging the numerous gait cycle stages developed by Cheal et al. (1992) into a single static analysis. This is not recommended, as it produces a loading regime irrelevant to the gait cycle. Large impact loading associated with heel strike is decreased when averaged with the mid-stance and toe-off phases, reducing the peak stress and strains generated by the model. Complete walking and stair climbing gait phases are required when thoroughly analysing performance characteristics of implants. This ensures complete analysis, rather than partial stages.

2.3.5.2 Modelling Muscle Inclusion

Many muscles influence the loading of the femur, and it is not practical to include all of them within a numerical model. In the past the selection of forces to be applied to the femur during numerical and experimental studies has been somewhat arbitrary, with significant variation between various researchers (Taylor et al., 1996, Stolk et al., 2001). When the femoral bone is loaded with a complete set of thigh muscles, the strain within the bone is more or less homogeneously distributed (Duda et al., 1998). Discounting certain major muscular groups from the analysis heavily influences solutions, generating non-physiological strain distributions.

Simplistic loading is generally applied to the femur with a joint reaction force and occasionally an additional abductor muscle force, resulting in bending stresses within the femur (Taylor et al, 1996). When muscular loading is neglected, overestimation of the bending moments and shear stresses occurs and torsional effects are underestimated (Duda et al., 1998). The level of femoral bending can also vary depending on the boundary condition applied at the knee.

It is generally accepted that sizeable bending moments within the femur indicate the use of simplistic or unrealistic loading. This has been proven anatomically and experimentally. Bone naturally forms from a load in compression, not in bending. In an analytical study, Taylor et al. (1996), concluded that that if the femur was loaded in bending, there would have been either large deflections of the femoral head, or a significant degree of curvature of the femoral shaft, when the femur was loaded. This does not occur naturally, as compressive loading generates negligible deflections of the femoral head and little or no increase in the curvature of the disphyseal (mid femoral shaft) region.

Perhaps the most telling indication that the femur is not loaded in bending is its own cross section. When bone is loaded axially in compression rather than in bending, lower strains are experienced, and less material is required to bear these strains. This reduces the biological cost of bone production and energy required to move. According to Wolff's law, bending stresses would create a non-circular cross section, which is unnatural (Taylor et al., 1996). The cross section of the femur is close to circular, and this shape predominantly indicates axial loading, rather than bending.

Furthermore, the bending load that is usually depicted in models may produce unphysiological load conditions at the knee (Taylor et al., 1996).

The level of muscular inclusion within a numerical model is a function of the required accuracy and analysis type. Muscles attaching to the femur are ilustrated in Figure 2.13 and Figure 2.14. Many researchers have attempted to define the femoral loading requirements, however their

findings are often conflicting. Advanced analysis such as the bone remodelling processes distal to the lesser trochanter should consider the abductors, ilio-tibial band, adductors and hip contact (Duda et al., 1998). Inclusion of the abductors has a pronounced effect, neutralising lateral bending at heel-strike and increasing medial bending at mid-stance and push-off (Stolk et al., 2001). Lengsfield et al. (1996) found inclusion of the iliotibial tract forces has a striking influence on the results, making their inclusion mandatory. Duda et al. (1997) confirmed that if only the vasti and abductors are considered, errors in the internal load computations of up to 10% proximally and up to 200% distally, the decrease at the proximal end caused by muscles pointing in a similar direction as the abductors.

Stolk et al. (2001) concluded that additional inclusion of the iliotibial tract, the adductors and the vastii produced relatively small effects during all gait phases. This is inconsistent with other work such as Duda et al. (1998) which established that modelling approaches in the diaphyseal part of the bone should include the vasti. Duda et al. (1998) continued to find that approaches accounting for the strain distributions in the distal part of the bone should account for the role of the gastrocnemi.

Including adequate muscular activity is important. Heller et al. (1998) found that during the entire gait cycle, the overall magnitude of the principal strains never exceeded 2000 microstrain with all thigh muscles included, however principle strain magnitudes reached 3000 microstrain with simplified loading regimes. This is a large error, and when researching such phenomenon as stress shielding and adaptive bone remodelling, inaccuracies of this magnitude may invalidate results.

The influence of specific muscle inclusion on solutions should be assessed on an intact femoral model initially, to assess the degree of loading inclusion required to obtain desired solution accuracy. Once this has been established, the simplified loading can be transferred to a reconstructed femoral model for analysis. The results from the reconstructed femoral model will then be comparable to the intact femoral model.

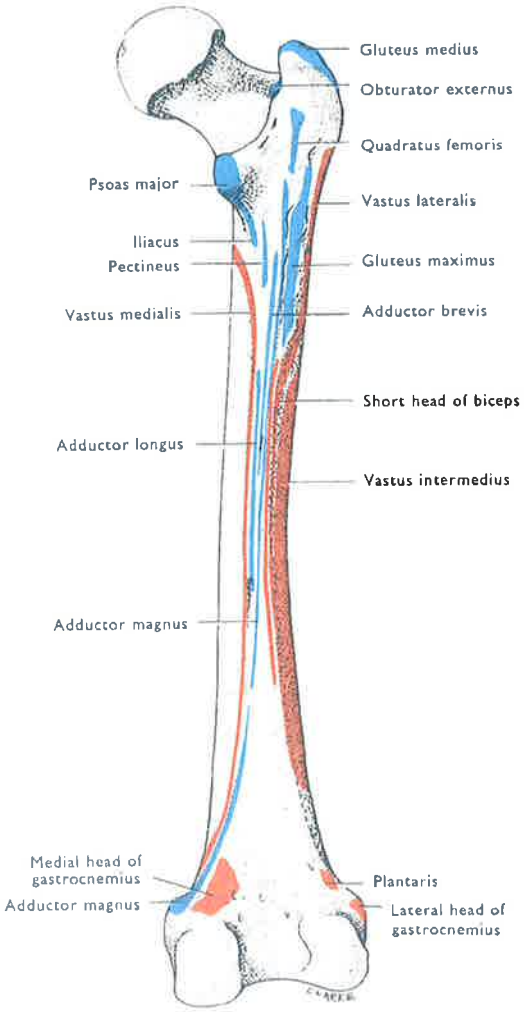


Figure 2.13: Muscular attachment areas of the femur - posterior view, (Cunningham and Romanes, 1986).

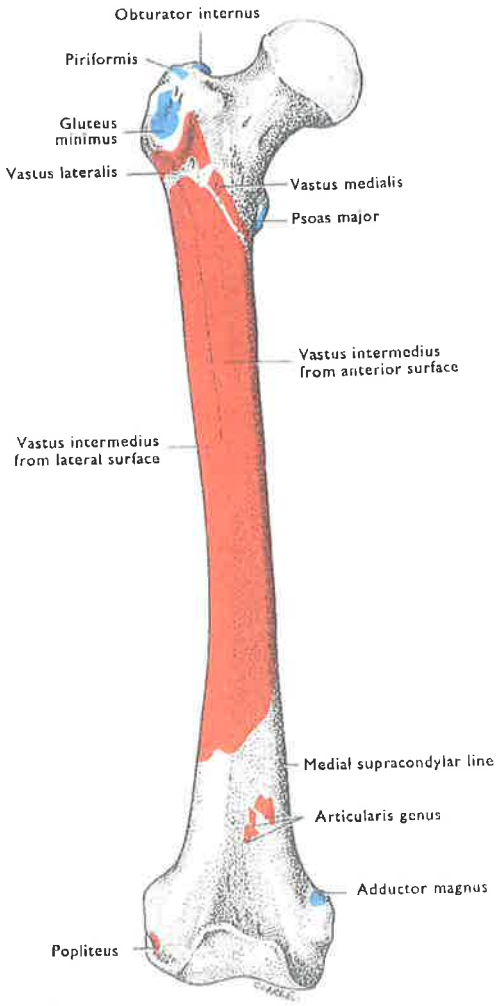


Figure 2.14: Muscular attachment areas of the femur - anterior view, (Cunningham and Romanes, 1986).

Therefore it is clear that there are conflicting views and uncertainties on the influence of muscle loading strategies within numerical modelling of the femoral system. Researching and correcting this deficiency is an important step towards improved numerical models. This issue is addressed in Chapter 4.

2.3.5.3 Femoral Loading Resulting from Muscular Wrapping

Advanced loading regimes can represent the muscles that pass across the hip without attachment to the femur. Moments are counteracted by the action of the appropriate muscles that cross the hip joint (Cheal et al., 1992). Although this seems beneficial and relatively simple to adopt, restrictions emerge. Literature clearly shows the insertion and origin areas of muscles, however contact areas are not often discussed. Furthermore, these muscles that counteract the moments within the femur under load are often located away from the bone and 'packed out' by other muscles.

Muscular loading is often applied to a specific attachment area on the femoral surface mesh. Incorporating muscles that do not attach directly to the bone requires manipulation of the values assigned to the attached muscles, further complicating the loading regime.

2.3.5.4 Femoral Joint Boundary Conditions

A restraint condition at the distal region of the femur is required to obtain a valid and meaningful numerical solution within a linear elastic finite element analysis. The accuracy of this solution is influenced by the method of restraint. Many boundary condition techniques could be employed, however the most efficient method is often the most desired. Restraint conditions range from the inclusion of articulating knee joints with rotational degrees of freedom and spring elements modelling tendons to cross sectional areas along the femoral shaft being fully fixed.

Stresses and strains in the proximal femur are of primary concern, with solution accuracy in the distal femur being of little interest. This allows full fixation of the distal end of the femur to avoid rigid body motion (Joshi et al., 2000). Complete restraint at the distal location accounts for all muscles, ligaments and tendons in the lower femur that influence the restraint and movement, thus balancing the loads within the model (Stolk et al., 2001).

Fully fixing the distal femur influences the stresses within the femur according to Saint-Venant's Principle (1855), which states that "The replacement of forces acting on a small portion of the surface of an elastic body by another statically equivalent system of forces acting on the same portion of the surface produces substantial changes in the local stress distribution but has a negligible effect on the stresses at distances which are large in comparison with the linear dimensions of the surface on which the forces are acting". Consequently with full restraint regions of excessive stress can be expected at the distal femur, however the proximal regions of interest will not be influenced.

Altering the femoral length has a significant influence on stresses within the femur. Some models include femoral material only at small distances past the base of the THA stem, however the femoral shaft must be left long enough to promote realistic deformation (Stulpner et al., 1997). Lengsfeld et al. (1996) modelled approximately 85% of the femoral length, believing it was enough to provide realistic results within the upper femoral regions (without discussion).

Element size at the distal femur can be coarser to increase computational efficiency. Complicated computationally intensive models with ligaments and distal sliding boundary conditions are not required to generate solutions within the proximal femur.

2.3.5.5 Muscular Loading Magnitude for Femoral Models

Cheal et al. (1992) published a table of muscular loading magnitudes and directions for the three phases of gait, and four other extreme loading cases. These values are used extensively within the research community, and were modified by Duda et al. (1998) to give a more accurate four-phase gait cycle, provided in Table A.2 in Appendix A.

Cheal et al. (1992) estimated each muscle force by assuming a constant relationship of 40 N/cm^2 for the maximum muscle force as a function of the cross sectional muscle area. These cross sectional dimensions were obtained from available literature.

Development of a numerical model based on the 'Standardised Femur', which replicates the average femoral geometry, requires scaling of the muscular load magnitudes supplied by Duda et al. (1998) if they are to be considered accurate. This scaling is based on the individual's weight.

2.3.5.6 Modelling Muscular Load Attachment to the Femur

In the body, muscles connect to the bone over a specific area, referred to as the attachment area. The method employed to transfer muscular loading in numerical models influences the solution. Currently, most femoral models apply the individual muscular forces to single nodes approximating the centroid of the attachment area. A more accurate but involved process is to distribute the muscular loading over nodes contained within the attachment area. Various tendon insertions extend over sizeable areas, and subsequent analyses of muscle-bone interactions are sensitive to attachment location and geometry (Duda et al., 1996).

Joshi et al. (2000) applied a distributed loading over surface nodes at the appropriate location on the model. This method eliminated stress concentrations caused by localised forces, and developed a more natural loading.

Obtaining a perfectly distributed muscular load is not possible, as muscle attachment areas vary in size and location between individuals. Many models use muscle attachment centroids sourced from anatomical books, however these anatomical views are often not to scale, having limited value (Duda et al., 1996).

The use of a generic set of muscular attachment locations is possible, however the wide range of anatomic variability suggests a mean data set is artificial and may not be biomechanically meaningful (Duda et al., 1996). In a study of anatomic variability, Duda et al. (1996) found that standard deviations (as a percentage of the mean) were about 70% for attachment area and 80% for muscle volume and attachment centroids location.

Realistically, there is no choice but to use generic attachment data, however it is important that models which are used to investigate musculo-skeletal relationships should respect attachment location variability (Duda et al., 1996). It is highly advantageous to distribute the muscular loading over the relevant attachment area, as simplistic point loading is inaccurate. It would be advantageous if an accurate set of attachment location data were made available for the 'Standardised Femur', allowing accurate model loading globally.

2.3.5.7 Changes in Femoral Loading Post Implantation

Removal of bone (femoral head and neck) is required to implant the THA stem, resulting in an altered loading regime. It is possible that some numerical models using relatively advanced loading procedures will require changes to suit the removal of bone material.

Some muscles are totally severed during surgery, and are assumed never to function again. Other muscles are partially severed, but heal almost totally. This change in muscular groups should be taken into account when modelling.

Loading, usually applied through the center of the natural femoral head, is changed to the center of the ball attached to the end of the THA stem. Sometimes this location is slightly different to the location of the center of the natural femur's head, and so amendments must be made to load magnitude and direction. Joshi et al. (2000) used an additional coupled load applied to the end of the trunion (THA stem neck region, between the ball and stem), calculated to correspond to the loading on the artificial femoral head of the same size and in the same location as the natural femoral head. It is generally accepted that loading post THA causes an offset relative to the natural loading on the femoral head (Joshi et al., 2000).

2.3.6 Choosing and Calculating Resultant Quantities

Results obtained from the numerical analysis of implanted femoral models range from stresses within the implant, to the decrease in femoral bone mass within particular locations due to stress shielding.

Usually the femoral model is divided in the lateral-medial and anterior-posterior planes, and numerous times in the anterior-posterior direction to generate specific volumes of bone. This allows for averages of quantities such as strain to be compared between models with identical divisions.

2.3.6.1 Mechanical Failure

Fractures in bone, cement or THA stem can occur. Mechanical failure of the isotropic cement and implant can easily be predicted from the stresses within the material. However using stresses within the bone to predict failure is inaccurate for a number of reasons; the anisotropic nature of bone results in varied yield strength with load direction and location of interest.

2.3.6.2 Stress Shielding of Femoral Regions

Post THA, implanted femoral model results defining stress shielding illustrate a change in some quantity (such as stress or strain) relative to the original intact femur value under natural loading. Many researchers predict the level of stress shielding by examining the level of stress within the implanted femoral cortical bone, assuming that changes in magnitude of the principal stresses from that of a naturally stressed intact femur lead to excessive bone loss due to adaptive bone remodelling (Cheal, 1992).

Von Mises Stress is commonly used to demonstrate the loading on the femoral bone. The Von Mises Criterion, also known as the maximum distortion energy criterion, octahedral shear stress theory, or Maxwell-Huber-Hencky-Von Mises theory, is often used to estimate the yield of ductile materials. The Von Mises criterion states that failure occurs when the energy of

distortion reaches the same energy for yield or failure in uniaxial tension. This calculation is limited to the shear loading failure of ductile materials, and so is not strictly applicable when investigating femoral bone geometry with such a system of loads and materials.

The limitations of Von Mises theory, along with the abundance of *in vivo* results that can only be measured in strain, leads to the use of principal strains (magnitude and orientation) to adequately represent the resultant femoral loads (Duda et al., 1998). Researchers are increasingly adopting the use of strain in preference to stress as a measure of loading.

A more advanced measure of bone loading is 'Strain Energy Density' (SED), which is used for comparative strain analysis in bone (Lengsfield et al., 1996). Stress shielding can now be more accurately defined as the decrease in strain energy per gram of bone mass in the implanted femur relative to the intact femur (Weinans et al., 2000).

The most advanced measure of stress shielding is the 'Stress Shielding Signal' (SSS), as used by Weinans et al. (2000). The change in strain energy of the implanted bone relative to the reference bone was used as the stress shielding signal. The SSS introduced by Weinans et al. (2000) is expressed in Equation 2.3 as:

$$SSS = \left[\frac{SE_{(imp)} - SE_{(ref)}}{SE_{ref}}\right] \quad \textbf{(2.3)}$$

Where SSS refers to stress shielding signal, $SE_{(imp)}$ refers to strain energy within the implanted femur and $SE_{(ref)}$ refers to strain energy within the intact femur. The strain energy SE is the strain energy density divided by the apparent density.

This stress shielding signal uses the SED divided by the localised bone density. This is only useful when using non-isotropic bone material properties; otherwise change in SED can be used as a stress shielding signal.

2.3.6.3 Quantifying THA Stem Loosening

Implant stability is a function of its interfacial properties, particularly the stresses. Cheal (1992) investigated femoral component loosening by analysing the shear stress at the implant-bone interface, assuming that excessive shear stress leads to mechanical instability of the implant.

Implant stability is also a function of the bone and cement (if cemented THA) integrity. Therefore cement and bone stresses approaching or exceeding the yield strength influence structural integrity, and can be correlated to implant loosening.

2.3.7 Femoral Model Mesh Characteristics

Generating an ordered mesh allows for simplified result collection, and generally a more stable model. Automatically generated meshes are easily produced, however element size and shape can be hard to control. Consequently, mesh generation for bone models is often performed manually, due to model construction technique.

Mesh density, solution time and model complexity depend mostly upon the required solution accuracy. The nature of analysis and element type also can influence the level of mesh refinement. Lengsfield et al. (1996) found that refining mesh density from 2500 nodes to 7000 nodes within a section of femoral shaft produced nearly identical results for a simple linear static analysis.

Complex models used to investigate parameters such as interfacial shear stresses require a more planned mesh. Sensitivity to mesh alterations is of great importance. Failure predictions, based on the level of stress within the cement and material interface, have a high level of uncertainty due to the sensitivity to mesh density (Stolk et al., 1998).

The main issue associated with mesh refinement arises when comparing various models. When evaluating different prosthetic designs, they should be compared using models with the same

level of mesh refinement (Stolk et al., 1998), or models that have had their mesh density confirmed sufficient to provide accurate solutions. Coarsely meshed models may provide accurate solutions however these should be checked against more refined meshes to determine if significant mesh density related error exists.

2.3.8 Solution Accuracy

Generating accurate solutions from numerical modelling of the implanted femoral environment is difficult. The level of accuracy is hindered severely by inherent model limitations.

Model loading, material properties and geometry all influence solution accuracy. Subject specific analyses require detailed geometry and material properties, to give a solution that is only as accurate as the applied loading permits. The possibility of accurately predicting the amount of bone adaptation caused through stress shielding associated with a specific implant design is small, but will increase in the future.

A more sensible solution technique for analysing the stress shielding characteristics of various THA stem designs is to use generic bone geometry with isotropic material properties. Although the numerical solutions may not be accurate, the difference between various designs will demonstrate solution trends. These solution trends are valuable in distinguishing various implant characteristics.

As with all numerical modelling, overall accuracy is proportional to the expense invested. Currently, solution trends are adequate for determining the characteristics required for producing and choosing between the many implants and implantation techniques available.

2.3.9 Numerical Optimisation Techniques for THA Stem Analysis

Conventional THA requires femoral head and neck removal, replacing them with an implant that is anchored within the upper femoral shaft. Following THA, all loading transferred between

the femur and the pelvis must pass through the implant/femur interface, causing vastly different loading within regions of the upper femoral shaft when compared to the intact natural state. Regions within the implanted upper femoral shaft are either under-stressed or over-stressed relative to the intact condition, both of which can be detrimental to THA service life.

THA stem design is complex, requiring the collaboration of engineers and surgeons, (Pawlikowski et al., 2003), and design improvements rapidly achieved through the application of engineering analysis (Crowninshield et al., 1980). Technology permits an extension of THA service life through alteration of THA stem characteristics.

When comparing both cemented and uncemented stiff THA stems of the same material, previous studies indicate that the inclusion of deformable polymer cement reduces the level of stress shielding and corresponding bone resorption (Katoozian et al., 2001), which in turn shortens THA service life.

THA stem stiffness is a crucial design variable governing load transfer (El-Sheikh et al., 2002) which in turn dictates the long term success of THA due to interfacial loosening and bone loss (Katoozian et al., 2001) caused by stress shielding.

Increasing THA stem stiffness reduces the loading transferred to the bone within the proximal femur (Gross & Abel 2001) while decreasing THA stem stiffness increases the loading transfer to the bone within this region reducing stress shielding and corresponding bone loss (El-Sheikh et al., 2002, Huiskes et al., 1992, and Katoozian et al., 2001).

However, as THA stem stiffness decreases to reduce stress shielding, proximal interfacial stresses increase (Huiskes et al, 1992) and stresses within the implant itself decrease (El-Sheikh et al., 2002). This increase in interfacial stressing associated with more flexible THA stems is of concern because maximum cement stresses occur proximally (El-Sheikh et al. 2002). Increasing these stresses enhances the risk of cement failure (Gross & Abel 2001) and

interfacial de-bonding and micro-motion, possibly corresponding to a higher stem loosening rate (Huiskes et al, 1992). Hence, by simply decreasing THA stem stiffness it is not possible to achieve a totally satisfactory compromise between low stress shielding and low cement stresses (Gross & Abel 2001).

Selection of candidate THA stem materials excludes many due to high strength requirement (Chang et al., 1998), expense, manufacturability and biocompatibility. A reduction in THA stem stiffness using traditional materials can be achieved by using a hollow design. Hollow stems allow a reduction in stress shielding and provide potential for incremental improvement of existing THA stem designs (Gross & Abel 2001). Mattheck et al., (1990) verified the reduction of stress shielding associated with using a hollow THA stem, finding decreases in stresses below the distal prosthesis tip and increased proximal cortical bone stresses.

2.3.9.1 Composite Materials and Optimisation

Recently, composite materials have been employed within biomedical devices and implants, and although biocompatibility issues have not been undisputedly proven, they may be the material of choice in the future (Simões & Marques 2001).

The manufacture of THA stems using composite materials allows increased design flexibility. Traditional metal devices are commonly replaced with composite materials, and possibly the biomedical field may follow the aerospace industry where composite materials are prevalent, replacing high performance metals and outperforming them (Simões & Marques 2001).

In an attempt to meet a compromise between stress shielding and migration, Simões et al., (2000) designed a prototype controlled stiffness THA stem utilising a stiff cobalt-chrome core surrounded by a flexible composite outer layer. The stem stiffness was controlled by altering the thickness of the outer composite layer, however manufacturing a hip prosthesis using composite technology with a highly differentiated modulus proved difficult.

Another composite THA stem is the PM uncemented isoelastic THA stem, produced by Rob Mathys Co, (Bettlach, Switzerland) from polyacetal resin with a steel core. The PM uncemented isoelastic THA stem has similar elasticity as bone (Niinimäki et al, 1994), designed to theoretically allow the THA stem and bone to deform as one unit and promote bone formation through avoidance of stress shielding (Niinimäki et al, 1994).

Niinimäki et al., (1994) conducted a 114 subject clinical trial using the PM uncemented isoelastic THA stem with a mean follow up of 8.2 years. At revision time only 71 of the original THA's were available for follow-up, and of these, 31 had either good or excellent functionality, 16 were fair and 24 were poor. Also, 21 of the 71 stems were radio-graphically judged to be loose, which is a poor result (Niinimäki et al, 1994). It is believed that superior mechanical matching of the isoelastic material is required to fulfil the advantages of the design (Niinimäki et al, 1994).

2.3.9.2 Numerical Modelling as a Tool for Optimisation

Using optimisation techniques within numerical analysis and design of THA stems allows improvements in stress shielding and interfacial stresses by manipulating THA stem design variables such as geometry and material characteristics. Design optimisation requires the construction of a model using design variables that have allowable ranges, the allocation of model limitations and an objective function that seeks the design variable values that return the optimal result. Importantly, other factors such as manufacturing and surgical techniques require consideration when designing THA stems (Huiskes & Boeklagen 1989).

THA stems can be optimised with numerical techniques to reduce and smooth THA stem-bone interfacial stresses by means of a stress analysis (Katoozian et al., 2001) and altering well defined design variables (Huiskes & Boeklagen, 1989) such as THA stem and cement material properties, surface finishes and geometries (Katoozian & Davy 2000). In order to achieve a THA stem design that satisfies design objectives, the objective function need not be a

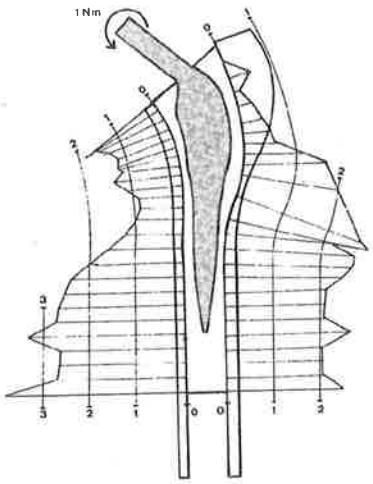
quantitatively accurate function, as a qualitivley accurate function suffices (Kuiper & Huiskes, 1997).

2.3.9.3 2-Dimensional Optimisation within Numerical Modelling

Optimisation of THA stems using 2-dimensional numerical models has the advantage of simplification through the elimination of enormous mathematical complexity associated with 3-dimensional structures (Crowninshield et al., 1980). However, this simplification neglects many structural aspects (Huiskes & Boeklagen, 1989) such as geometry and loading that cannot be adequately represented with a 2-dimensional analysis (Crowninshield et al., 1980).

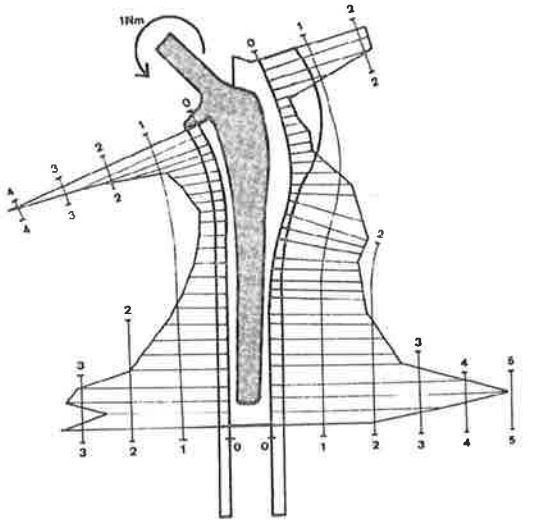
Huiskes & Boeklagen (1989), conducted a 2-dimensional numerical optimisation analysis aiming to minimise SED (strain energy density) peaks within the cement near the cement/bone interface through manipulation of implant shape. This research found that a 30-70% reduction in cement stresses near the bone/cement interface could be achieved with the optimal THA stem geometry relative to traditionally shaped THA stem. Results for the optimally shaped THA stem with proximal and distal tapers and a belly-shaped mid-section can be seen in Figure 2.15, while results for a traditionally shaped THA stem neglecting collar/bone contact can be seen in Figure 2.16.

Kuiper & Huiskes (1997) investigated the optimisation of material stiffness within a cementless THA stem using a 2-dimensional numerical model to minimise the probability of interface failure while also limiting the bone resorbtion caused by stress shielding. The 2-dimensional numerical model can be seen in Figure 2.17 showing non-homogeneous bone density distribution and load cases, and the resulting optimal THA stem stiffness distribution with a resorbed bone mass fraction of 7.5% and corresponding interfacial failure index in Figure 2.18. These results indicate that a non-homogeneous THA stem allows the transfer joint loading to bone without alarming interfacial stress levels associated with traditional THA stems (Kuiper & Huiskes, 1997).



$(SED \times 10^{-13} Nmm^{-2})$

Figure 2.15: Optimal THA stem geometry and resulting SED within the cement found by (Huiskes & Boeklagen, 1989).



$(SED \times 10^{-13} Nmm^{-2})$

Figure 2.16: Traditional THA stem geometry with no collar/bone contact and resulting SED within the cement found by (Huiskes & Boeklagen, 1989).

Kuiper & Huiskes (1997) found that their model produced an optimal THA stem that was relatively stiff at the proximal end, with stiffness that gradually recedes towards the distal end. This stiffness distribution can be thought of as having a proximal 'belly' (Kuiper & Huiskes, 1997), which is similar to the results obtained by Huiskes & Boelagen (1989) where the reducing distal THA stem diameter is equivalent to a reduction in material stiffness.

Advancement over some basic 2-dimensional models can be achieved using a 3-dimensional axi-symmetric model which has a computational expense far less than a full 3-dimensional analysis. Yoon et al., (1989) used a 2-dimensional numerical model checked by a 3-dimensional axi-symmetric model to optimise THA stem geometry with the goal of minimising stresses within the cement. Rahman (2000) conducted THA stem geometrical optimisation using entire simplified axisymmetrical femur geometry with non-axi-symetrical loading, which further

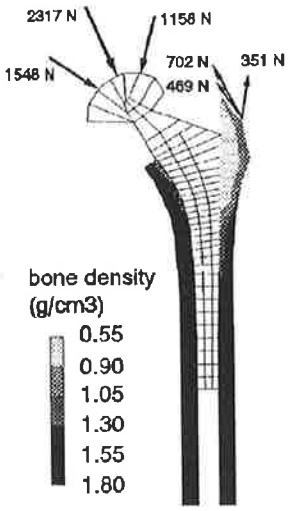


Figure 2.17: 2-dimensional numerical model employed by Kuiper & Huiskes (1997), showing load cases and non-homogeneous bone density distribution.

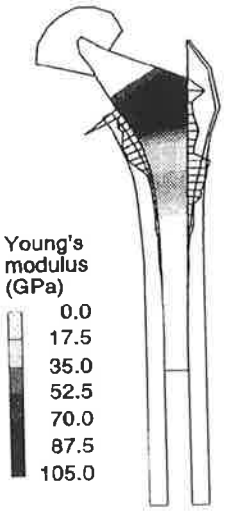


Figure 2.18: Results showing THA stem-bone interfacial failure index and optimal THA stem stiffness distribution for a resorbed bone mass fraction of 7.5% (Kuiper & Huiskes, 1997).

increasing solution accuracy whilst being numerically efficient. This is only suitable for axi-symmetric models.

2.3.9.4 3-Dimensional Optimisation within Numerical Modelling

Increased accuracy associated with more 'anatomical' 3-dimensional models have the disadvantage of increased complexity and expense (Huiskes & Boeklagen, 1989). The *in vivo* femoral system has complex geometry, materials and loading that requires a very thorough analysis to evaluate response to implant technology (Chang et al., 1998), and this enhanced model realism expense easily justifies the increased computational expense (Katoozian & Davy 2000).

Katoozian & Davy (2000), used a 3-dimensional numerical model to undertake a THA stem shape optimisation to smooth interfacial stresses. This research found that improvements in

bone and cement stresses occur with the optimal THA stem geometry, which was wide and wedge-wedge shaped in the proximal region, and tapered distally. Pictures of the 3-dimensional implanted model, along with initial and optimal THA stem designs can be seen in Figure 2.19.

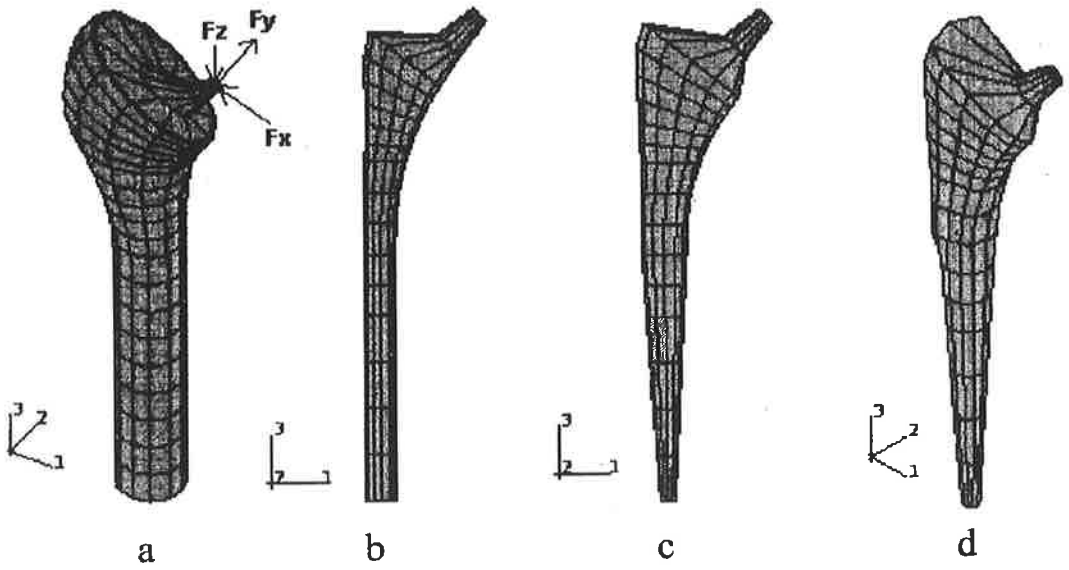


Figure 2.19: Model meshed used by Katoozian & Davy (2000): (a) 3-dimensional model with joint loading; (b) initial implant geometry; (c) anterior-posterior view of the optimal implant geometry; (d) isometric view of the optimal implant geometry.

One limitation of the model developed by Katoozian & Davy (2000) is the exclusion of muscular loading. It is believed that loading conditions contribute significantly in determining optimal THA stem geometry within numerical optimisation (Hedia et al., 1996). Models with simple joint loading developed by Katoozian & Davy (2000) found that differences in optimal solutions with generated with ranging loading conditions were greater than those with different optimisation objective functions. This demonstrates that realistic model loading is paramount when conducting optimisation analysis.

2.3.10 Modelling Adaptive Bone remodelling

Numerically simulating the adaptive bone remodelling process is highly complicated. The mathematical laws that govern bone remodelling in a local state of stress and strain are still under investigation, achieving an accurate solution is challenging. Calibration of these modelling methods also requires experimental data that is particularly difficult to obtain.

Stulpner et al. (1997) created an adaptive bone remodelling technique for an intact femur with a simplified loading condition representing the gait cycle, using only an abductor muscle tensile force, femoral head reaction force and fixed proximal boundary condition. This model showed the ability to generate bone adaptation, however inaccurate and incorrect results were a product of the overly simplified loading. The model generated bone characteristics that are not observed in reality, highlighting the need for accurate model loading and boundary conditions.

Absolute solutions may not be achievable when dealing with the quantities of bone adaptation; consequently solutions may tend to be more of a qualitative nature. In addition, the value of simulating the adaptive bone remodelling process may be minor as direct correlations between bone adaptation and change in strain energy density can easily be achieved.

2.4 Literature Review Summary

Examination and evaluation of the current published literature suggests that although numerical models of intact and implanted femoral systems exist and serve as tools in the assessment and design of THA stems, uncertainty and conflicting opinions surround much of the model parameters.

This research endeavours to investigate and resolve these uncertainties and conflicting opinions by conducting a series of staged numerical studies including:

- Assessing suitability of intact numerical femoral models, both sourced and generated, for use as a tool within THA stem assessment and design. This includes distributed material property allocation.
- Discovering the required intact and implanted numerical femoral model load parameters, including choice of loadstep, level of muscular load inclusion, influence of distributed muscular loading and boundary conditions at the knee.
- Assessing commercially available THA stems with differing geometry and surface finish for their stress shielding characteristics, using the previously suggested suitable intact numerical femoral model.
- Conducting optimisation analysis on the THA stem previously discovered to exhibit the most favourable stress shielding characteristics, providing superior stress shielding characteristics through manipulation of material stiffness.

Investigation of the above mentioned issues within this research holds significant value to the international research community, allowing others to maximise the potential of their research and further advance implant technology. Improved THA stem bio-compatibility and service life is of paramount importance to all, offering reductions to physical pain and suffering, and financial load to healthcare systems.

Chapter 3

PRELIMINARY NUMERICAL MODELLING OF THE INTACT FEMORAL SYSTEM

3.1 Introduction

Prior to major investment of resources in the development of a detailed numerical femoral model, creation of an initial simplistic model was undertaken. In addition to providing familiarity with the numerical software, the purpose of the initial simplistic model was to uncover potential issues that may impede future work. These issues may arise from software deficiencies, model characteristics or other previously unidentified factors.

Knowledge discovered in this initial modelling procedure assisted in the generation of more detailed numerical models with an increased degree of confidence. Hence, the development and analysis of a 'cheap' generic initial model provided direction for the efficient construction of a superior model for future use within this research.

3.2 Research Aim

The aim of this initial research was to ascertain and provide solutions for major modelling limitations experienced using the available numerical research tools. This investigation intended to provide specifications required to efficiently develop a numerical modelling technique that is accurate and relevant to the intact femoral system.

3.3 Preliminary Intact Femoral Model Construction

Model geometry acquisition is an important element within the simulation process. A generic style of geometry is desired for this initial modelling, endeavouring to eliminate factors associated with geometric detail irrelevant to the research objective.

3.3.1 Model Geometry Generation

Initially, thought was given to establishing a simple model of circular cross-section. However, after initial modelling of this nature, a more natural geometry was sourced to enable comparison of generated results with other research.

This more natural generic geometry is based on the 'Standardised Femur' developed within the 'Standardised Femur Program' (Viceconti et al., 1996). Using this geometry provides a model similar to the 50^{th} centile human male femur that is generally accepted within the research community. This geometry was downloaded free of charge in an IGES format following the completion of an online registration form.

This geometry was initially imported directly into ANSYS V5.7.1. (2002), however small details within the geometry, mainly due to inappropriate surface features, presented problems when attempting meshing. Removal of these details was necessary to create a geometry that was more compliant with the automated meshing procedures.

Removal of surface features was conducted using Rhinoceros V1.1. (2000) NURBS modelling software. The solid model was stripped to the 'wire frame' line components representing the cross sectional slices recorded during computer tomography scanning of the original bone analogue component. Once this set of lines was exposed, new surfaces were mapped over the lines to generate new external and internal surfaces. This can be seen in Figure 3.1.

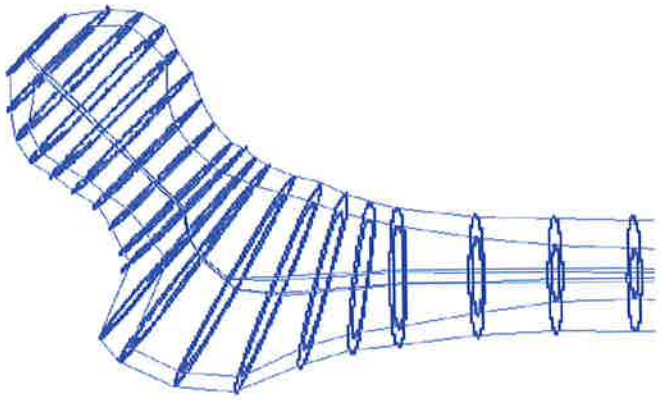


Figure 3.1: Internal and external contours defining the geometrical 'wire frame', (Rhinoceros V1.1, 2000).

These newly developed surfaces required further manipulation. A smoothing algorithm was applied to eliminate the sharp edges within the surfaces. This smoothing algorithm generated a set of surfaces that represented smooth inner and outer surfaces for the cortical bone. This can be seen in Figure 3.2. The level of smoothing was sufficient to eliminate irrelevant surface details while maintaining a generic style femoral geometry. These surfaces were then saved in IGES format.

Solid model construction was undertaken using Solid Edge V9. (2000) software. Solid Edge V9. (2000) enabled the surfaces to be joined and a solid model created. This solid model looked similar to the initial 'Standardised Femur' geometry, however contained none of the details that caused meshing problems. This solid model resembles a generic cortical bone geometry that is numerically robust.

3.3.2 Model Meshing

To assist the meshing process, the majority of the bone volume was separated into many volumes, each with 8 sides. This volume division allows simplistic meshing with 8-sided

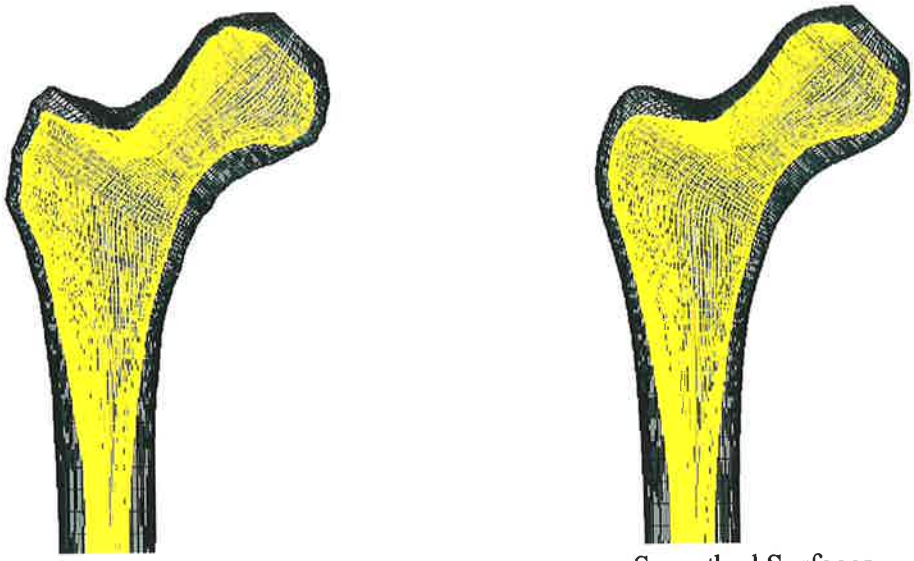


Figure 3.2: Smoothed and unsmoothed model surfaces, (Rhinoceros V1.1., 2000).

hexahedral 'brick' elements. Although automatic meshing techniques are viable, element shape control was found to be superior when manually meshing. This manual meshing procedure resulted in the allocation of eighteen second-order hexahedral brick elements within each separated bone volume, with a resolution of two elements across the bone thickness.

The femoral head geometry was meshed with tetrahedral elements primarily due to shape considerations, although hexahedral elements could have been used with additional effort. If required, meshing with hexahedral elements could be employed in the future.

Second-order elements are utilised within the entire bone volume mesh. Second-order elements are capable of representing the complex femoral geometry more accurately than more simplistic first-order elements, and were chosen accordingly. This mesh is provided in Figure 3.3.

Solution time for this mesh density is minimal, allowing further mesh refinement if required.

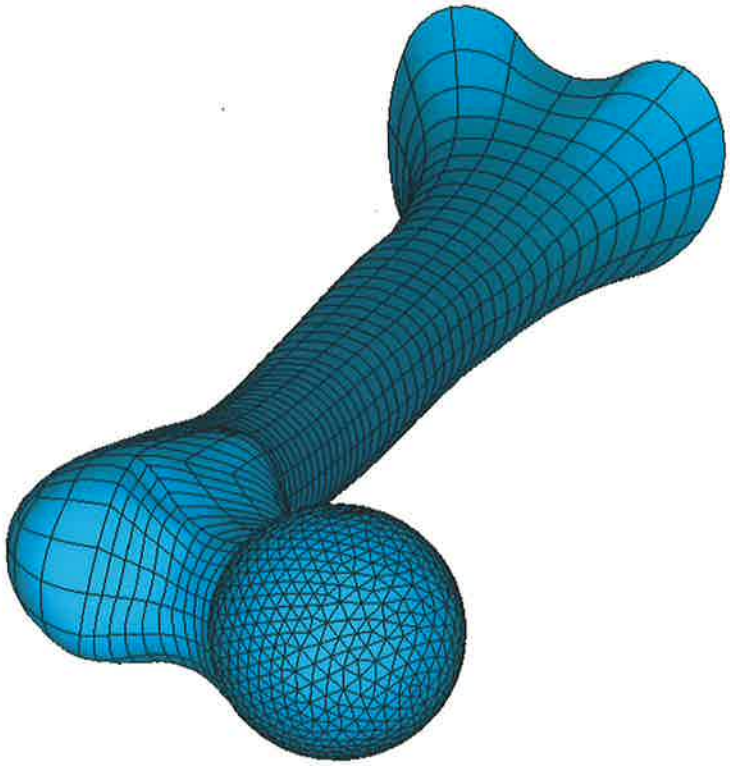


Figure 3.3: Smoothed mesh including second-order hexahedral 'brick' elements in the femoral neck and shaft, and second-order tetrahedral 'brick' elements in the femoral head, (ANSYS V5.7.1., 2002).

3.3.3 Material Characteristics

The material properties allocated within the model are a function of the information provided by the geometry. As described in the literature review, the 'standardised femur' geometry provided is that of a hollow synthetic bone replica. As such, the meshed volume in the model has no information or contrast in material data, and so a homogeneous material is used throughout the entire model.

This homogeneous material was assigned a Young's Modulus of 17 GPa and a Poisson's Ratio of 0.3 (Ashby et al., 1997). There is no cancellous bone in this model, as the inner volume is

unmeshed. Although somewhat unnatural, this assigned material will deliver a solution adequate for initial modelling purposes. Material property refinement can follow if required.

3.3.4 Model Loading

Femoral loading information provided by Duda et al. (1998) is extensive, and composed of the four load conditions experienced during the gait cycle. This initial modelling uses only the 45% gait cycle loading regime, as published results exist for this load regime applied to a model also based on 'standardised femur' geometry. Use of this loading regime will allow comparison of results generated from both models.

The individual muscular load data provided by Duda et al. (1998) includes directional components of force and coordinates for the point of application of the load on the femoral surface. To use this data, the model must first be orientated in the same coordinate system described by Duda et al. (1998).

The muscular forces are applied to the model as individual directional nodal forces. A program was developed to select the node located on the exterior surface of the model with the closest proximity to the location of each muscular load. The extremely close proximity of model surface nodes to muscular load locations indicated accurate model alignment and geometry.

All muscular forces provided by Duda et al. (1998) were included in this model, although some seemed to impart little loading. Refinement and improvement of model loading will follow in a model sensitivity analysis.

All nodes at the distal end of the femoral model were restrained in all degrees of freedom.

3.3.5 Model Solution

The linear elastic material properties allocated to all elements coupled with the static nature of the model provided a very short solution time. This minimal solution time allows high levels of mesh refinement if required.

3.4 Model Validation

Model validation is achieved through comparison of results with Duda et al. (1998) with identical muscular load inclusion. Duda et al. (1998) provides resultant principal strains for a quality femoral model under comprehensive muscular loading for the 45% gait cycle loading regime.

Comparison of the model with that of Duda et al. (1998) required the construction of three paths on which the resultant quantities are recorded. Duda et al. (1998) recorded the maximum and minimum principal strains as a measure of femoral load state, necessitating the extraction of these quantities from the model.

The three paths were used by Duda et al. (1998) to examine the magnitude of femoral loading with varying muscular inclusion parameters, and are adopted within this model. These paths are constructed through connection of adjacent nodes along the anterior, medial and lateral exterior surfaces of the upper region of the femur.

Although Duda et al. (1998) placed the three paths on the exterior surface of the femur, the midsection of the cortical bone was chosen as the location along which to record results within the current preliminary model. This is advantageous in that it somewhat isolates the region being analysed from the effect of localised muscular surface nodal loading. Current mesh density means that it is highly likely a surface node with an associated muscular loading is included in a path if it were located on the surface. This would disrupt the results extracted from the model.

Results are extracted through selection of all nodes that compose paths and exported as a matrix of global coordinates and principal strains. This information is processed to generate graphs of path length (or distance along the path) in relation to maximum and minimum principal strains. The graphs of maximum and minimum principal strains along anterior path is presented in Figure 3.4, while the medial and lateral paths are presented in the Appendix A as Figure A.1 and Figure A.2 respectively. The Von Mises equivalent strain profile is presented in Figure 3.5 as a contour plot, sectioned to display the strain profile on both inner and outer surfaces.

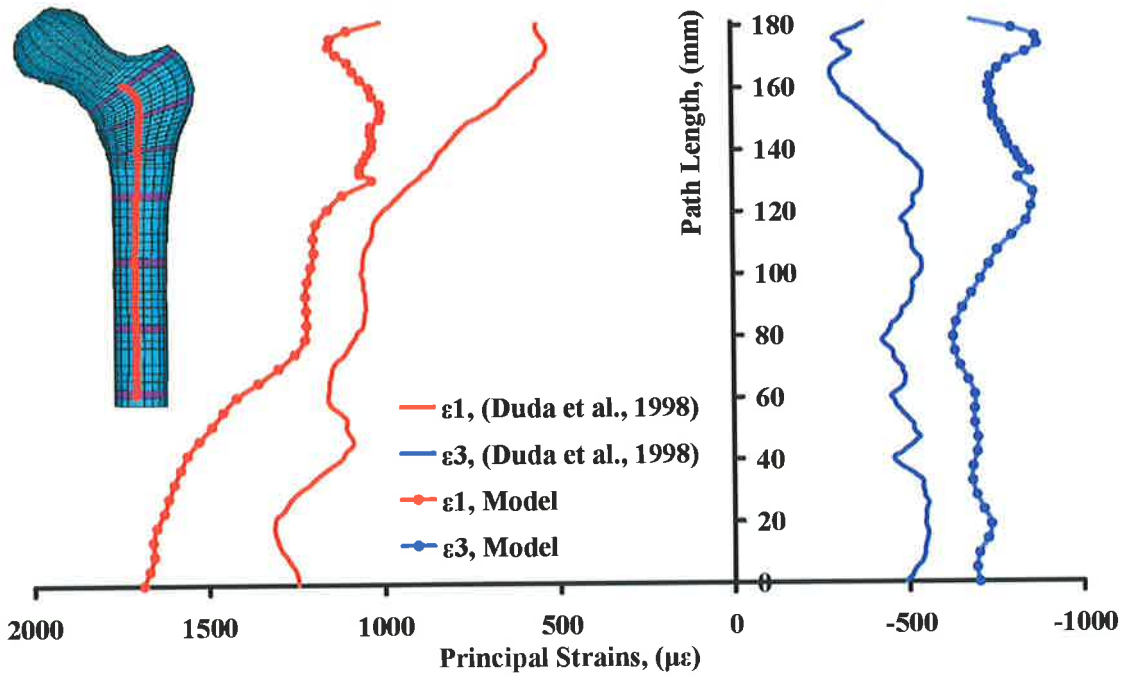


Figure 3.4: Comparison of model resultant principal strains along an anterior path with those obtained from Duda et al. (1998).

Comparison of model results with those from Duda et al. (1998) reveal a similarly in principal strain trends along the anterior, medial and lateral paths, although the results obtained form the model are consistently larger in magnitude than those of Duda et al. (1998).

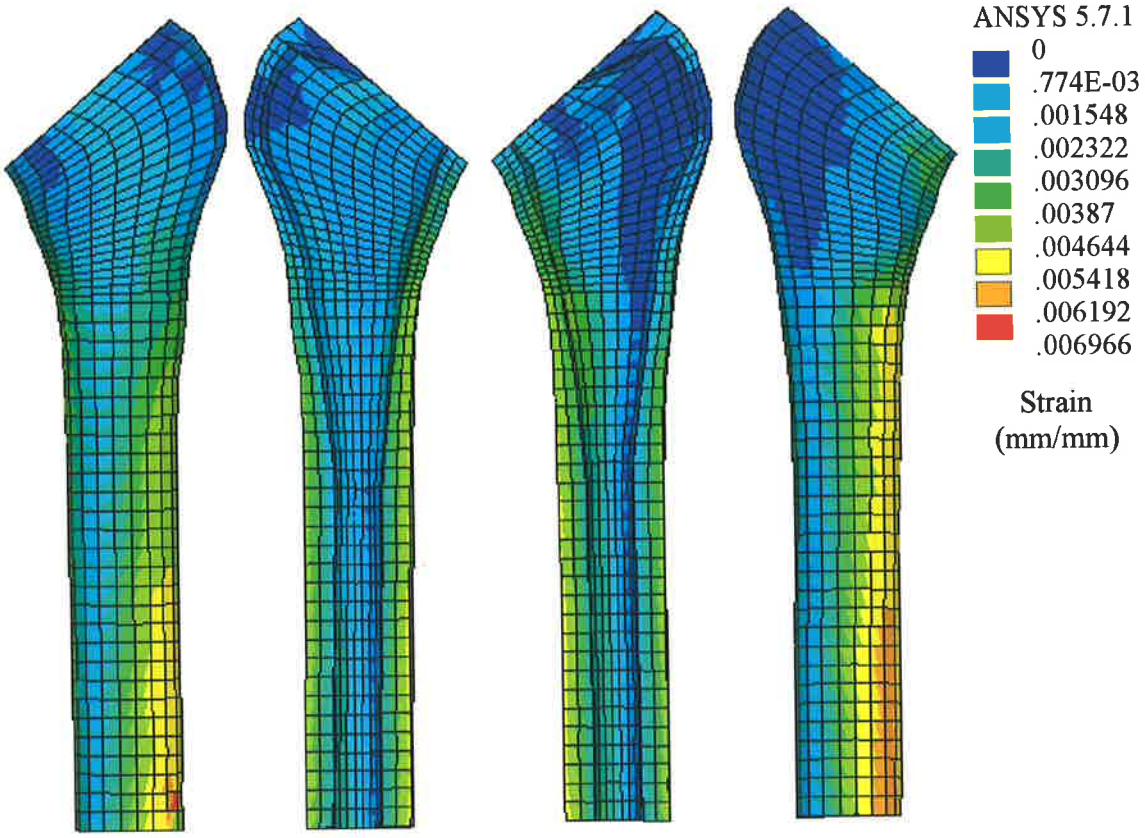


Figure 3.5: Contour plot of Von Mise's equivalent strain profile for the model, (ANSYS V5.7.1., 2002).

Two major differences exist between the current model and that developed by Duda et al. (1998). Duda et al. (1998) plotted results at the outermost surface of the model, while results from the current model are extracted half way through the cortical bone thickness. If all other model characteristics were constant, stresses and strains at the surface of the model should be higher than those in the middle of the cortical bone thickness, as they are further from the effective neutral axis.

One explanation for the large resultant magnitude in the developed model is the absence of reinforcing cancellous bone material. Duda et al. (1998) filled the interior void within the 'standardised femur' geometry with a material allocated a Young's Modulus of 1500 MPa. This

would reduce the levels of stress and strain within the cortical bone, and could account for the consistently higher results generated by the developed model. In addition, results obtained from the model were not recorded at identical locations to those of Duda et al. (1998), further impeding comparison.

Unfortunately it was not possible to replicate completely the protocol used by Duda et al. (1998). It was decided not to continue with the comparison of the developed model and the model created by Duda et al. (1998), which could have been achieved by filling the void within the 'standardised femur' with reinforcing cancellous bone structure. The developed model was evidently deficient in material property and geometry detail and considered too basic for further use within this research, and so, it was decided to focus efforts elsewhere.

3.5 Conclusion

This preliminary modelling investigation has provided valuable guidance for the generation of numerical models designed to simulate intact femoral response.

Although resultant trends produced by the model were similar to other published work, discrepancies in resultant magnitudes existed. Differences in significant model characteristics (such as location of displayed results and presence of reinforcing cancellous bone) made comparison problematical, with substantial modification required to allow more precise comparison. Unfortunately, other major shortcomings and incurable inadequacies of the developed model had surfaced during this work, requiring the development of a completely new model. Hence, resource limitations prohibited further development and alteration of the model.

The 'standardised femur' solid model is useful but has limitations. The two volumes defining cancellous and cortical bone are unnatural, and for the purpose of this research, do not provide an adequate distribution of material properties. Analysis of implant technology without adequate material property allocation would yield results irrelevant to the natural femoral

system. A model with realistic material property distribution is required for investigation of natural response to implant technology.

The smoothed geometry of the modified 'standardised femur' used in this initial model is oversimplified. It is believed that investigation of femoral response to implant technology requires a more realistic femoral geometry to provide relevant findings. The upper femoral regions of the 'standardised femur' define an almost constant thickness of material, with the internal geometry vastly more unrealistic than the external geometry. Although the 'standardised femur' solid model geometry has value within the research community, it is not adequate for this research.

Numerical models designed to investigate natural response require both realistic geometry and material properties. A model with more realistic geometry and distribution of material properties is required for this research. A model based on CT scans of a natural femur constructed using existing and available techniques would meet the specifications. This preliminary modelling of the intact femur has provided information beneficial to the development of another more advanced intact femur numerical model.

Chapter 4

UNDERSTANDING RESULTANT SENSITIVITY TO CHANGES IN MODEL CHARACTERISTICS

4.1 Introduction

Prior to investigating the optimisation of femoral implant characteristics, a suitable numerical model for the intact femoral system is required. This intact femoral system model will form the basis of the implanted femoral model. Accuracy of the intact femoral system model is paramount if solutions from the implant optimisation investigations are to be relevant.

Current numerical modelling techniques for simulating the femoral system vary considerably between researchers. Some of these modelling techniques generate results that possibly are an inaccurate representation of what occurs in the intact femoral system. This is often due to oversimplification.

Preliminary modelling in this research has indicated there are many requirements for accurate investigation of the natural femoral system, as well as deficiencies in popular modelling techniques. Model attributes such as material properties, loading and boundary condition regimes heavily influence solution accuracy.

With such variation of model characteristics throughout the research community, an understanding of the resultant influence these model parameters provide is required. Results

generated using simplified model input parameters should be interpreted while taking into consideration the assumptions made when performing the simplifications.

Generating a method for creating implanted femoral numerical models whose results can be correlated to the intact femoral system will allow other researchers to advance their studies.

4.2 Research Aim

The aim of this sensitivity analysis is to identify and quantify factors that influence stress shielding within the intact femoral system.

Once these factors have been determined, the relative stress shielding effect generated by each of these factors will be quantified. This will allow the major stress shielding influences to be identified and investigated to ascertain the required level of computational expense and model detail required to provide accurate model generated results.

The model for the intact system endeavours to be as state-of-the-art as possible, while achieving an efficient balance between solution accuracy and computational expense.

The result of this sensitivity analysis will be a numerical model that is used to investigate realistic femoral response to implant technology. This numerical model will exhibit a benchmark set of characteristics to ensure model generated results can be associated accurately to the intact femoral system.

4.3 Model Generation

Development of a numerical model for the intact femur was assisted by the acquisition of a freely available intact femoral model mesh with defined material property distribution.

4.3.1 Model Aquasition

Preliminary modelling indicated a need for realistic model geometry and material properties. The 'VAKHUM' (Virtual Animation of the Kinematics of the Human) project coordinated by Van Sint Jan (2002), provides for download of finite element models for both left and right femurs in different mesh densities. Increasing mesh density allows the capture of more morphological data such as material property distribution and geometry refinement. The left femur was chosen since muscular loading is published by Duda et al. (1998) for this bone.

Elements within this model are first-order, 8-noded, 8-sided, hexahedral 'bricks'. Within ANSYS, these elements are referred to as 'Solid45' elements. The mesh provided by the 'VAKHUM' project (Van Sint Jan, 2002), is high quality, easily passing element shape testing procedures. It is believed that no meaningful improvement could be made to this mesh whilst maintaining the same mesh density. This model mesh is displayed in Figure 4.1

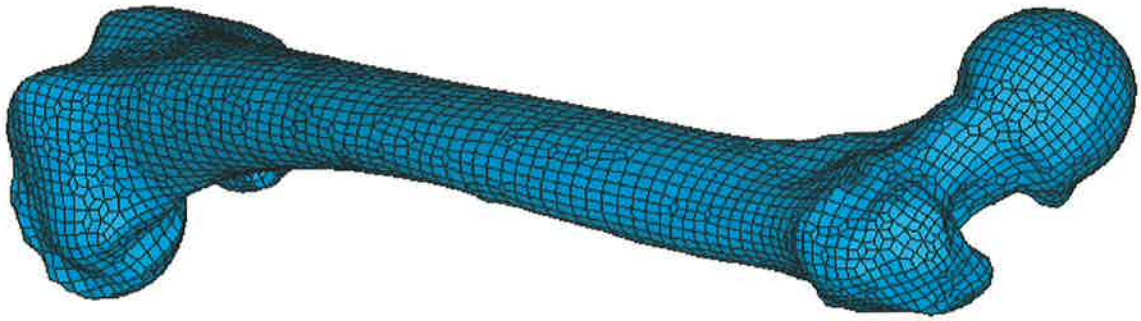


Figure 4.1: Left femur model mesh obtained from the 'VAKHUM' project (Van Sint Jan, 2002).

This numerical model of the left femur (Figure 4.1) with the fourth level of mesh refinement, having 18,863 elements and 21,563 nodes was obtained as a compromise between accuracy and model size. This model provides 215 individual linear isotropic material properties with constant Poisson's ratio of 0.3 and Young's Modulii ranging from 1.3GPa to 28.1GPa. A contour plot displaying the distribution of these material properties is provided in Figure 4.2.

As expected, bone stiffness increases from the centre of the femoral shaft towards the exterior surface.

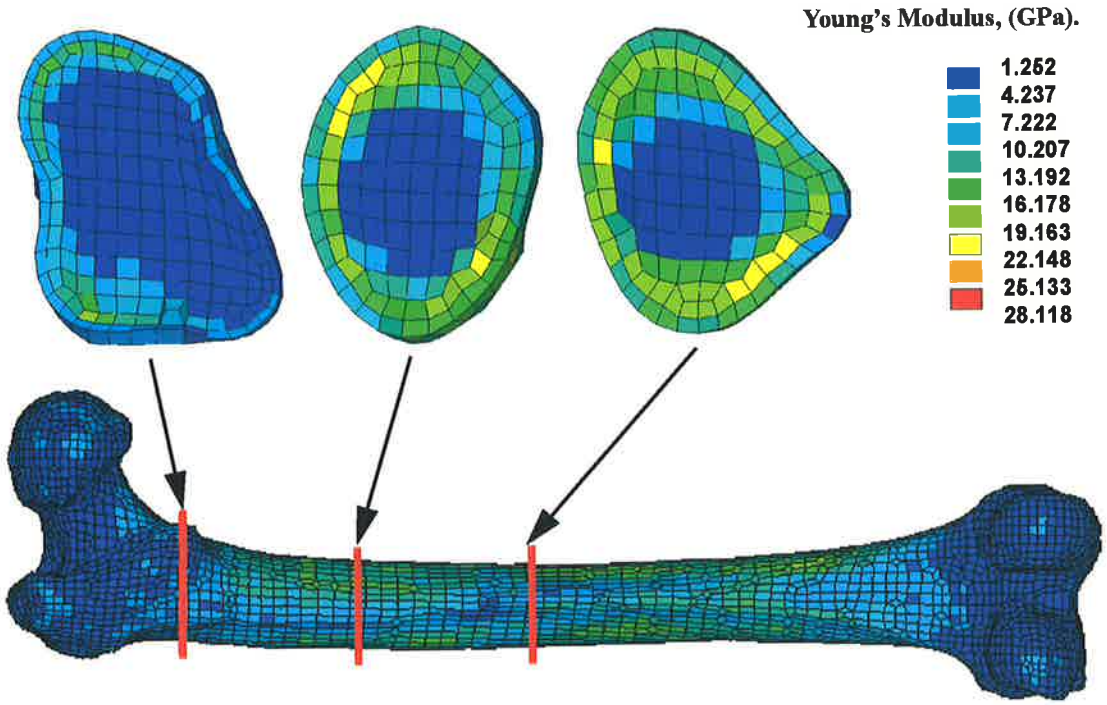


Figure 4.2: Contour plot of Young's Modulus distribution within the model.

4.3.2 Quantifying Resultant Trends

For the purpose of this investigation, results extracted from the model need to be relevant and easily correlated to bone remodelling. As strain energy density is often regarded as the quantity that drives the bone remodelling process, it is recorded as the quantity for evaluation.

The nodal Von Mise's equivalent strain energy density is output from the numerical model by manipulating the nodal Von Mise's equivalent strain and stress. This is simpler than manipulating either the stress or strain alone, as the Young's Modulus for adjacent elements sharing a node can differ.

Although contour plots are helpful in visualising the change in magnitude of a quantity when plotted on the geometry, graphing the change in magnitude along a path within the geometry often provides a clearer understanding of behaviour.

Bone material in the regions surrounding femoral implants is of primary concern when evaluating the performance of a femoral implant with respect to bone remodelling, and so this is where results are recorded for evaluation.

Paths are generated linking adjacent surface nodes on the anterior, posterior, lateral and medial surfaces of the upper femur. These paths commence at the upper regions of the femur and extend along the length of the femoral shaft further than where a femoral implant would reach. These paths are displayed in Figure 4.3. The Von Mise's equivalent strain energy density is plotted along the paths to allow evaluation of solution trends.

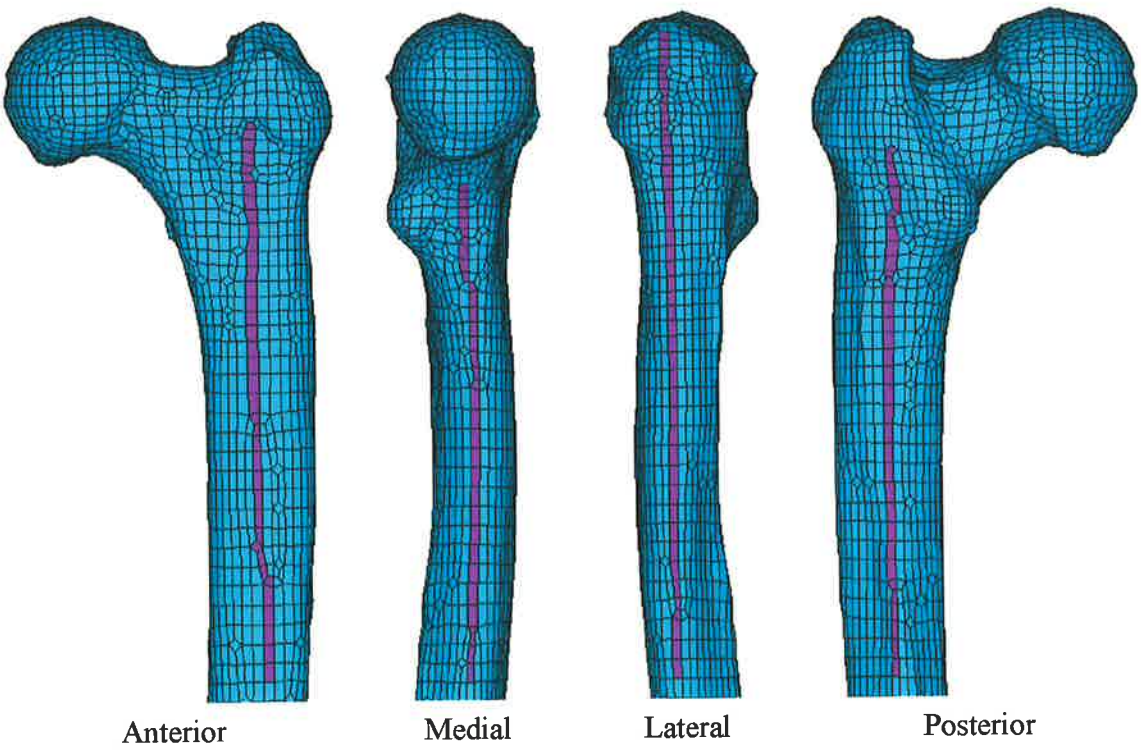


Figure 4.3: Paths (purple) along which results are recorded for graphical representation.

4.4 Choice of Loadstep

The detailed muscular loading data acquired from Duda et al. (1998) provides a four-step loading regime for the gait cycle. These four steps contain the instance of maximum muscle activity, the first and second peaks in ground reaction forces and the swing phase.

All of these phases of the gait cycle produce differing load distributions, and so a femoral implant optimised for each would yield different designs. Designing an optimal femoral implant should revolve around the maximum load condition, negating the possibility of designing an implant with dangerously low strength when subjected to a different load step.

This investigation intends to find the loading regime that generates the maximum Von Mise's equivalent strain energy density within the bone volumes of interest. If the THA stem is designed with a defined maximum loading regime, then the likelihood of over-engineering is reduced, meaning other loading regimes that do not stress the femur as much are also not burdened with an overly engineered THA stem. Unfortunately the design of the THA stem remains constant while the loading is irregular.

Selection of the load regime providing maximum femoral response is achieved by averaging the Von Mise's equivalent strain energy density along the previously defined paths for each loading regime, and selecting the loading regime that generates maximum model response.

Muscular loading is applied to the model as a series of nodal point loads. These loads are sourced from Duda et al. (1998) and provide individual muscular loading as directional components of the model Cartesian coordinate system. This model Cartesian coordinate system is constructed using alignment data provided by Duda et al. (1998). All knee joint ligament and contact data was neglected as it was assumed not to influence the upper femoral regions of interest (Joshi et al., 2000).

The location coordinates of load application is provided by Duda et al. (1998) for the 'Standardised Femur', however the dimensions of the model provided by the 'VAKHUM' project (Van Sint Jan, 2002), are different. Consequently the node closest to the centroid of the muscular attachment area was manually established with the aid of anatomical textbooks. The muscular loading data can be found in Table 4.1.

The model is restrained at the distal end of the femur. This is achieved by fixing all degrees of freedom for nodes located on the models exterior surface, in the vicinity of the femoral bearing surface at the knee joint. Material properties remain unchanged from those provided.

The four loading regimes were treated as individual linear elastic static solutions, each requiring minimal computational effort to solve. The resultant average Von Mise's equivalent strain energy density along the anterior, posterior, medial and lateral lines as previously defined are presented in Table 4.2.

Table 4.2 shows the maximum Von Mise's equivalent strain energy density exists within the medial path for the second peak in ground force gait phase (45% gait cycle). Interestingly, the Von Mise's equivalent strain energy density result trends are similar within the upper femoral regions for the fist three gait phases, with magnitude being the major difference. The final swing phase of the loading regime (70% gait cycle) yields results of minute magnitude, as would be expected when the foot is swinging in the air. The Von Mise's equivalent strain energy density along the four paths for the 45% gait cycle load regime is plotted in Figure 4.4. Plots for the 10%, 30%, and 70% gait cycle load regimes can be found in Figure A.3, Figure A.4, and Figure A.5 respectively, located in the Appendix A.

Figure 4.4 shows a 'spike' in Von Mise's equivalent strain energy density on the lateral path. This is the result of a muscular load applied to the node, which is part of the lateral path. This 'spike' is a localised stress concentration point that is difficult to exclude without distributing muscular loading (covered later).

Table 4.1: Joint reaction and muscular loading data (Duda et al., 1998).

Muscular Group	Node Number	Force at 10% Gait Cycle [N]			Force at 30% Gait Cycle [N]			Force at 45% Gait Cycle [N]			Force at 70% Gait Cycle [N]		
		X	Y	Z	X	Y	Z	X	Y	Z	X	Y	Z
Joint Contact Hip	16582	-510.63	665.76	-1131.89	-399.59	812.50	-1435.34	-466.34	962.62	-1911.22	-68.12	4.94	-47.79
Gluteus Maximus 1	17191	71.13	-71.72	75.19	50.18	-87.92	90.85	35.10	-87.87	90.95			
Gluteus Maximus 2	18285	27.33	-58.78	75.97	10.05	-69.16	85.76	0.08	-57.73	70.32	0.20	-0.45	0.55
Gluteus Maximus 3	17719	36.06	-12.13	-27.76									
Gluteus Medius 1, 2, 3	17059	161.10	-118.59	149.10	128.07	-164.71	201.36	111.23	-179.68	221.40	3.57	-4.89	5.53
Gluteus Minimus 1, 2, 3	16809	136.50	-92.37	36.25	152.51	-177.49	78.50	186.22	-193.69	92.98	22.29	28.45	7.97
Tensor Fasciae Latae	17265	3.23	-51.09	-18.95	35.26	-20.26	-26.34	51.42	-40.70	-40.04	6.43	-3.00	-5.58
Piriformis	16536	22.71	-47.98	42.95	15.17	-77.90	68.03	5.35	-77.90	67.03	2.89	-6.42	5.44
Obturator Externus	17609										0.55	-0.41	0.07
Quadratus Femoris	17523	20.34	-22.79	32.46									
Obturator Internus, Gemellus Superior & Inferior	16872	11.96	-18.98	20.66	12.43	-36.77	39.19	7.07	-35.18	37.20	2.15	-3.92	4.14
Pectineus	18436							1.30	-1.01	1.12	2.38	-1.06	1.32
Vastus Medialis	19131	82.90	-6.10	-259.22				2.93	0.18	-8.09			
Vastus Intermedius	19022							9.13	5.01	-62.06			
Vastus Lateralis	18912							69.58	-25.73	-215.72			
Gastrocnemius Lateralis	20302	-22.75	5.96	-52.93	-126.98	21.72	-159.16	-292.75	-37.74	-247.83	-19.04	-3.33	-4.72
Gastrocnemius Medialis	20345				-6.77	2.30	-8.42	-5.71	0.04	-4.77			
Biceps Femoris, Caput Breve	19085	-0.10	9.17	-48.81	-4.00	10.97	-60.16	-15.09	11.31	-90.02	-0.64	0.17	-2.21
Adductor Magnus Caudal	20326	6.44	-7.45	61.20									
Adductor Magnus Cranial	18643	30.22	-49.77	63.83									
Adductor Minimus	19223	9.53	-20.47	51.26				1.86	-1.90	2.81	11.45	-7.62	13.25
Adductor Longus	18963										0.40	-0.29	0.26
Adductor Brevis 1	18409												
Adductor Brevis 2	18577										0.37	-0.28	0.31
Psoas Major, Iliacus	18088				51.47	-24.37	44.32	115.24	-62.89	114.51	32.41	-7.41	20.43

The 45% gait phase loading regime (otherwise referred to as toe-off) is chosen as the basis for future modelling, as it provides the greatest model response in locations of relevance to this

research. Design of an implant for this loading regime will negate the possibility of implant failure due to overload conditions. Investigation of stair climbing that loads the implant and cement under torsion and bending moments would be interesting, however, the quantity of published results available for comparison justify use of the 45% gait cycle. Model response to other loading regimes is not required in future investigations.

Table 4.2: Resultant avererage Von Mise's Equivalent Strain Energy Density along paths of interest for load regimes.

Average Von Mise's Equivalent Strain Energy Density Along Path, (KJ/m³)				
Path	**10% Gait Cycle Load Regime**	**30% Gait Cycle Load Regime**	**45% Gait Cycle Load Regime**	**70% Gait Cycle Load Regime**
Lateral	31.98	45.21	68.75	0.07
Medial	65.96	86.25	148.12	0.17
Posterior	30.56	38.28	60.03	0.05
Anterior	27.95	36.59	55.62	0.03

4.5 Refinement of Muscular Inclusion

Muscular loading data sourced from Duda et al. (1998), is comprehensive. Numerous muscular groups provided are remote from the femoral regions of interest. Other muscular groups provide very small loading magnitudes relative to others. It is possible that these relatively weak and remote muscular groups contribute little to the loading of the upper femoral regions of interest, and neglecting these muscular groups may simplify the model significantly.

The numerical model used previously for the selection of gait cycle load regime is used, with all model characteristics unchanged. All muscular groups provided in the 45% gait cycle load regime are graded in order of magnitude of summed directional load components. This grading allows for the systematic elimination of muscular groups from the model in order of minimum summed directional force magnitude. These muscular groups are neglected from the model one at a time. The range of muscular inclusion for alternate solutions is presented in Table 4.3.

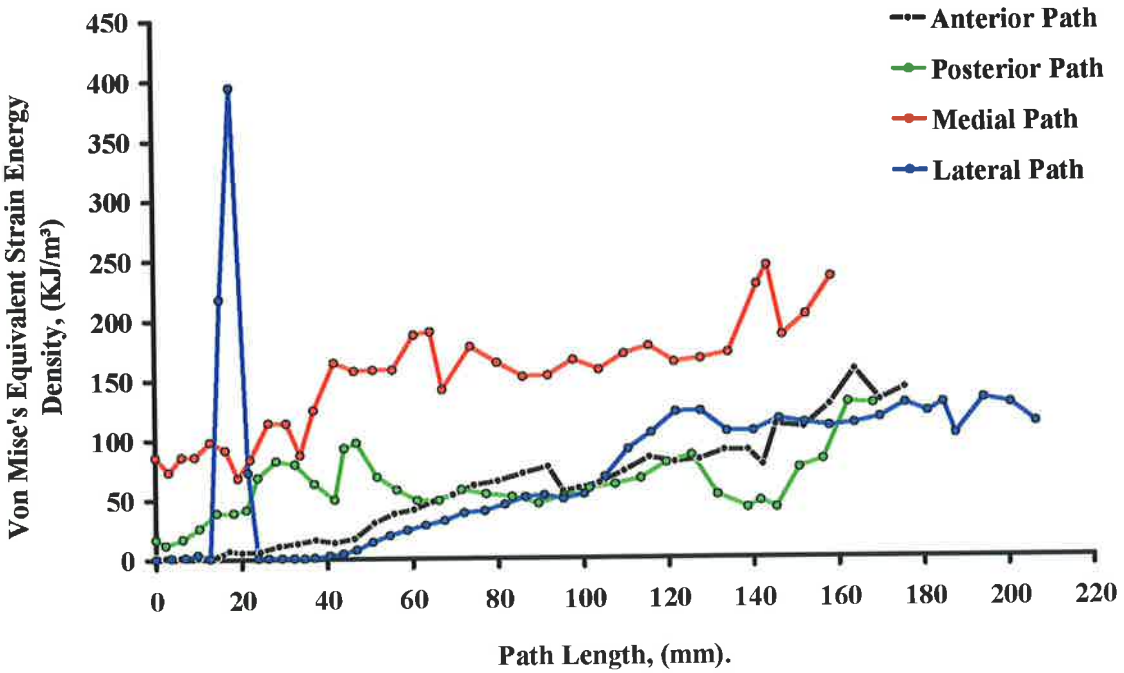


Figure 4.4: Von Mise's Equivalent Strain Energy Density along paths of interest for 45 % gait cycle load regime. Spike in Von Mise's Equivalent Strain Energy Density on the lateral path is attributed to muscular loading on that particular node.

Results for the numerical simulations are recorded as a percentage change in average Von Mise's equivalent strain energy density along the previously defined paths from complete muscular group inclusion. These results are provided in Table 4.4.

Although some muscular groups have significant force magnitude there is little resultant influence along the paths of interest. The initial 17 solutions systematically analyse the model by eliminating one muscular group at a time, demonstrating the influence of singular muscular groups. The final solution includes all muscular groups that have more than a 1% change in average Von Mise's equivalent strain energy density from complete muscular group inclusion along any path.

Table 4.3: Muscular group inclusion within specific solutions.

Muscular Group	Total Force, (N)	Solution Number																	
		1	2	3	4	5	6	7	8	9	10	11	12	13	14	15	16	17	18
Joint Contact Hip	2190	x	x	x	x	x	x	x	x	x	x	x	x	x	x	x	x	x	x
Gastrocnemius Lateralis	385	x	x	x	x	x	x	x	x	x	x	x	x	x	x	x	x		
Gluteus Medius 1, 2, 3	306	x	x	x	x	x	x	x	x	x	x	x	x	x	x	x			x
Gluteus Minimus 1, 2, 3	284	x	x	x	x	x	x	x	x	x	x	x	x	x	x				x
Vastus Lateralis	228	x	x	x	x	x	x	x	x	x	x	x	x	x					
Psoas Major, Iliacus	174	x	x	x	x	x	x	x	x	x	x	x	x						x
Gluteus Maximus 1	131	x	x	x	x	x	x	x	x	x	x	x							x
Piriformis	103	x	x	x	x	x	x	x	x	x	x								x
Biceps Femoris, Caput Breve	92	x	x	x	x	x	x	x	x	x									
Gluteus Maximus 2	91	x	x	x	x	x	x	x	x										x
Tensor Fasciae Latae	77	x	x	x	x	x	x	x											x
Vastus Intermedius	63	x	x	x	x	x	x												
Obturator Internus, Gemellus Superior & Inferior	52	x	x	x	x	x													x
Vastus Medialis	9	x	x	x	x														
Gastrocnemius Medialis	7	x	x	x															
Adductor Longus	4	x	x																
Pectineus	2	x																	

x denotes inclusion within the solution.

Table 4.4: Solution change from complete muscular loading regime generated by reduced muscular inclusions.

Solution Number	Average Von Mise's Equivalent Strain Energy Density Along Path, (KJ/m³)				Change In Average Von Mise's Equivalent Strain Energy Density Along Path From Complete Muscular Inclusion Load Regime			
	Lateral Path	Medial Path	Posterior Path	Anterior Path	Lateral Path	Medial Path	Posterior Path	Anterior Path
1	68.7	148.1	60.0	55.6	0.0%	0.0%	0.0%	0.0%
2	68.8	148.3	60.1	55.7	0.1%	0.1%	0.1%	0.1%
3	68.8	148.3	60.1	55.7	0.1%	0.1%	0.1%	0.1%
4	68.8	148.3	60.1	55.7	0.1%	0.1%	0.1%	0.1%
5	68.8	148.3	60.1	55.7	0.1%	0.1%	0.1%	0.1%
6	68.7	150.7	64.0	59.5	-0.1%	1.7%	6.7%	7.0%
7	68.7	150.6	64.0	59.7	0.0%	1.7%	6.6%	7.3%
8	72.7	161.1	69.3	62.4	5.8%	8.7%	15.4%	12.1%
9	71.9	162.2	71.6	65.4	4.7%	9.5%	19.2%	17.7%
10	72.0	162.2	71.6	65.5	4.7%	9.5%	19.3%	17.7%
11	69.8	164.3	84.9	78.2	1.5%	10.9%	41.5%	40.6%
12	69.2	170.0	98.5	90.5	0.7%	14.7%	64.1%	62.7%
13	78.8	195.4	108.3	98.4	14.6%	31.9%	80.4%	76.9%
14	79.0	194.9	107.7	96.8	14.9%	31.5%	79.3%	74.1%
15	91.7	242.5	161.4	138.7	33.4%	63.7%	168.9%	149.4%
16	77.5	264.3	216.4	187.5	12.7%	78.4%	260.5%	237.1%
17	77.5	264.3	216.4	187.5	12.7%	78.4%	260.5%	237.1%
18	69.0	147.8	59.7	54.8	0.4%	-0.2%	-0.5%	-1.5%

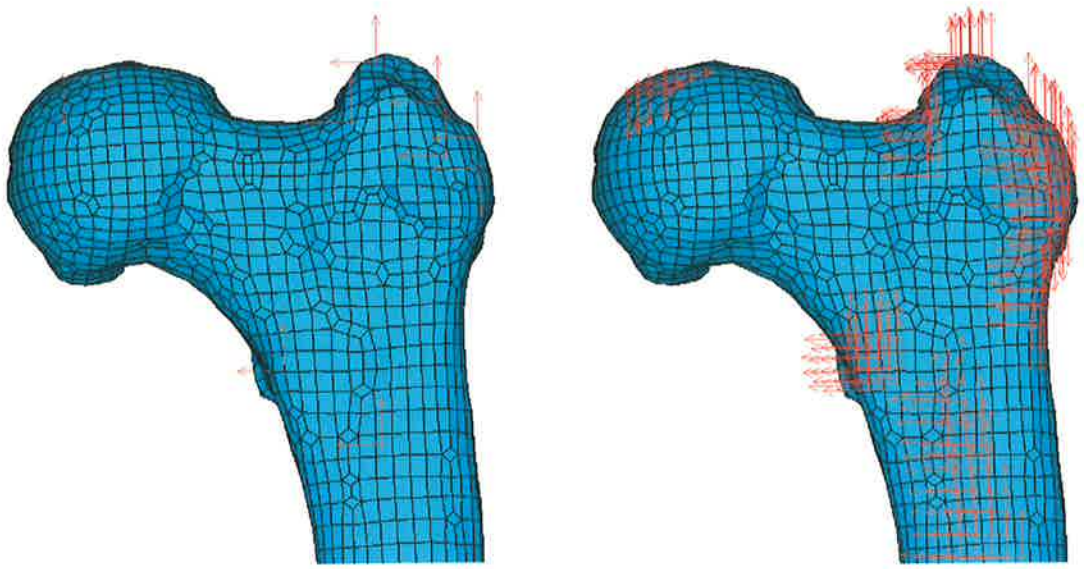
This muscular group inclusion investigation ascertains that using only half of the muscular groups provided by Duda et al. (1998), generates a solution within the femoral regions of interest accurate to within a few percent of total muscular group inclusion. This is a valuable finding, as model simplification can be made.

4.6 Anatomically Accurate Distribuion of Muscular Load

Previous models have applied muscular loading as singular point loading. Although this transfers the correct load magnitude to the model, regions of excessive and unnatural bone response exist. Muscular groups attach to bone over specific areas. It is suggested that distribution of loading over natural muscular attachment areas would produce a more realistic and advanced model. The same load magnitude would be applied to the model, however the regions of excessive and unnatural bone response associated with point loading would be eliminated.

The numerical model for the 45% gait cycle load regime is used, employing the newly found refined muscular inclusion. All other model characteristics are unchanged. An anatomical textbook (Cunningham and Romanes, 1986) was used to select nodes on the exterior surface of the model that locate within the muscular attachment areas. The directional force components for each muscular load are divided by the number of nodes that formulate the attachment area, effectively producing an evenly distributed load. Although dissimilar node spacing means muscular loading is not evenly distributed, it is not known if natural muscular attachment is either. Basic dispersion of muscular loading is achieved with this method. A comparison between point and dispersed loading can be seen in Figure 4.5.

The Von Mise's equivalent strain energy density profiles along the medial and lateral defined paths are similar for both load attachment methods. This comparison can be seen in Figure 4.6. The average Von Mise's equivalent strain energy density along the lateral path for distributed loading differs from that of point loading mainly due to the influence of a single muscular group



Point Loading Distributed Loading

Figure 4.5: Muscular loading applied as point loading and distributed loading.

located on the path itself. Distributed loading eliminates the unnatural region of intense loading, previously described as a 'spike'.

The femoral bending response to loading is only slightly different for the two load attachment methods along the medial and lateral paths, however femoral bending response is significantly increased along the anterior and posterior paths. This can be seen in Figure 4.7.

As the distributed muscular load attachment regime has been developed, it makes sense to employ its use within future models. It is more natural and advanced, and use of this loading regime will provide more accurate results.

4.7 Knee Restraint Boundary Condition

The femoral restraint condition allows scope for possible reduction in computational effort without compromising solution accuracy within the femoral regions of interest. It is suggested

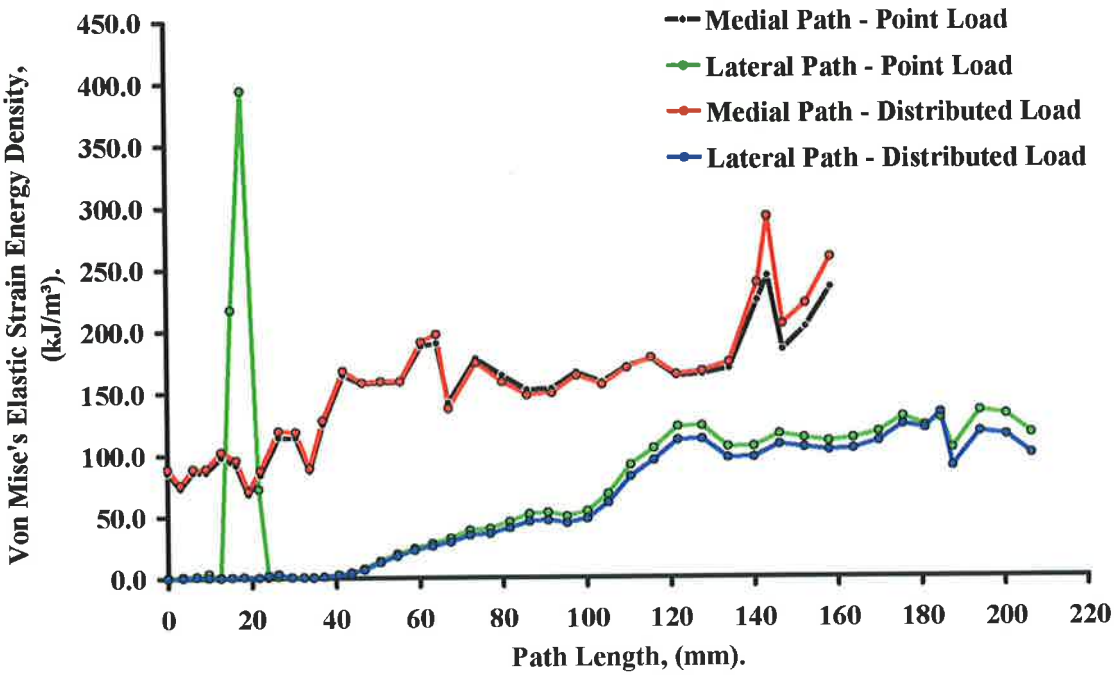


Figure 4.6: Comparison between point and distributed muscular loading for medial and lateral paths. Distributed loading eliminates the 'spike' in results generated with point loading on the lateral path.

that reduction in femoral length would reduce computational effort; however the magnitude of femoral length reduction without compromising the results is uncertain.

Five femoral lengths are investigated. The model used in prior investigations (45% gait cycle with reduced muscular inclusion and distributed loading) is restrained at all nodes near the distal end. Other restraint conditions have been allocated, allowing elimination of some elements from the model. Figure 4.8 shows the location of restraint conditions (labelled 1 to 5) used in this analysis. Purple areas indicate the region of interest, and include all nodes that compose the anterior, posterior, medial and lateral paths previously used for recording results. The red areas indicate restraint locations. In these restraint locations elements have all associated nodes restrained an all degrees of freedom. When any of these restraint regions are used other than the complete length condition, the elements distal to the specific restraint location are removed. This reduces computational intensity.

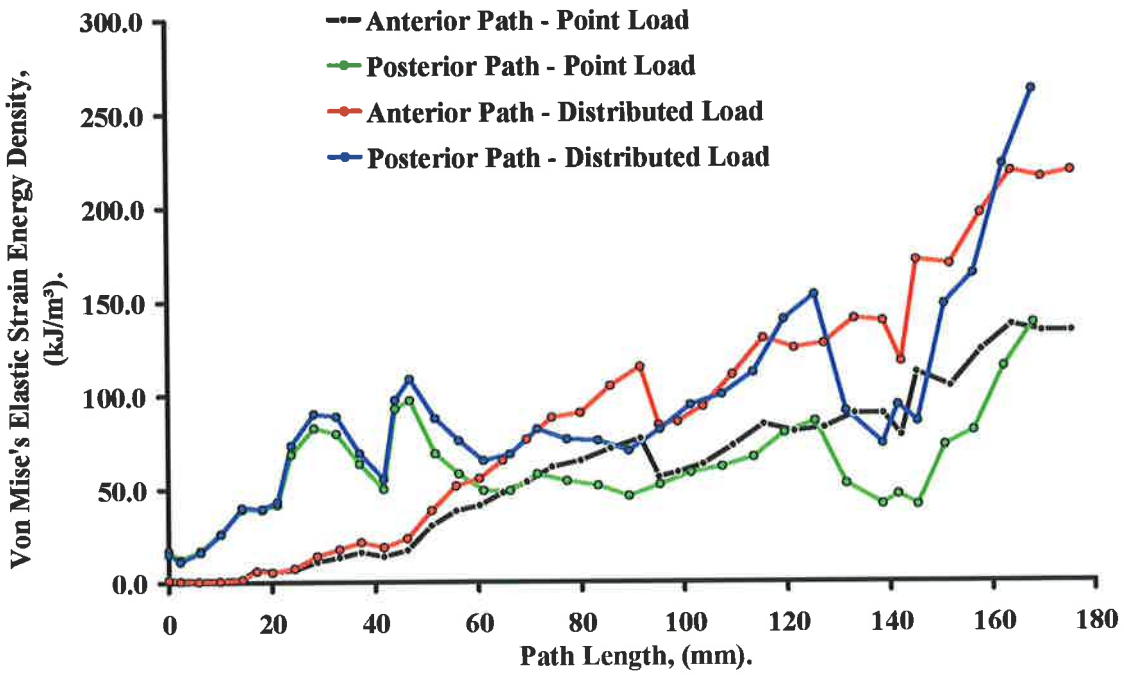


Figure 4.7: Comparison between point and distributed muscular loading for anterior and posterior paths.

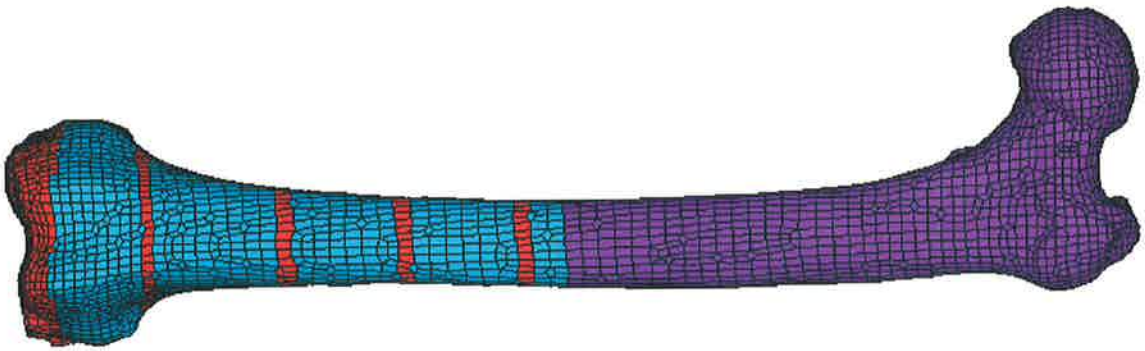


Figure 4.8: Reduced length femoral model. Purple indicated regions of interest and red indicates restraint location.

Results obtained from this investigation are presented in Table 4.5. It can be seen that extremely similar results within the femoral regions of interest are obtained using either the fully fixed distal end of complete femur or fully fixing base of a reduced length femur. The final boundary

condition tested (5) provided a 48% reduction in the number of elements within the model, however the average Von Mise's equivalent strain energy density differed by less than 1% to the complete femoral length condition along all paths. Graphs showing actual Von Mise's equivalent strain energy densities on paths are not included since the discrepancies are too small to visualise.

Table 4.5: Restraint condition details and results.

Boundary Conditon	% Reduction in Elements from Complete Model	Average Von Misses Equivalent Strain Energy Density Along Path, (KJ/m³).			
		Lateral Path	Medial Path	Posterior Path	Anterior Path
1	-	50.08	152.66	88.81	82.82
2	27.90%	50.08	152.66	88.81	82.82
3	37.43%	50.08	152.66	88.81	82.82
4	42.85%	50.08	152.67	88.81	82.82
5	47.62%	50.16	151.75	88.00	82.33

The minute discrepancy between results obtained from the different restraint regimes stems from the proximity of the restraint location to the paths where results are recorded. Elements located close to the restraint location experience increased loading due to reaction forces at the restraint location. As the restraint condition is located two elements away from the femoral region of interest, much of the restraint reaction force is dissipated. Locating the restraint condition closer has a graeter influence.

Although the Von Mise's equivalent strain energy density profiles along the four paths showed near-identical results for the complete and shortened femur models, strain along the length of the femur was examined to eliminate the possibility of any change in the component magnitudes within Von Mise's calculations. This investigation yielded similar trends to the Von Mise's equivalent strain energy density results.

This investigation shows that if accurate results are only required for the upper femoral regions, then increased modelling efficiency can be achieved by restraining the model a short distance

from the regions of interest. This major reduction in model size will have a great impact on solution time when used in iterative optimisation analysis.

4.8 Model Verification

Verification of model solution convergence is achieved through the comparison of models with increasing element edge shape function polynomial order, with the original first-order elements substituted for second and third-order elements.

Throughout this investigation, the number and location of elements within the model was constant, allowing identical nodal loading, restraint and recording of results along the paths of interest.

Initially, results were recorded along the four paths of interest as previously discussed for the reduced femoral length model with refined and dispersed muscular loading. This model used first-order 8-noded solid ANSYS 'solid45' brick elements.

The second level of model refinement was achieved by replacing the first-order 8-noded elements with second-order 20-noded solid ANSYS 'solid95' brick elements. These elements have mid-sided nodes, and provide a more accurate quadratic representation of quantities along the element boundary.

The third level of model refinement was achieved by replacing the second-order 20-noded solid ANSYS 'solid95' brick elements with ANSYS 'solid147' 3D structural brick P-Type elements. This analysis used the p-method rather than the h-method used in all previous models. The p-method obtains results to a user specified degree of accuracy by assigning high order polynomial levels to the finite element shape functions in order to approximate the real solution.

For this model, the p-level was automatically altered to provide results that converge to within 1% of the global strain energy. All elements including nodes with an applied load or restraint were neglected from the p-type convergence computations to discount the influence of singularities. Convergence was achieved with the majority of elements assigned second-order polynomial level, with the others third-order polynomial level.

Results were extracted from each model along the paths of interest as previously discussed; however resultant nodal values were averaged within the corresponding element. This was a requirement for the extraction of results generated from a p-type analysis.

A Preconditioned Conjugate Gradient (PCG) Solver was used for all models. This indirect iterative solver generates relatively fast solutions accurate to convergence specification supplied by the user, and is suited to large models with solid elements. A preconditioner to the global assembled matrix is created by the solver, which is similar in size to the stiffness matrix, and is stored in memory with the non-zero part of the stiffness matrix. The solver requires a lower disk space but higher memory than other solvers. The convergence criterion for the solver was set to 1×10^{-8} for all solutions.

Solutions for this convergence analysis are displayed in Table 4.6, and displayed for the posterior path in Figure 4.9.

Table 4.6: Comparison between average Von Mise's Equivalent Strain Energy Density along paths for given element types.

Number of Nodes	Number of Elements	Element Type	Element Order	Analysis Type	Average Von Mise's Equvalent Strain Energy Density along Path, (kJ/m³).			
					Lateral Path	Medial Path	Posterior Path	Anterior Path
11,390	9,881	SOLID45	1	H-type	49.402	148.252	95.011	92.882
43,947	9,881	SOLID95	2	H-type	50.883	151.242	95.273	87.493
43,947	9,881	SOLID147	Variable	P-type	48.107	146.723	94.793	86.943

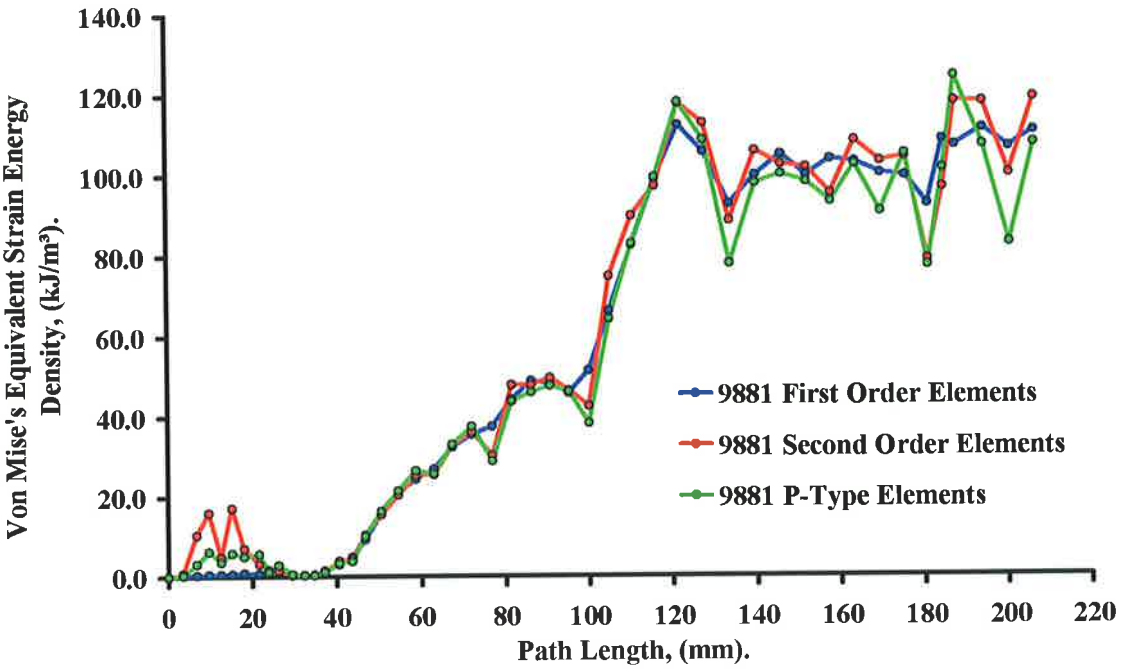


Figure 4.9: Comparison between average Von Mise's Equivalent Strain Energy Density along the posterior path for given element types.

Good agreement between results obtained using different levels of mesh refinement is achieved. This suggests that the model mesh density is sufficient using linear elements to generate an average Von Mise's equivalent strain energy density along the paths to within 7% (along the anterior path, 3% along other paths) of that using p-type elements that are converged to within 1% of the global strain energy. Therefore results obtained using the linear elements are sufficiently accurate relative to other model input data to be valid. Increasing the number of linear elements will increase accuracy further.

4.9 Conclusion

This investigation into the influence of specific model details has provided understanding of the required model characteristics to generate results efficiently and accurately.

This sensitivity analysis has suggested that for accurate results within the femoral regions of interest, a half length model is adequate. This model is restrained at the base, and has distributed refined muscular loading for the 45% gait phase. This provides the maximum femoral loading condition for the gait cycle, which is representitive of the 'toe-off' phase. The model response to this loading is displayed in Figure 4.10 and Figure 4.11.

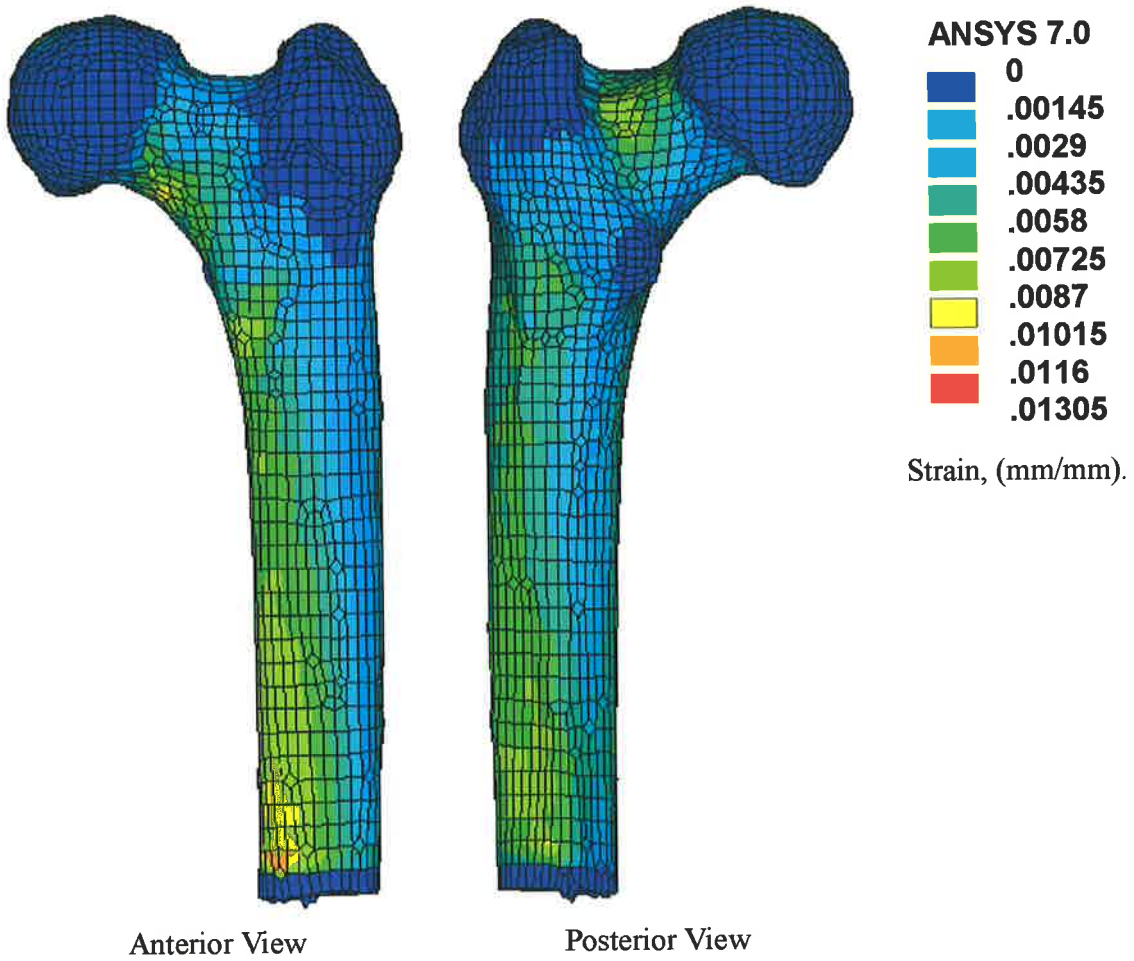


Figure 4.10: Von Mise's equivalent strain solution contour plot for the final model.

Although this model used in the sensitivity analysis has provided valuable information about model requirements, it is not suitable for use in implant technology investigation. This unsuitability for future model development is due to a congenital deformity referred to as a

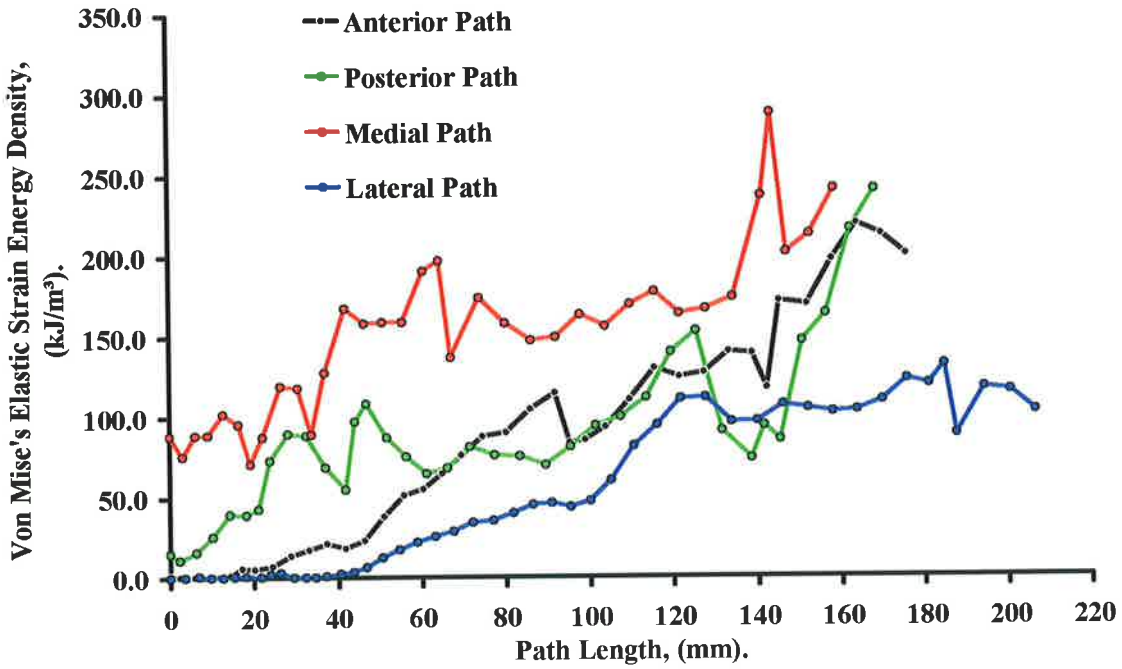


Figure 4.11: Von Mise's Equivalent Strain Energy Density for the final model.

'varus' femoral neck, discovered during a conversation with Dr Mellick Chehade, an Orthopaedic Surgeon (Department of Orthopaedics and Trauma, Royal Adelaide Hospital). A 'varus' femoral neck implies that the femoral head is located in a more distal position than expected for a given femur.

This deformity has implications when selecting and positioning femoral implants. Investigating femoral response to implant technology using this deformed model is interesting; however the findings are relevant only to those interested in 'varus' femoral shafts. Investigating implant technology using femoral geometry with more natural specifications is more valuable at the current time.

It has been decided that a new model should be developed from CT scans, based on an appropriate cadaveric femoral specimen. Using a real femoral specimen also allows actual THA stem implantation and additional CT scanning to reveal exact implant and cement locations,

assisting in model generation. Model characteristics discovered in this sensitivity analysis will be used in future models.

Chapter 5

GENERATION OF AN IMPLANTED FEMORAL MODEL USING ADVANCED MODELLING TECHNIQUES

5.1 Research Aim

This investigation aims to numerically identify short-term (immediate application of load post implantation) post-operative femoral response to two commercially available cemented THA stems with different surface finishes and corresponding modes of fixation under a previously defined realistic loading scenario. This will allow identification of the implant characteristics that are likely to provide superior service life.

The implanted femoral model generated within this investigation with most favourable stress shielding characteristics will form the basis for further optimisation techniques aspiring to further increase implant service life in the following chapter.

5.2 Introduction

Within this research, advanced numerical techniques are applied to investigate differences in load transmission and immediate post-operative stress shielding caused by two popular cemented THA stems that employ both dissimilar surface finishes and design philosophies in order to achieve stability. As much conjecture surrounds the choice of superior stem design in cemented THA, direct comparison of the level of stress shielding generated by the respective THA stems scientifically indicates superior characteristics.

The 'CTP Hip Prosthesis', pictured in Figure 5.1 is marketed by Zimmer, Inc. Warsaw, Indiana, USA, and was released in 1990. The manufacturers suggested retail price for the femoral component excluding the femoral head is $2,315USD (Trick 2001). This THA stem is of universal design, forged from Cobalt-Chrome (CoCr) material, and has a collarless double-tapered geometry. The implant surface finish is highly polished, endeavouring to prevent bonding with cement and allow subsidence with minimal friction, generating stability through a wedging motion. The tapering of this THA stem intends to impart compressive stresses within the cement. This implant has the benefit of simple extraction if revision surgery is necessary. The CPT THA stem geometry will subsequently be referred to as stem 'A' within this research.

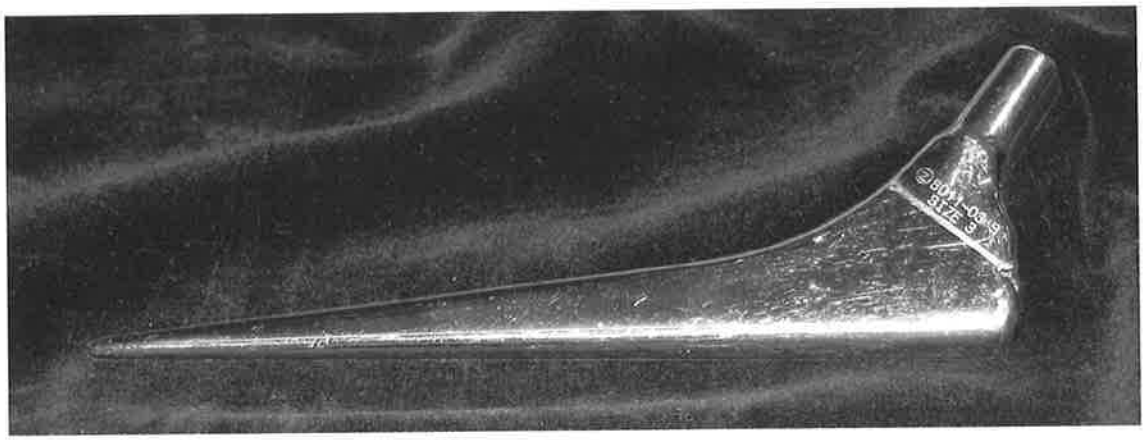


Figure 5.1: The CPT THA stem, subsequently referred to as stem 'A', has a double-tapered geometry with a highly polished surface finish. The pictured CPT stem is a retrieved specimen with scratches and is no longer highly polished

The 'Spectron' THA system, with stem component pictured in Figure 5.2 is marketed by Smith & Nephew, Inc. Memphis, Tennessee, USA, and was initially released in 1983, and later revised in 1989. The manufacturers suggested retail price for the femoral component including a forged CoCr femoral head is $3,267USD (Trick 2001). The stem is forged from CoCr material and has a circulotrapezoidal neck, designed to provide increased range of motion compared to a circular neck of the same strength (Smith & Nephew 2003). The collared stem has grooves on both Anterior-Posterior (AP) stem surfaces that increase rotational stability without increasing

cement stresses (Smith & Nephew 2003). The stem surface finish is matt with increased roughness in proximal regions generated by grit blasting. These surface textures promote bonding with the cement to achieve stability. The Spectron THA stem geometry will subsequently be referred to as stem 'B' within this research.

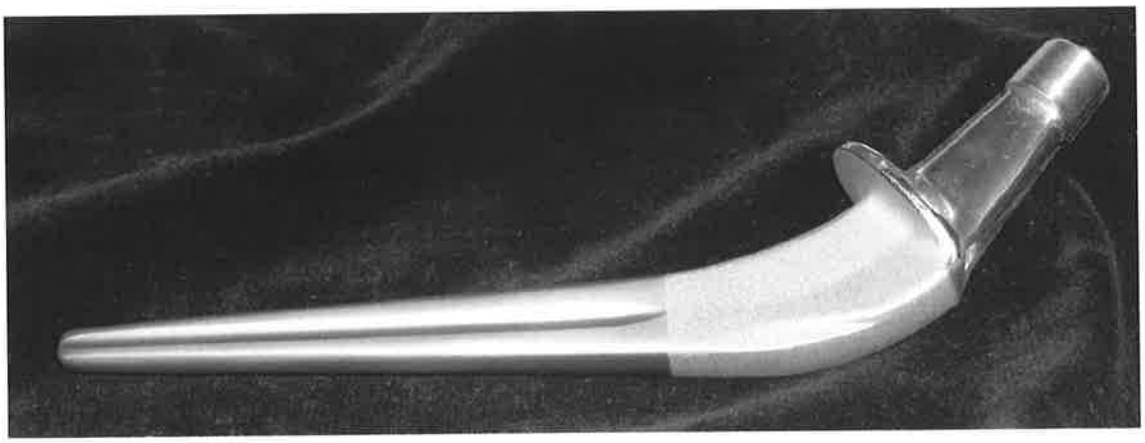


Figure 5.2: The Spectron THA stem, subsequently referred to as stem 'B', has a collared stem geometry with grooves and a grit blasted surface finish.

For this study numerical models are generated for both the intact and implanted femora. The numerical models constructed within this investigation are developed using cadaveric femora and CT scan technology, and implanted models are developed for the same femora after being professionally implanted. Model characteristics such as loading and restraint mechanisms meet or exceed the requirements for accurate modelling suggested within Chapter 4, and selected cadaveric femora have common geometry. These model characteristics overcome all limitations uncovered with the previously constructed models, also allowing further refinement of material property allocation and mesh density.

Furthermore, as numerical models of the implanted femur are generated from CT scans taken after a real THA stem implantation performed by an experienced orthopaedic surgeon, implant positioning and alignment is therefore accurate and transferred to the finite element model

through the CT scanning process. Participation of a skilled and internationally respected orthopaedic surgeon within this stage of the modelling process provides confidence in obtaining a model representative of a surgically implanted femoral system.

Conversion from CT scan data to finite element model information is mostly achieved using a program developed by Keyak et al. (1990). This program interprets the greyscale values of the CT data and calculates material stiffness distribution. This information is then sub-sampled at a user specified resolution to construct elements, and then filtered to eliminate elements that do not represent bone.

This procedure produces a hexahedral mesh that, although being numerically sound, does not accurately represent surface geometry smoothly. The critical cement-THA stem interface is insufficiently modelled directly using CT scans, although the positioning of the implant relative to the bone is provided. Surface scanning the implants prior to implantation allows generation of an accurate, smooth implant meshes that with the assistance of CT scan information can be positioned along with the corresponding cement volumes within the relevant intact femoral models. This achieves both an accurate and smooth cement-THA stem interface and positioning within the femur.

The implanted femoral model displaying the most favourable response to the loading condition will form the basis of further numerical modelling endeavouring to optimise material properties to further increase THA service life.

5.3 Methodology

5.3.1 Cadaveric Specimen Selection

The prerequisite to use human cadaveric specimens within this research necessitated liaison with The University of Adelaide School of Anatomical Sciences. After completion of the appropriate legal and ethical requirements, selection and acquisition of a pair of suitable

cadaveric femora was achieved with the assistance of the Technical Officer (Mr Wesley Fisk) in charge of the Ray Last Anatomy Laboratory.

Initially, ten intact embalmed pairs of human femora were made available for preliminary x-ray analysis to assess bone density and geometry. The average age of the specimen donors was 63 years (range: 45-89), with the composition being 3 male, 7 female.

X-rays of the Anterior-Posterior (AP) and Lateral-Medial (LM) orientations were performed for both hips in each individual. The x-rays were performed at the Department of Physiotherapy, University of South Australia. Interestingly, 3 of the donors had previously received THA surgery, and so were excluded from this research.

From the remaining group of 7 pairs of femora, one pair belonging to a male donor aged 58 was chosen. This pair of femora displayed good bone density with generic geometry. An x-ray image of the chosen pair of femora can be seen in Figure 5.3.

5.3.2 Implant Selection

The selection of appropriately sized THA stems from the specified product ranges for the cadaveric femora was made at the Royal Adelaide Hospital Department of Orthopaedics and Trauma, with the assistance of Dr Mellick Chehade (PhD), the orthopaedic surgeon chosen to implant the femoral stems. The THA stem size selection process followed the standard protocol used within the institution. This required more precisely orientated and magnified x-rays.

With the aid of the appropriate x-rays and the relevant THA templating systems, suitable stem sizes were chosen that matched the contour of the proximal femoral canals and filled them the most completely while maintaining centre of rotation of the femoral head and femoral neck shaft angle (offset). Both stem 'A' and stem 'B' were both found to be standard offset size 3 items from their respective product ranges. Stem 'A' was allocated for implantation into the right-hand femur, and stem 'B' into the left-hand femur.



Figure 5.3: X-ray image showing the pelvic region of the cadaveric specimen chosen for this research.

The required implants and associated surgical required hardware for the implantation process were then sourced.

5.3.3 Surgical Extraction of the Cadaveric Femora

Once all x-rays required for pre-operative planning had been recorded, the cadaveric femora were surgically extracted by Mr Wesley Fisk, Technical Officer in charge of the Ray Last Anatomy Laboratory. The bones were stripped of the majority of attached soft tissue, however a small amount was retained in an attempt to maintain moisture levels. The explanted embalmed femora can be seen in Figure 5.4.



Figure 5.4: Explanted embalmed cadaveric femora with excess soft tissue removed.

5.3.4 Numerical Model Generation for the Intact Femora

Keyek et al. (1990) developed a procedure for the rapid generation of patient-specific three-dimensional finite element models of bones with material properties derived form the CT scan digital data. A program based on the procedure, titled 'CT2FEM', was generated by Viceconti et al. (1998) and made available within the public domain. It was sourced and executed using a Silicon Graphics Irix 6.5 operative system.

5.3.4.1 CT Scanning

Single CT scans record digital information concerning material density distribution throughout a two dimensional region. Scan resolution and size is determined by the number and size of pixels located within the planar scan to produce an ordered grid. The CT scanner used for this research was a Marconi Medical Systems PQ6000 CT Scanner, kindly made available by the Department of Radiology, Royal Adelaide Hospital. The CT scanner was operated at the following settings: 120kVp; 200mA; 0.2s; slice thickness 1.5mm; pixel size, 0.5859mm; 512x512 matrix. Each pixel is assigned a 'CT number' obtained as a measure of the density at

the respective location within the specimen being examined. These CT numbers are organised and stored in a 16-bit binary format. One of the cropped CT scan images is provided in Figure 5.5.

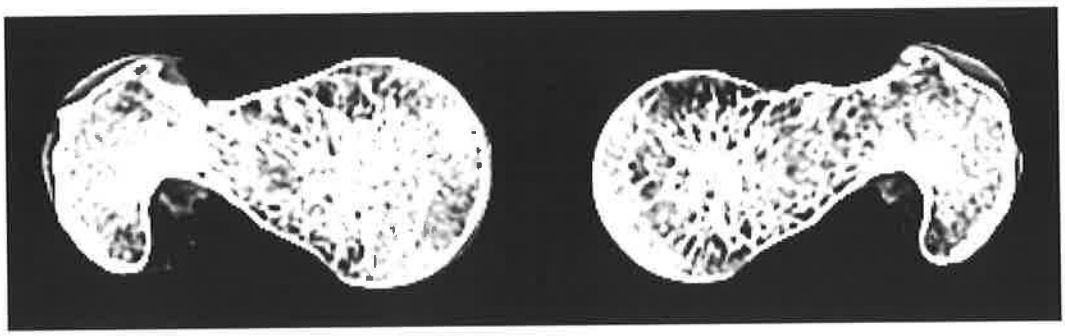


Figure 5.5: CT scan through the femoral heads of the cadaveric femora.

A three dimensional image of the specimens is achieved through acquisition of multiple scans each incremented in a direction normal to the scan plane. This three dimensional image can be stored as a single file, containing the CT numbers defining image density ordered relative to their position within the successive scans.

5.3.4.2 Finite Element Model Generation

Three dimensional 8-noded solid hexahedral elements are generated from the binary file containing the three dimensional density image. Element size is user specified, however their size cannot be smaller than the distance between consecutive CT scan slices. Cubic elements with an edge length of 2mm are used to generate models within this research.

Linear elastic material properties are allocated to each element according to the density of the CT scan data within the element. An empirical formula developed by Carter & Hayes (1977) allows the Young's Modulus to be calculated from the density at any location within the bone, and is expressed below in Equation 5.1 as:

$$E = 3790 \times \dot{\varepsilon}^{0.06} \times \rho^{3}, \qquad \textbf{(5.1)}$$

for $0.10 \leq \rho \leq 2.0 g/cm^3$, $0.001 \leq \dot{\varepsilon} \leq 10.0 s^{-1}$, where E is Young's Modulus (MPa), $\dot{\varepsilon}$ is the rate of strain (s^{-1}) and ρ is apparent density (g/cm^3). Within this research a rate of strain of $\dot{\varepsilon} = 0.01 s^{-1}$ is employed throughout the entire bone, as used by Keyak et al. (1990).

Prior to implementing the density to modulus relationship developed by Carter & Hayes (1977), values for density must be obtained from the CT numbers. Fortunately, a linear relationship exists between the CT number and the apparent density of bone, allowing a simple conversion from CT number to density, required for the calculation of Young's Modulus. Two locations are used to perform a linear calibration of the CT numbers and convert them into density values. The first location represents a region of thick cortical bone and assigning it the value of $1.8 g/cm^3$, assumed to be the average density of cortical bone (Keyak et al. 1990), and the second location is contained within a volume of water placed within the scan volume that represents non-bone regions with an assigned (unrealistic) density $0 g/cm^3$, allowing simple filtering of soft tissue.

The Young's Modulus for each element is determined by the average Young's Modulus for all pixels that are located completely or partially within the element boundaries. For those pixels not completely within the element boundaries a volume fraction calculation is performed. This procedure is also used for those pixels that are partially external to the bone. A Poisson's ratio of 0.4 is allocated to all elements, as used by Keyak et al. (1990).

The resultant output from the 'CT2FEM' program was manipulated to allow generation of nodes, elements and material properties within ANSYS finite element analysis software. A contour plot of Young's Modulus distribution within the right-hand intact femoral model is presented in Figure 5.6. The intact femoral models for the left-hand and right-hand are presented in Figure 5.7.

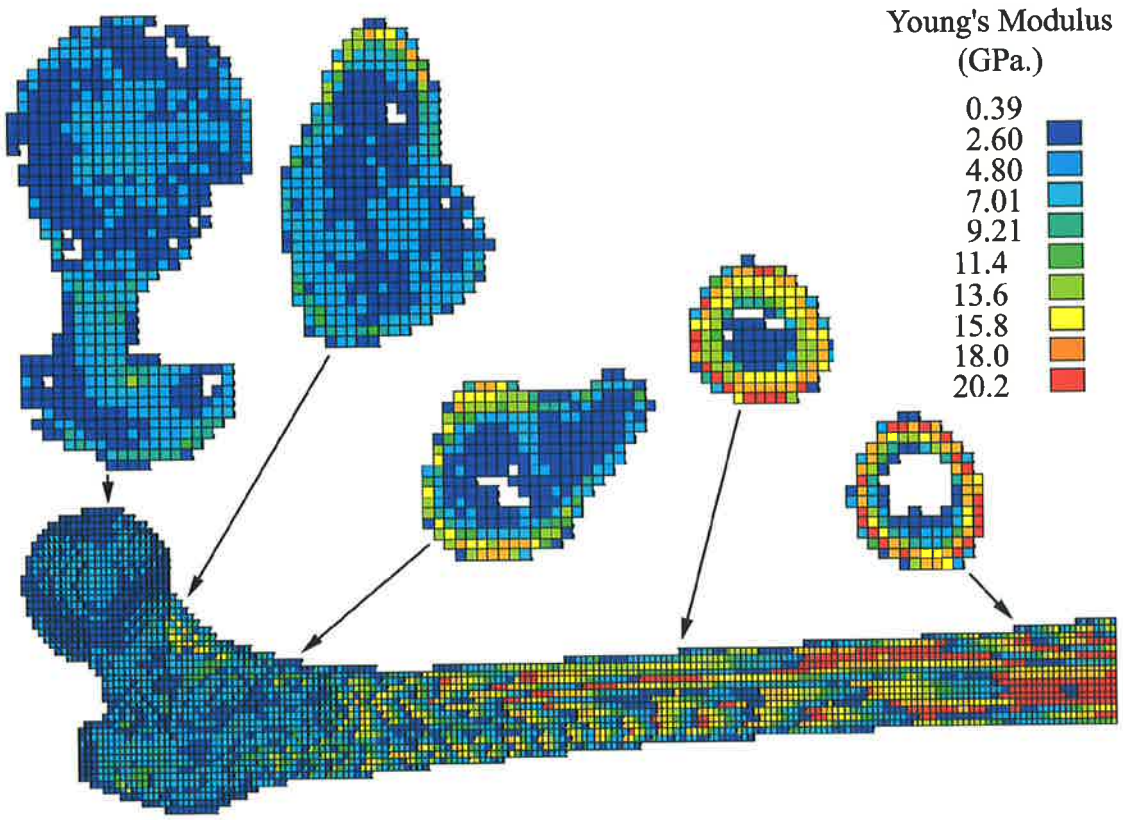


Figure 5.6: Young's Modulus contour plot for the right-hand intact femoral model showing cross sectional variation.

This process of model generation is robust, however first-order elements compromise the accuracy of the curved exterior bone surface and the transition between cancellous and cortical bone. These inaccuracies can be reduced through the use of smaller elements, and are less relevant if resultant quantities are not recorded on the exterior bone surface. Keyak et al. (1990) suggests that the use of element with side length 4mm of less provides adequate representation of both the bone surface and any abrupt changes in material properties within the cancellous bone. The overall distribution of model density is maintained through the use of the volume fraction calculation employed when allocating elemental elastic modulii.

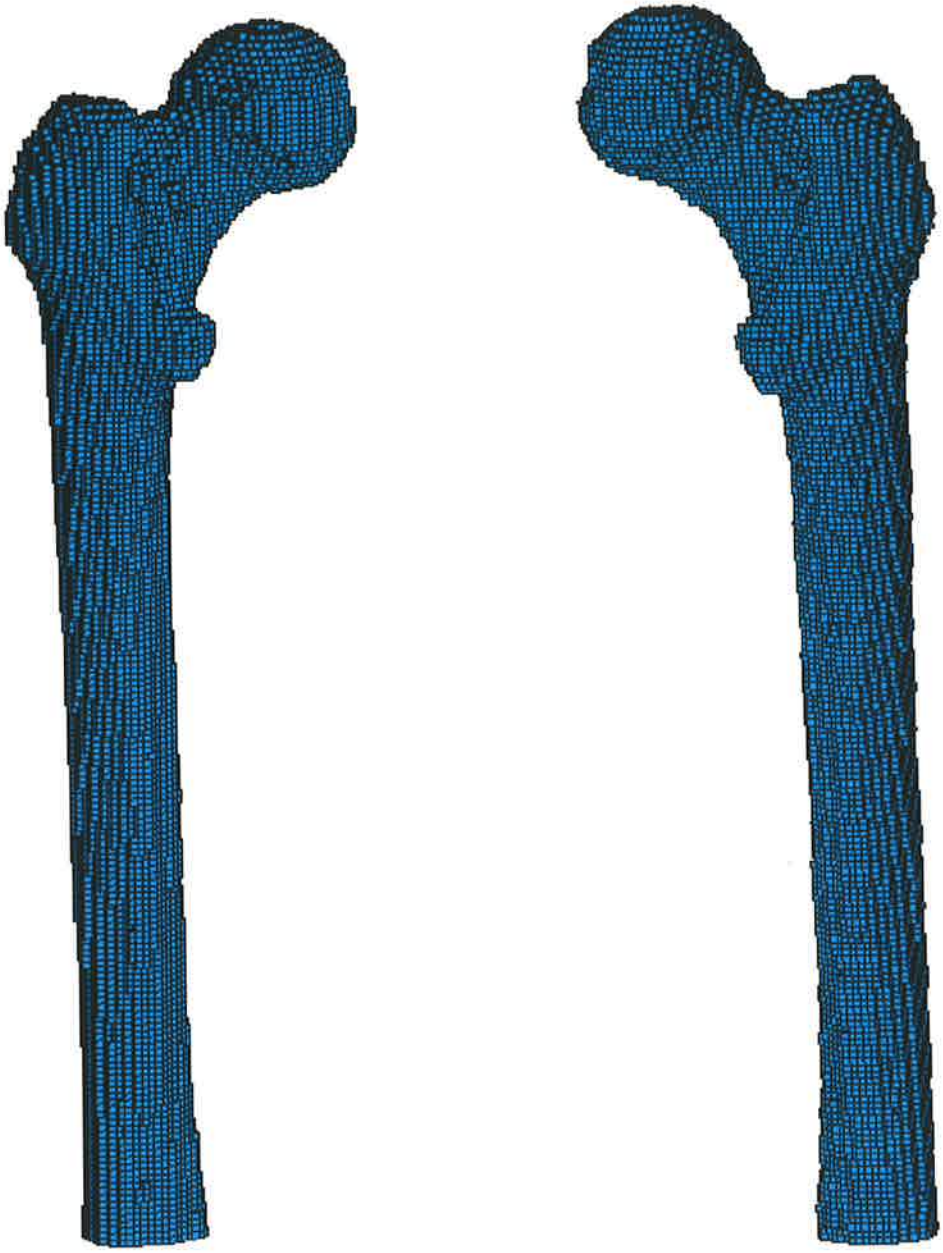


Figure 5.7: Left-hand and right-hand intact femoral model meshes. The use of cubic elements gives a jagged surface.

The potentially significant underestimation of density and therefore Young's Modulus due to the presence of fatty tissue such as that found in bone marrow is neglected (Keyak et al. 1990).

5.3.4.3 Intact Femoral Model Boundary Conditions

Boundary conditions for the numerical models are based on findings presented within Chapter 4.

As suggested within Chapter 4, a refined level of muscular inclusion for the 45% gait cycle is adopted, with individual muscular loading distributed over natural attachment areas. This muscular loading data was originally sourced from Duda et al. (1998), and translated into the model coordinate system.

The femoral models are fully constrained in translation and rotation at the distal end, with the femoral length shortened to increase solution efficiency, again, following the findings of Chapter 4.

5.3.5 Numerical Models of Implanted Femora

5.3.5.1 Creation of THA Stem Meshes

Numerical models for both stem 'A' and stem 'B' were created using sophisticated surface scanning technology.

A non-contact 3D laser scanner (ModelMaker X70, 3D Scanners, London) suspended from a portable measuring arm (FaroArm 2.4m, FARO Technologies Inc, Florida) was used to gather 'point clouds' that correspond to the spatial coordinates of points lying on the stem surface. Concentric Advanced Manufacturing Facility based in Adelaide, Australia, provided this service. The portable measuring arm is suggested to have an accuracy of +/- 0.025mm, and the laser scanner an accuracy of +/- 0.05mm. Talcum powder was dusted onto the stem surfaces to aid in the scanning process.

This point data was then imported into Solid Edge CAD software, allowing generation of solid models. Inclusion of the geometric detail around the top of the implant exterior to the cement was neglected, as it has no influence on the stem volume enclosed within the femur.

The solid models were then imported into the ANSYS environment, and meshed with second-order quadrilateral surface elements and second-order tetrahedral solid elements. An element size was chosen that captured significant geometric resolution whilst maintaining reasonable numerical efficiency. The model mesh for the stem 'A' can be seen in Figure 5.8, and for stem 'B' in Figure 5.9.

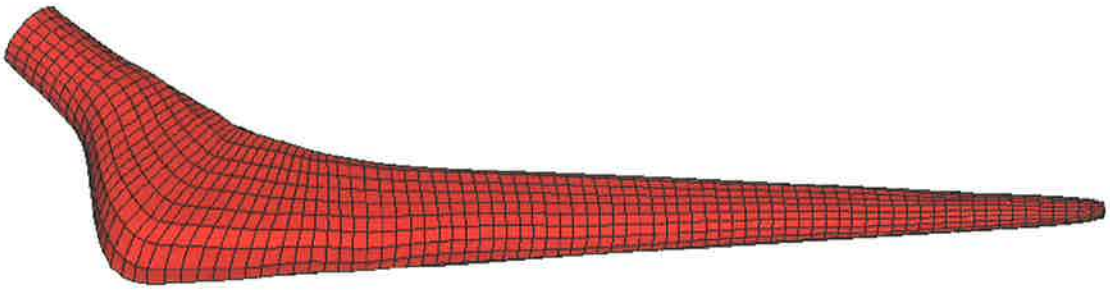


Figure 5.8: Model mesh for stem 'A', neglecting some geometric detail in regions exterior to the cement.

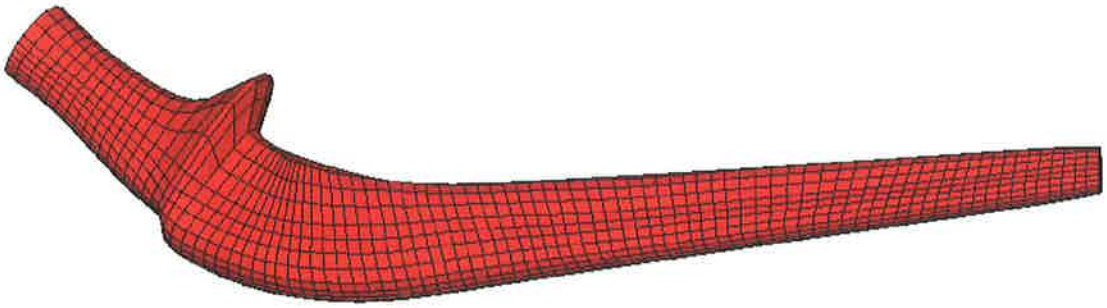


Figure 5.9: Model mesh for stem 'B', neglecting some geometric detail in regions exterior to the cement. Although included, the image does not clearly show grooves in the stem.

5.3.5.2 Surgical Implantation of Cadaveric Femora

Implantation of stem 'A' and stem 'B' into the pair of the cadaveric femora was required to aid in the generation of the implanted numerical models. Within an appropriate surgical laboratory environment, orthopaedic surgeon, Dr Mellick Chehade, completed the implantation procedure that he had preoperatively planned. Care was taken to ensure that the surgery was conducted in a realistic manner, with all resources available.

This process yielded implanted femora with bone geometry, implant positioning and cement thickness all resulting from the actions of an experienced orthopaedic surgeon. Numerical models based on these implanted femora are therefore assumed to have realistic geometric characteristics. The right-hand femur containing stem 'A' can be viewed in Figure 5.10, while the left-hand femur containing stem 'B' can be viewed in Figure 5.11. Other images taken during the implantation procedure are located in Appendix A (Figures A.6 to A.9).



Figure 5.10: Right-hand cadaveric femur with surgically implanted stem 'A'.



Figure 5.11: Left-hand cadaveric femur with surgically implanted stem 'B'.

5.3.5.3 CT Scanning of Implantation of Cadaveric femora

The implanted femora were again CT scanned, this time to allow measurements to be taken that assist in alignment of the THA stem and to assess cement thickness. All settings within the CT scanner were returned to the values previously used within this research. Images output from the scanner included 'diffraction artefacts', visible in Figure 5.12 as regions of darkened image contrast extending from the implant surface.

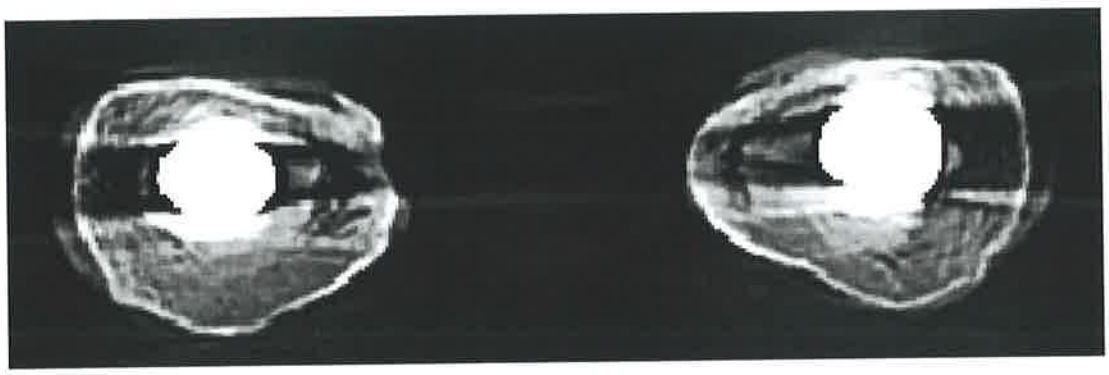


Figure 5.12: This CT scan of the implanted femora includes 'diffraction artefacts' that darken regions within the image giving a false indication of bone density.

These 'diffraction artefacts' cause significant errors within the images, eliminating the possibility of generating new models directly form this data. Consequently, the CT scans are only used to measure implant and cement positions (data that was not compromised by artefacts).

5.3.5.4 Implanted Model Generation

Femoral models with cemented THA stems have interfacial regions defining the bone-cement and cement-THA stem boundaries. These material interfaces require significant attention during the model building process.

The cement-bone interface is identical for all implanted femoral models, however the cement-THA stem interfaces associated with matt and polished implant surfaces differ.

Formation of the common cement-bone interface included a geometric constraint. As the existing intact femoral models were modified to create the implanted femoral models, removal of hexahedral solid elements was necessary to fabricate the cement volume. Complete elements were removed that were interpreted to lie within the cement volume suggested by the CT scans. Subsequently, the interface is not geometrically accurate and dependant on element size, as indicated in Figure 5.13. However the Author believes this interface is adequately modelled and is pictured in Figure 5.14.

5.3.5.4.1 Stem 'B' Implanted Femoral Model

The implant mesh for stem 'B' was aligned within the cement volume of the left-hand femur according to the CT scans. The exterior THA stem mesh dictated the cement-THA stem interface geometry, and the void between this interface and the bone-cement interface was filled with second-order tetrahedral solid elements, modelling cement. The cement was assigned a Young's Modulus of 3000 Mpa (Automation Creations, 2002) and Poisson's ratio of 0.3 (Gross & Abel, 2001). The Young's Modulus for cement varies with type and it should be noted that varying this property may alter calculated interfacial stresses. The CoCr stem 'B' was assigned

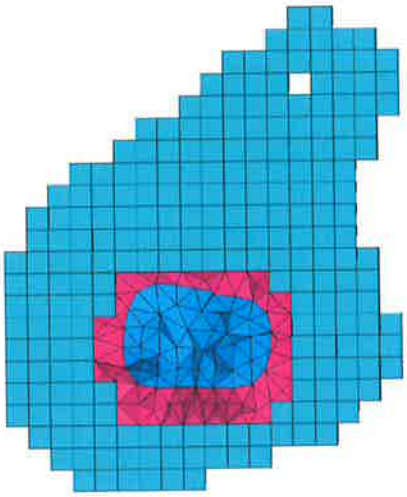


Figure 5.13: Cross-section through the left-hand implanted femur mesh indicating bone, cement and THA stem locations within the mesh.

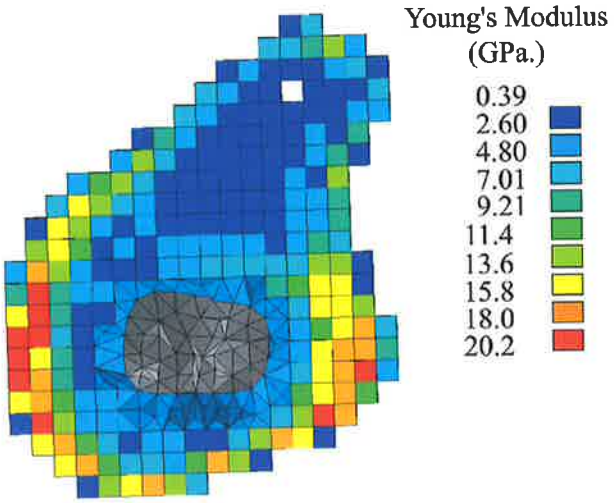


Figure 5.14: Young's Modulus contour plot showing material stiffness differential at the bone-cement interface.

a Young's Modulus of 234 Gpa (Automation Creations, 2002) and Poisson's ratio of 0.3 (Gross & Abel, 2001).

Stem 'B' has a matt surface finish, designed to achieve mechanical bonding with cement, allowing no interfacial movement. This research assumes this bond is complete and ideal, and models this interface as such. Elements modelling cement and THA stem regions share common nodes along the interface, generating this ideal bond. This same technique is used to model the bone-cement bond in all models. The corresponding model mesh can be seen in Figure 5.15.

5.3.5.4.2 Stem 'A' Implanted Femoral Model

Generation of the model for the right-hand femur implanted with stem 'A' followed the same procedure used to model the left-hand femur implanted with stem 'B', although the cement-THA stem interface was modelled differently. As stem 'A' is also CoCr, the same material properties were assigned to both the implant and cement.

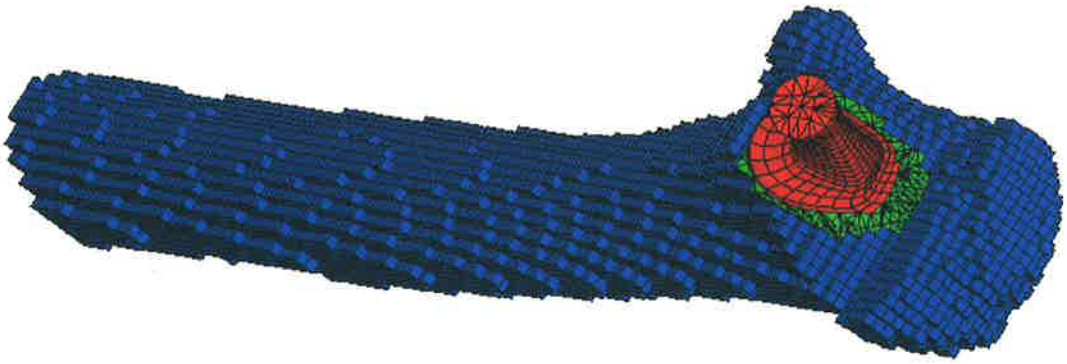


Figure 5.15: Model mesh for the left-hand femur implanted with stem 'B'.

A more complex cement-THA stem interface exists with the polished stem 'A'. The polished surface finish endeavours to prevent mechanical bonding with cement, and allow movement at the interface. The THA stem is believed to achieve a lock with the cement due to its double-tapered wedge geometry. This is numerically modelled using contact elements requiring a nonlinear analysis.

The contact analysis used within this research allows the THA stem and cement surfaces to sustain or disengage contact as well as slide relative to each other. To model this process efficiently, the cement and THA stem have identical meshes at the interface, and although the elements and nodes are located in the same location, they are independent entities. Connectivity between the THA stem and the cement is achieved with contact elements, generated through coincident nodes at this interface. The implant is assigned a 'closed' initial contact condition, preventing rigid body motion and allowing solution iterations to commence.

The three-dimensional, point-to-point contact elements used allow transfer of compressive loading normal to the contact interface. Tensile forces are not transferred across the interface, allowing separation. The contact elements support transfer of shear loading tangential to the contact interface. Shear loading and sliding are governed by a coefficient of friction. In order to understand the influence surface finish, solutions resulting from assigned frictional coefficients of 0.1, 0.2 and 0.3 are generated. This range of frictional coefficients was selected based on a

range of reasonable estimates in line with those suggested by Viceconti et al. (2000) and allows understanding of the influence friction has within the analysis.

Investigation into the performance of stem 'A' with matt surface finish was also undertaken, using the cement-THA stem interfacial modelling procedure implemented for the stem 'B'. The mesh for all right-hand femoral models implanted with stem 'A' variations can be seen in Figure 5.16.



Figure 5.16: Model mesh for the right-hand femur implanted with stem 'A'.

5.3.5.5 Implanted Femoral Model Boundary Conditions

Use of the intact femoral models as the basis for the implanted femoral models allowed all muscular loading and restraint conditions to be retained, with the exception of the hip joint loading applied through the femoral head.

As THA intends to maintain location and centre of rotation of the femoral head, all elements within the femoral head with applied loads were retained and attached to the THA stem through use of an arbitrary rigid support structure. This arbitrary rigid support structure connects the elements within the femoral head with applied loads to the THA stem. The retained elements within the femoral head and the arbitrary rigid support structure were assigned the same

mechanical properties as the THA stem. This method guarantees identical hip joint loading between intact and implanted femoral models, assisting results comparison.

5.4 Analysis

The intact and implanted femoral models with rigidly bonded THA stems are simple linear static analysis. Economical solution times for these large size numerical models require the use of a Preconditioned Conjugate Gradient (PCG) solver (ANSYS V5.7.1 2002), iterating to a convergence criterion of 1×10^{-8}.

The models including contact follow a nonlinear static analysis, using the same solver and convergence criterion. The loading is applied incrementally, and the solution converged for force and displacement. Seven load increments were required to achieve convergence.

5.5 Model Results and Discussion

All numerical models within this study have been equipped with paths joining consecutive nodes located along the anterior, posterior, medial and lateral upper femoral shaft surfaces, at one element depth (2mm) from the surface. Result comparison between models is achieved by plotting solution quantities along these paths. This method of displaying results is similar to that used within Chapter 4, however overestimated surface solutions resulting from local muscular loading are avoided. An increased number of nodes per path is employed to improve solution resolution.

As in Chapter 4, Von Mise's equivalent strain energy density was chosen as the output solution quantity. As previously discussed, this quantity is reported to be fundamental in influencing bone remodelling.

Results extracted along the paths are smoothed using a moving average algorithm. This smoothing algorithm calculates for each point along the path a value corresponding to the mean

using 5 points either side of the point of interest. This process allows a less variable result plot without significant loss of accuracy.

5.5.1 Intact Femoral Models

Resultant Von Mise's equivalent strain energy density obtained from numerical models of the left-hand and right-hand intact femora are displayed in Figure 5.17 and Figure 5.18. These intact femoral models indicate that for the 45% gait cycle, the Von Mise's equivalent strain energy density within the upper femoral shaft is relatively constant in the anterior and lateral regions, whilst increasing distally in the posterior region and decreasing distally in the medial region.

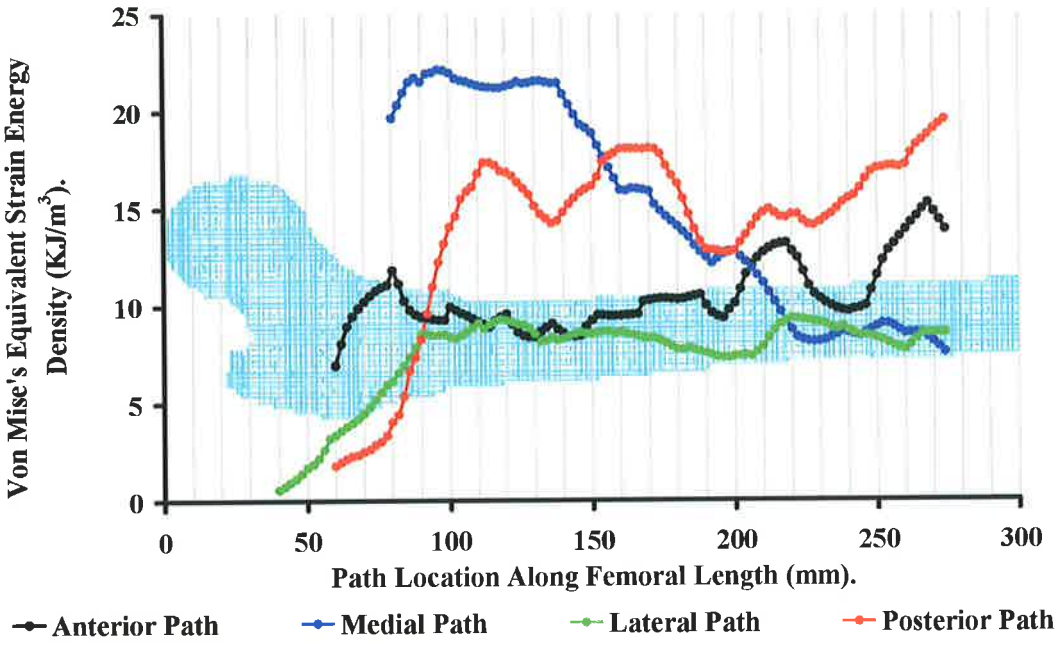


Figure 5.17: Resulting Von Mise's Equivalent Strain Energy Density, plotted along all paths for the intact left-hand femoral model. Silhouette in the plots background indicates path region along femur.

Comparison of solutions for similar paths in the left-hand and right-hand intact femoral models shows little relative difference. The discrepancies between the two intact femoral models are

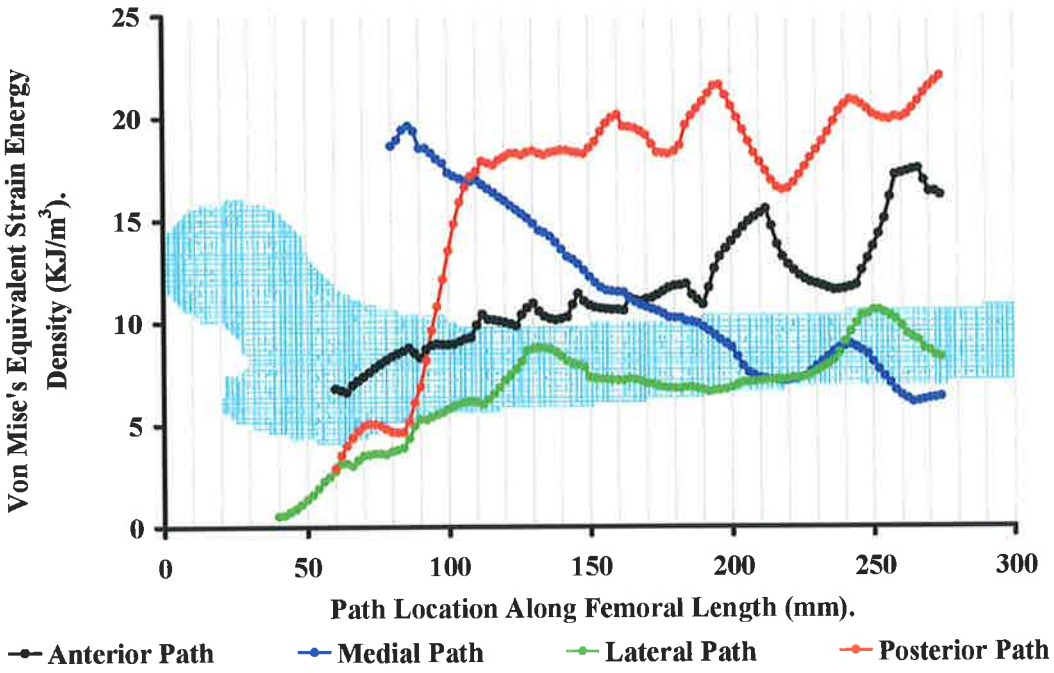


Figure 5.18: Resulting Von Mise's Equivalent Strain Energy Density, plotted along all paths for the intact right-hand femoral model.

understood to result of many compounding factors associated with independent model construction. Model geometry and material properties are not identical, however small variations in load application and alignment, along with location of result extraction paths are more believed to exert the greatest influence in this result discrepancy. Specifically, results for the left and right medial paths between 100-150 mm are believed to differ mainly due to location of applied muscular load.

Comparison of the current results with results extracted on the surface of the model developed within Chapter 4, displayed in Figure 5.11, indicate the current models experience a reduced magnitude of Von Mise's equivalent strain energy density. This can be explained as the result of numerous factors, discussed in following paragraphs.

A level of bending is experienced by the model as a response to the applied loading condition, and so extraction of results beneath the surface, closer to the effective neutral axis, provides smaller stresses and strain energy densities. Furthermore, the results extracted from the current model will be smaller in magnitude than those found within Chapter 4, since the current model is approximately 15% physically larger with loading conditions the same for both. It is believed that the most significant reason for the differences in results extracted from the current model and that used in Chapter 4 is the reduced influence of localised high surface stresses resulting from muscular loading.

Discrepancies in Von Mise's equivalent strain energy density trends within the upper femoral shafts of the current models and the model generated within Chapter 4 could be the result of the deformed femoral neck geometry associated with the model developed within Chapter 4. Unfortunately simulating a deformed femoral neck in the present model to assess potential differences is unfeasible due to resource constraints and the automated CT scan based method of model generation employed. The current models in this chapter are believed to be more suitable for researching implantation.

5.5.2 Implanted Femoral Models

To allow straightforward comparison of implanted femoral response for all THA stem variations investigated, a measure of the change in response post implantation was used. This change in femoral response is defined as the change in Von Mise's equivalent strain energy density between implanted and intact states, expressed as a percentage of the intact state. The right-hand femoral models implanted with stem 'A' variations were compared to the intact right-hand femur model, and the left-hand femur model implanted with stem 'B' was compared to the intact left-hand femur model.

A plot showing the change in femoral response post implantation for all variations of stem 'A' and for stem 'B' is presented for the medial path in Figure 5.19, and for the anterior, posterior

and lateral paths within the Appendix A as Figure A.10, Figure A.11 and Figure A.12 respectively.

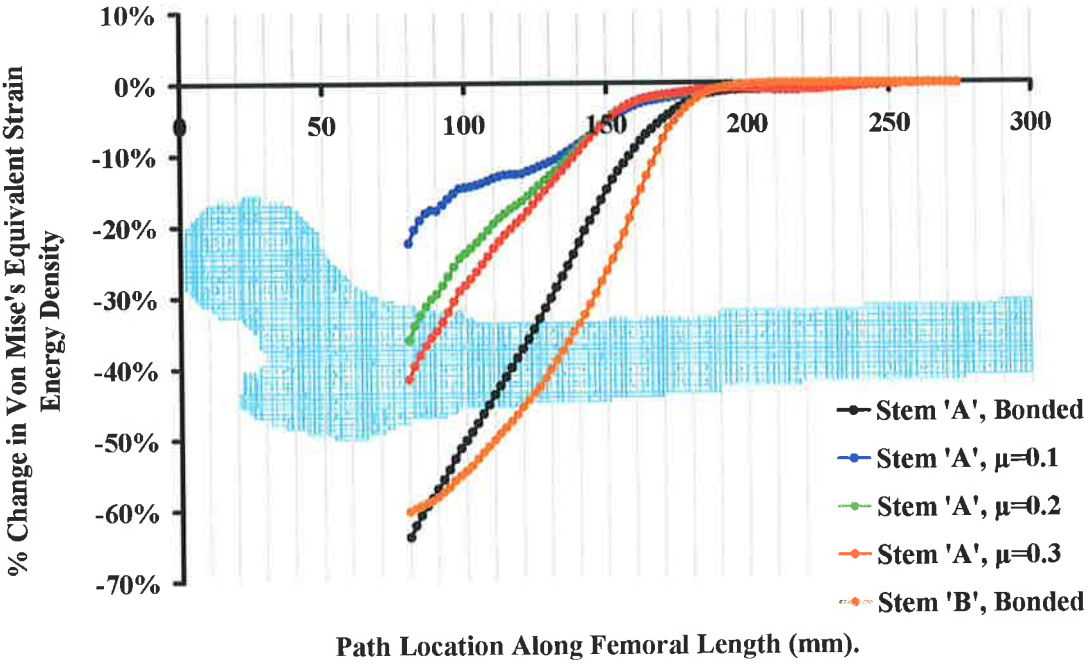


Figure 5.19: Comparison of percentage change in Von Mise's Equivalent Strain Energy Density distribution along the Medial path following implantation.

Analysis of these results indicate that THA stem surface finish influences the level of femoral response. Generally, implantation of all THA stem variations investigated reduced the amount of Von Mise's equivalent strain energy density within the upper femoral shaft. At many locations, the implanted femoral models experienced less than 50% of the Von Mise's equivalent strain energy density found in the intact femoral models.

Numerical models based on stem 'A' provided insight into the influence of the cement-THA stem interface on femoral response. As the interface geometry was constant, conclusions can be made about the femoral response to cement-THA stem interfacial characteristics. Allowing the THA stem and cement surfaces to sustain or disengage contact and slide with an associated

frictional coefficient resulted in an increased femoral response relative to the fully bonded condition except for within the mid-to-lower anterior path, believed to be a consequence of chosen loading regime.

Within the contact analysis the frictional coefficient was altered to assess the change in femoral response. Lower frictional coefficients allowed more distal movement of the wedge shaped THA stem, and increased femoral response in the upper femoral shaft. With identical loading, a frictional coefficient of 0.1 allowed 0.40mm of subsidence, while a frictional coefficient of 0.2 allowed 0.23mm of subsidence and a frictional coefficient of 0.3 allowed 0.17mm of subsidence.

One distinguishing feature of stem 'B' is the collar designed to transfer increased loading within upper regions of the femoral shaft, particularly in the medial section. Findings from this research indicate that this did not occur, probably due to the strength of the cement-THA stem bond over the entire interface. It is believed that if the THA stem was allowed to slide within the cement then this collar would have had greater influence.

Comparison of implanted femoral models suggests that bonded stem 'A' is superior to bonded stem 'B' in generating a femoral response for the applied loading conditions. Figure 5.20 displays the implanted femoral response to both bonded stems for all paths on the same set of axes for direct comparison.

Implantation of bonded stems 'A' and 'B' provide similar femoral response trends along all paths within the upper femoral shaft, however bonded stem 'A' extracts a more favourable femoral response at nearly all locations. It was endeavoured to model both stems with the same cement-THA stem interfacial conditions and material properties, however undoubtedly there are differences in stem positioning and cement mantle thickness that could have influenced the comparison. Further, differences between the intact left and right femoral models, particularly

within the anterior and lateral paths make direct comparison of the implanted femoral models more difficult.

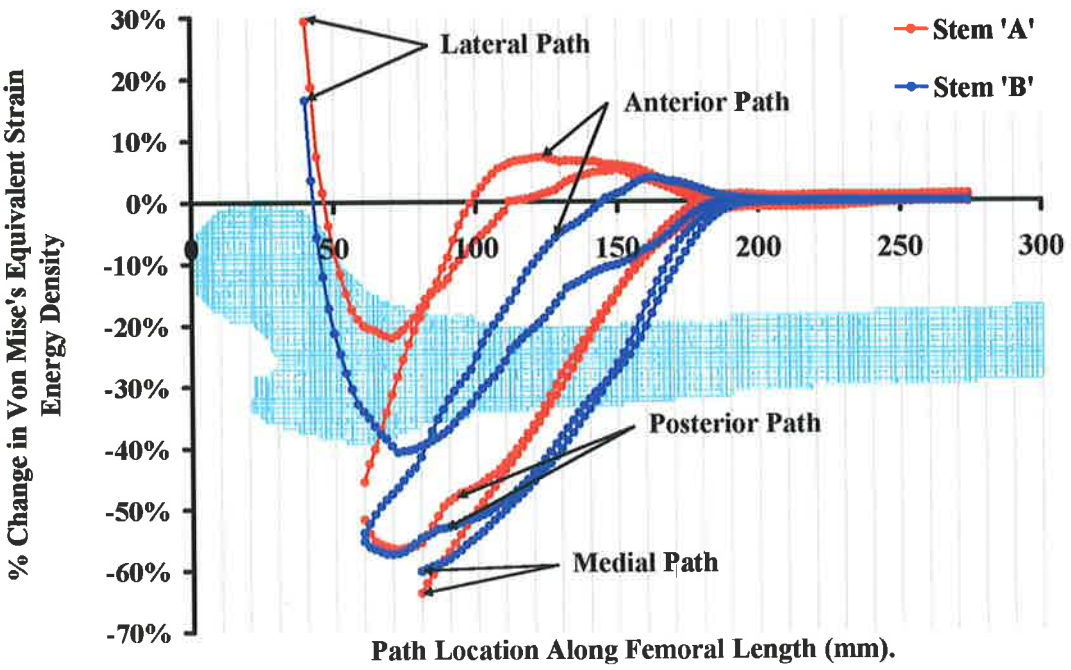


Figure 5.20: Comparison of percentage change inVon Mise's Equivalent Strain Energy Density Distribution along all paths caused by the bonded THA stems.

5.6 Model Verification

Model validation is assumed for the intact and implanted femoral models through use of an increased mesh density as in previously verified models within Chapter 4. Implanted femoral models use second order elements for the cement and THA stems, with a mesh density finer than that used to model the bone. Similar results extracted from the independently created left-hand and right-hand femoral models also suggest validation.

5.7 Conclusion

This investigation has discovered that for a refined 45% gait cycle loading regime, both the smooth and rough surface finished variations of stem 'A' (the CPT THA stem), are superior in femoral response than the rough surface finished stem 'B' (the Spectron THA stem).

Although the smooth surface finished versions of stem 'A' were suggested to promote a more desirable femoral response than the rough surface finished version, the added computational expense associated with the nonlinear contact analysis inhibits its use as a basis within further optimisation analysis.

Hence, the right-hand femoral model implanted with the rough surface finished version of stem 'A' is chosen for further development. This model requires a simple linear static analysis with a relatively small solution time.

Chapter 6

OPTIMISATION OF IMPLANT CHARACTERISTICS FOR EXTENDED SERVICE LIFE

6.1 Introduction

This study uses models and findings from previous sections of this research within an advanced optimisation method to derive an implant design approach that provides extended service life by minimising stress shielding. It is suggested that alteration of the THA stem stiffness along its length can reduce the level of stress shielding within the femur, however this distribution profile, along with other consequences resulting from a distributed stiffness are somewhat unknown.

Initially, for a given loading regime, geometries and material properties, femoral stress shielding and maximum cement stress response to variations in homogeneous THA stem stiffness will be investigated to suggest limitations and benchmarks in the calculation of optimally distributed THA stem stiffness. With the assistance of this information, formulation of the THA stem stiffness distribution optimisation process is possible. This optimisation of the THA stem stiffness distribution will be executed to determine if extensions in THA service life can be achieved through the reductions in stress shielding whilst maintaining acceptable stress levels within the cement.

6.2 Research Aim

This research endeavours to find the relationship between homogeneous THA stem stiffness, maximum cement stress and extent of stress shielding within the upper femoral shaft. Following this, it is proposed that an optimal THA stem stiffness distribution be calculated that may reduce stress shielding within the upper femoral shaft for a nominated maximum cement stress.

6.3 Investigation into Stress Shielding and Maximum Cement Stress Response to Variation of Homogeneous THA Stem Stiffness

Investigation of femoral response to cemented THA stems of differing homogenous stiffness will provide insight into the correlation between reductions in stress shielding associated with more flexible THA stems and corresponding increases in design limiting interfacial stresses.

6.3.1 Research Methodology

This investigation used a numerical model based on right-hand femur geometry with cemented THA stem 'A' geometry (CPT THA stem) with rough surface finish, sourced from the previous chapter. As previously used and described; a refined 45% gait cycle loading regime was employed, the distal end of the femoral shaft was fixed in all degrees of freedom and all material characteristics were unchanged.

As with prior investigations, the same paths on the anterior, posterior, medial and lateral upper femoral shaft surfaces are used to record Von Mise's equivalent strain energy density values, allowing stress shielding attributes to be visualised. In order to numerically quantify the magnitude of stress shielding for a given THA stem stiffness, the value of Von Mise's equivalent strain energy density at 5 equidistantly spaced points along each of these paths is recorded, and a stress shielding indicator is calculated. To calculate the stress shielding indicator, the difference between the intact and implanted Von Mise's equivalent strain energy

density is calculated at each of the 5 points per path. All positive differences (meaning there is less energy density post-implantation) are summed, and negative differences (meaning there is more energy density post-implantation) are neglected. This summed value is believed to adequately represent the level of stress shielding caused by a THA stem, and is referred to as the Von Mise's equivalent strain energy density indicator.

Within this research interfacial stresses are assumed to be adequately characterised by Von Mise's equivalent stresses within the cement itself. To gain an appreciation of where the maximum cement stresses, and hence the limiting interfacial stress region existed, preliminary solutions were generated for the entire range of THA stem stiffness values. The upper medial portion of the cement was consistently the region with highest Von Mise's equivalent stress profile, and so 10 nodes surrounding this region were selected to have their resultant Von Mise's equivalent stress value summed to provide an indication of interfacial stressing.

Solutions to the analysis are obtained for different THA stem Young's Moduli, ranging from a relatively flexible 25 GPa to a relatively stiff 250 GPa.

6.3.2 Results

This research indicates that homogeneous THA stem stiffness influences both the level of stress shielding and interfacial stresses within the implanted femoral system. Higher values of homogeneous THA stem stiffness generate greater levels of stress shielding within the upper femoral shaft, however lower levels of interfacial stresses. While lower values of homogeneous THA stem stiffness generate lower levels of stress shielding within the upper femoral shaft and greater levels of interfacial stresses.

To measure the relative influence of homogeneous THA stem stiffness on interfacial stress and stress shielding, results were normalised with the values found for a CoCr THA stem, which is the real material used for the specific THA stem geometry. These results are provided in Figure 6.1. This figure also indicates results for both titanium and CoCr materials and that for the given

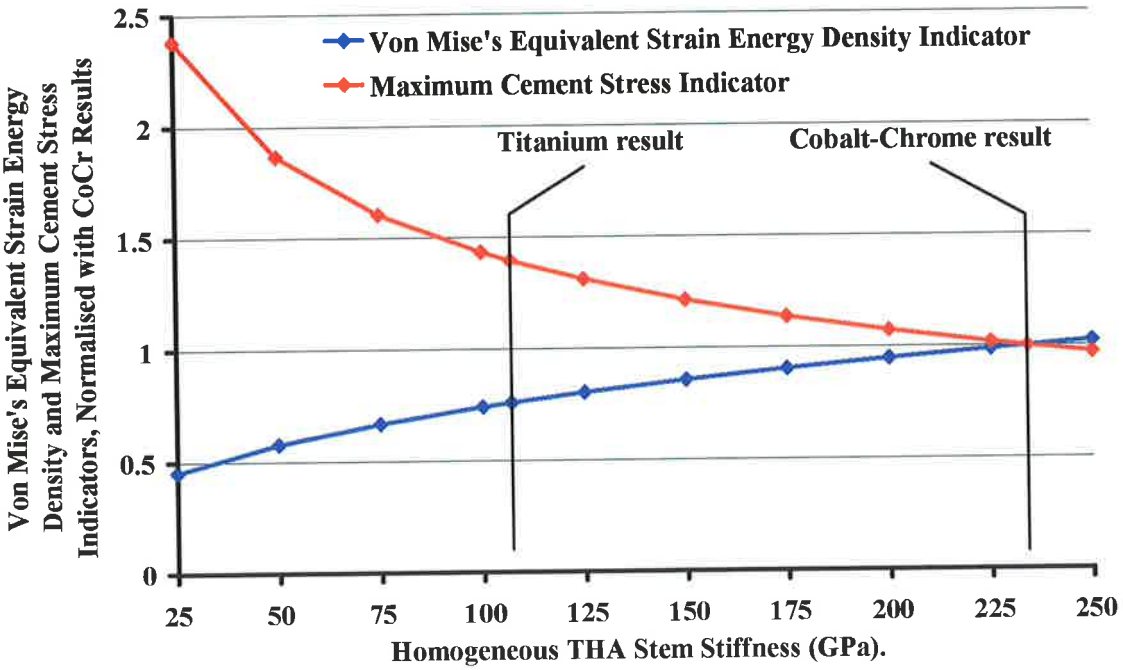


Figure 6.1: Variations in Von Mise's Equivalent Strain Energy Density and maximum cement stress for variations in homogeneous THA stem stiffness. The results are normalised with the CoCr results.

model, a titanium THA stem provides 24.1% less stress shielding but 39.6% more interfacial stresses than equivalent CoCr THA stem.

Changes in Von Mise's equivalent strain energy density from the intact condition within the upper femoral shaft along the four paths for both homogeneous titanium and CoCr THA stem materials are provided in Figure 6.2. This figure indicates that generally a more flexible THA stem imparts more Von Mise's equivalent strain energy density within the upper femoral shaft than a stiffer THA stem, although a similar Von Mise's equivalent strain energy density profile is retained.

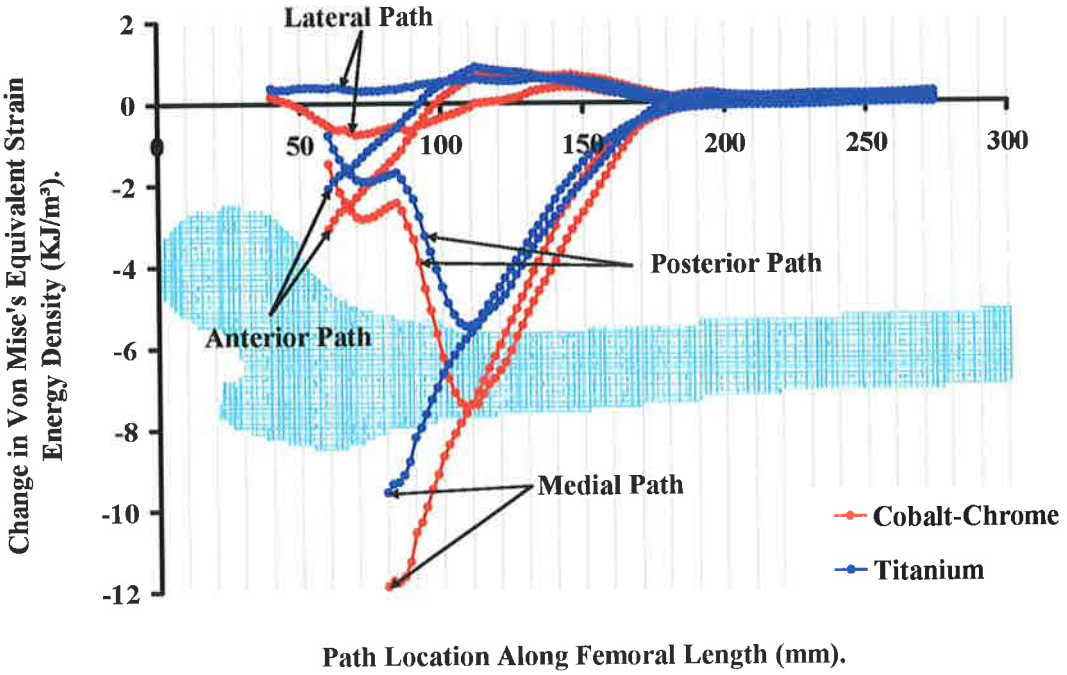


Figure 6.2: Change in Von Mise's Equivalent Strain Energy Density distribution from the intact condition along all paths for both the CoCr and titanium THA stems.

6.3.3 Discussion

This investigation has found the association between interfacial stresses and stress shielding that exists for a range of homogeneous THA stem materials within the implanted femoral model. This research is in agreement with previous studies that have advised a stiffer THA stem generates more stress shielding and less interfacial stresses than a comparable more flexible THA stem.

An association between interfacial stresses and stress shielding for a range of homogeneous THA stem materials allows consequences of homogeneous THA stem material choices to be appreciated. Minimisation of stress shielding is important and desirable within THA, however this occurs at the expense of interfacial stresses. Therefore an understanding of acceptable interfacial stresses must be obtained, as sound interfacial characteristics are paramount for

successful THA. If the importance and consequences of both interfacial stresses and stress shielding are known, then it may be possible to achieve an optimal balance between these two characteristics using a specific homogeneous THA stem stiffness to achieve maximum THA service life.

An interesting finding is that maximum Von Mise's stresses within the cement exists opposite the femoral region experiencing maximum stress shielding, which as Figure 6.2 shows, is the upper medial region of the femoral shaft. This could result directly from the selected THA stem geometry, meaning interfacial stresses could be reduced through alteration of THA stem geometry, or it may be a characteristic common to all THA stem designs.

It is clear that stress shielding of the femur can be reduced at the expense of interfacial stresses for the implanted femoral model used within this research. Different femoral and cement geometries, material and interfacial properties, and possibly more importantly loading conditions and THA stem geometry may alter the relationship between homogeneous THA stem stiffness, interfacial stresses and stress shielding within the femur. It is believed however that generally a reduction in homogeneous THA stem stiffness will reduce stress shielding within the femur at the expense of increasing interfacial stresses.

6.4 Investigation into the Optimisation of THA Stem Stiffness Distribution

As investigation into variations of homogeneous THA stem materials showed, a relationship exists between reductions in stress shielding within the femur and increases in interfacial stresses. This relationship is a limitation of the THA system. It is suggested that a non-homogeneous or distributed THA stem material stiffness may offer advantages over traditional homogeneous stiffness THA stem materials, allowing reductions in stress shielding without increasing interfacial stresses significantly.

6.4.1 Research Methodology

The numerical model used to investigate femoral response to cemented THA stems with non-homogeneous stiffness is identical to the model used to examine femoral response to cemented THA stems of differing homogenous stiffness, with the addition of THA stem segmentation allowing regular alteration of stiffness.

In an attempt to efficiently obtain the most favourable non-homogeneous THA stem stiffness distribution that generates the least stress shielding for a given allowable interfacial stress, ANSYS design optimisation analysis techniques were employed. ANSYS design optimisation produces solutions that meet all specified requirements with minimum expense of factors such as stress, volume, or any specified cost function. Within an ANSYS design optimisation analysis, Design Variables (DVs) such as dimensions or material properties are manipulated within specified ranges to produce solutions that are either feasible or infeasible depending on State Variables (SVs) such as maximum stress that also have specified ranges. An objective function, which is dependant upon problem DVs is minimised during the analysis to achieve an optimal solution.

Within this study the THA stem is sectioned into volumes that may have differing stiffness. As indicated by Figure 6.3, the THA stem has 8 divisions labelled A-H that may have differing stiffness. The Young's Modulus of each division is regarded as a DV with an allowable range spanning from a maximum of 250 GPa to a minimum of 20 GPa.

A maximum Young's Modulus of 250GPa was chosen as an upper DV limit because it exceeded the relatively high value of CoCr. A lower DV limit of 20 GPa was chosen as it is representative of healthy cortical bone. Also, specifying a minimum THA stem stiffness of at least 20 GPa eliminates the possible allocation of extreme low stiffness (<1000 MPa) within regions of THA stem, which can be thought of as structural discontinuities and an effective shortening of the THA stem. This study maintains complete and unaltered THA stem geometry, as it is believed maximising bone-cement-stem interfacial areas is favourable for achieving a robust bond.

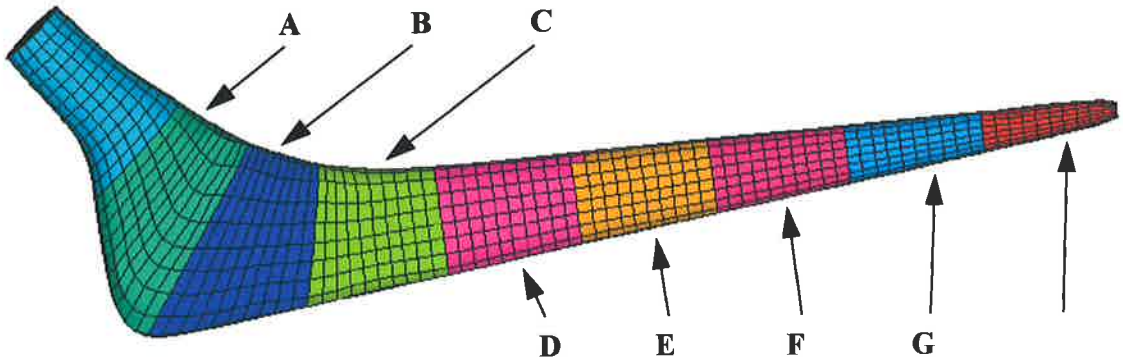


Figure 6.3: Sections within the THA stem that have different stiffness.

For the implanted femur model, both interfacial stresses and stress shielding within the bone are SVs that constrain the non-homogeneous THA stem stiffness. Interfacial stresses are treated in the same manner as the previous study of variations in homogenous THA stem stiffness, where 10 nodes at the upper medial portion of the cement volume have their resultant Von Mise's equivalent stress value summed to provide an indication of interfacial stressing, known as the maximum cement stress indicator (CSI). This CSI is used as a SV and a maximum value is specified prior to execution of the analysis. Resultant maximum interfacial stresses from the previous study of variations in homogeneous THA stem stiffness can be used as a guide for the selection of this SV.

Stress shielding of femoral bone is accounted for both with SVs and within the objective function. Simply aiming for an overall reduction in stress shielding may provide a solution with less overall stress shielding however with regions of severe stress shielding or overstressing. Previously, within the study of variations in homogenous THA stem stiffness, differences between the intact and implanted Von Mise's equivalent strain energy density were calculated at 5 equidistantly spaced points along the anterior, posterior, medial and lateral paths. These 20 differences between the intact and implanted Von Mise's equivalent strain energy density are defined as SVs, with an acceptable range. For each of these SVs the minimum value was calculated to be 2 KJ/m^3 greater stress shielding than the implanted CoCr THA stem results,

and the maximum value calculated to be 5 KJ/m^3 over-stressed than the intact solution, expressed in Equation 6.1. This was assumed to provide an acceptable solution envelope.

$$CoCr_{solution} - 2(KJ/m^3) \leq SV \leq Intact_{solution} + 5(KJ/m^3) \quad \textbf{(6.1)}$$

ANSYS design optimisation analysis endeavours to minimise an objective function, which in this instance is stress shielding. As with the SVs, the calculations had already been structured for the optimisation function as the stress shielding indicator (SSI) within the previous study of variations in homogenous THA stem stiffness. The SSI was defined as the sum of all positive differences (stress shielding) between intact and implanted Von Mise's equivalent strain energy densities calculated at each of the 5 points per path. Hence, minimising this objective function minimises overall stress shielding.

Within an ANSYS design optimisation analysis, design sets are formulated that include optimisation variables and all other model parameters. During the optimisation analysis both feasible and non-feasible solutions may be generated, with the best design set offering the minimum objective function value whilst satisfying all constraints.

The information flow process during the optimisation process can be seen in Figure 6.4. A parametrically defined analysis file is generated containing all pre-processing, solution and post-processing stages, using parameters to represent all design variables. An optimisation loop is then generated and used to build an optimisation database, which passes files through the analysis loop.

Optimisation iterations are defined as either single or multiple optimisation loops that provide a new design set. All design sets, optimisation specifications, model parameters and the current optimisation environment are contained within the optimisation database, which is separate from the ANSYS model database.

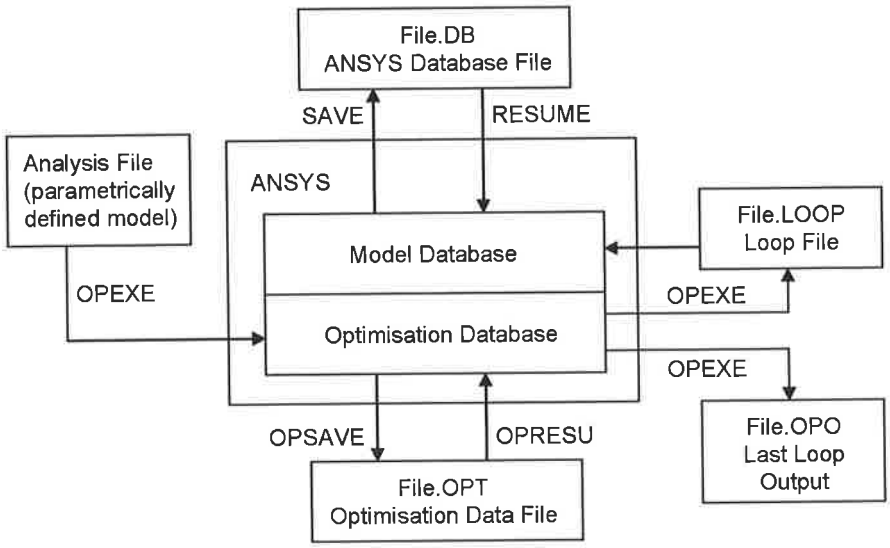


Figure 6.4: Information flow process during the ANSYS design optimisation procedure.

6.4.2 Results

The results recorded and presented for this investigation provide optimal THA stem stiffness distributions for differing maximum cement stress (SV) criteria:

- 'Analysis 1' provides an optimal THA stem stiffness distribution achieving minimal stress shielding for a maximum allowable cement stress equal to that found with a homogeneous CoCr THA stem.

- 'Analysis 2' provides an optimal THA stem stiffness distribution achieving minimal stress shielding for a maximum allowable cement stress equal to that found with a homogeneous titanium THA stem.

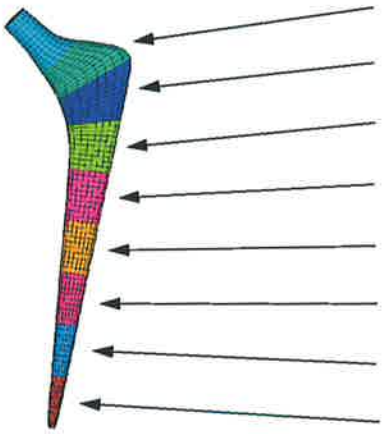
Table 6.1 presents changes in stress shielding within the upper femoral shaft (SSI) when using homogeneous THA stem stiffness distribution and optimised THA stem stiffness distribution for given maximum cement stress conditions (CSI).

Table 6.1: Changes in SSI's with constant CSI's using homogeneous and optimised THA stem stiffness distributions.

Quantity	Analysis 1	Analysis 2
Model CSI	52.56	73.36
SSI with homogeneous THA stem stiffness distribution	50.40	38.28
SSI with optimal THA stem stiffness distribution	34.90	23.88
% Improvement in SEDI when changing from homogeneous to optimised THA stem stiffness distribution	30.76%	37.62%

The magnitude of Young's Modulus within each optimised THA stem division 'Analysis 1' and 'Analysis 2' is provided in Table 6.2

Table 6.2: Distribution of Young's Modulus along THA stem length.

Position		Optimal Section Young's Modulus	
		Analysis 1	Analysis 2
	A	20.47 GPa.	20.47 GPa.
	B	20.47 GPa.	20.47 GPa.
	C	20.47 GPa.	20.47 GPa.
	D	20.47 GPa.	20.47 GPa.
	E	53.82 GPa.	20.47 GPa.
	F	249.53 GPa.	20.47 GPa.
	G	249.53 GPa.	66.96 GPa.
	H	249.53 GPa.	248.54 GPa.

To gauge the effect of the optimisation process, it is valuable to display the change in Von Mise's equivalent strain energy density that both the optimised and homogeneous THA stem stiffness distributions cause relative to the intact femoral condition. Figure 6.5 shows the change in Von Mise's equivalent strain energy density distribution within the upper femoral shaft for both a homogenous cobalt-chrome THA stem and a THA stem with optimised stiffness that causes identical maximum cement stresses found in 'Analysis 1'. Similarly, Figure 6.6 shows the change in Von Mise's equivalent strain energy density distribution within the upper femoral shaft for both a homogenous titanium THA stem and a THA stem with optimised stiffness that causes identical maximum cement stresses found in 'Analysis 2'.

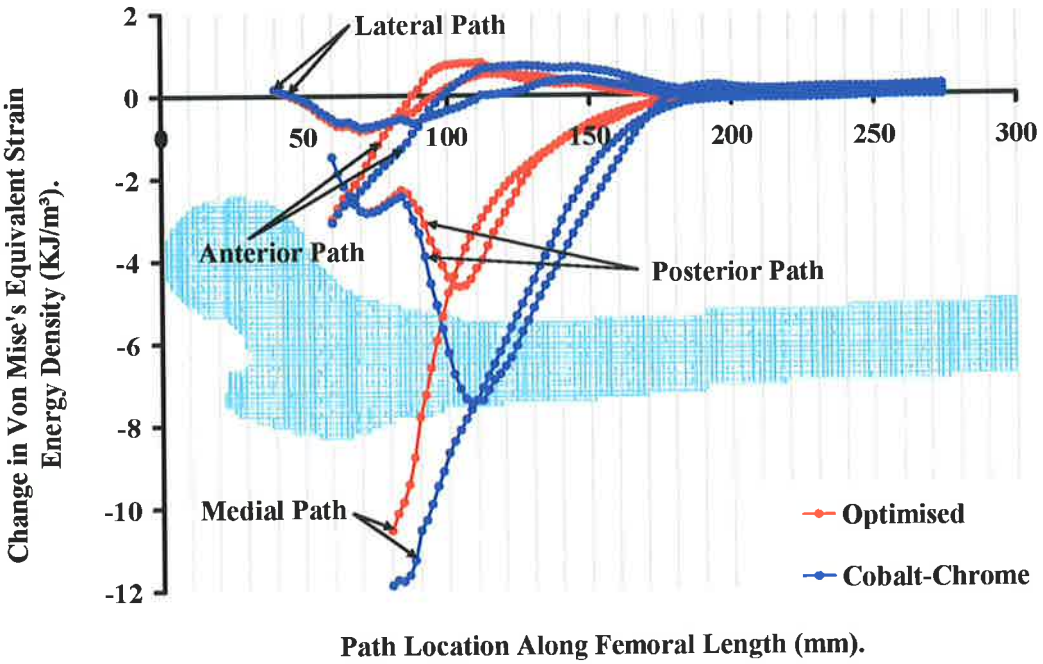


Figure 6.5: Change in Von Mise's Equivalent Strain Energy Density distribution within the upper femoral shaft from the intact condition along all paths for both a homogeneous CoCr THA stem and an optimal non-homogeneous THA stem producing a identical maximum stresses within the cement.

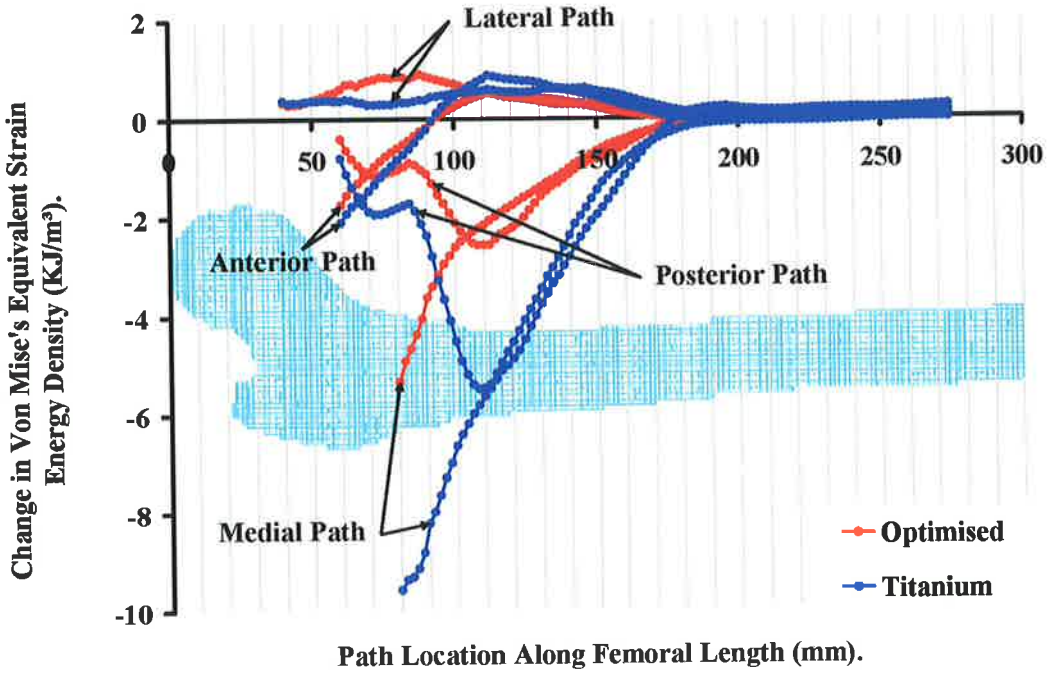


Figure 6.6: Change in Von Mise's Equivalent Strain Energy Density distribution within the upper femoral shaft from the intact condition along all paths for both a homogeneous titanium THA stem and an optimal non-homogeneous THA stem producing a identical maximum stresses within the cement.

6.4.3 Discussion

This research has found that for the specific model attributes, stress shielding within the upper femoral shaft can be significantly reduced whilst maintaining safe levels of stress within the cement through grading of the THA stem stiffness.

Essentially, in order to achieve a reduction in stress shielding within the upper femoral shaft whilst maintaining safe levels of stress within the cement, the THA stem varies from low stiffness at the top to high stiffness at the base. This is surprising, and contradictory to findings from other researchers.

For example, Kuiper & Huiskes (1997) investigated optimisation of stiffness within a cementless THA stem using a 2-dimensional numerical model aiming to minimise interface failure and limit bone resorbtion. However the optimal stem was found to have a relatively stiff proximal end, with stiffness decreasing towards the distal end. Kuiper & Huiskes (1997) suggested that their results were similar to the 2-dimensional optimisation results obtained by Huiskes & Boelagen (1989), where reductions in stem stiffness were equivalent to tapering stem geometry. The 3-dimensional numerical model developed within this research is significantly more detailed and advanced, and considers many aspects omitted by Kuiper & Huiskes (1997) and Huiskes & Boelagen (1989).

As found previously in Figure 6.1, a relationship exists between cement stresses and femoral stress shielding. This relationship demonstrated that reducing homogeneous THA stems stiffness increases stresses within the cement whilst reducing stress shielding. This finding provides insight into the results obtained relating to THA stems with distributed stiffness. The low stiffness in the upper and middle regions of the THA stem is attributed to the requirement for minimisation of stress shielding within the upper femoral shaft - which was the optimisation goal. As previously suggested, the low THA stem stiffness allows the bone and THA stem to flex together as one unit, reducing the quantities of bone that are shielded from loading by comparion to that associated with stiff THA stems.

The lower stiff portion of the THA stems with optimised stiffness distribution is a result of the need to control maximum cement stressing. Again, as indicated in Figure 6.1, minimal cement stressing is associated with stiff homogeneous THA stem stiffness. From the investigation of THA stems with distributed stiffness, 'Analysis 1' and 'Analysis 2' reveal that increasing the stiffness of the lower THA stem regions decreases the maximum level of stress within the cement. Hence, the maximum cement stress condition is responsible for the increased stiffness at the lower regions of the THA stem.

It is believed that increasing the stiffness in the lower portion of the THA stem controls the magnitude of deflection at the top of the THA stem through reducing the flexible length. The lower stiff portion of the THA stem resists elastic deformation more that the upper portions, and so less deflection occurs at the top of the THA stem (where maximum cement stress occurs) than occurs within a homogeneous low stiffness THA stem. Limiting the deflection of the upper THA stem within the cement and upper femoral shaft controls the level of maximum stress within the cement. A THA stem with flexible upper region and rigid lower region has less upper THA stem deflection and associated maximum cement stress than a THA stem that is homogeneously flexible.

Cross-sectional stem geometry has significant influence over optimal THA stiffness. This research has investigated altering material stiffness and not THA stem cross sectional profile (due to time constraints) to modify the overall THA stem bending stiffness, although both factors are equally influential. The results generated within this research show the Young's Modulus within the lower portion of the THA stem increasing rapidly to avoid large interfacial stresses; however within these regions of the chosen THA stem geometry the cross-sectional area (and second moment of inertia) also decreases rapidly, albeit constantly. Analysis of a THA stem geometry that does not taper as much as the CPT stem towards the distal end would provide insight into this, and associated changes in interfacial stressing.

Although increasing the stiffness within the lower portion of the THA stem decreases maximum cement stresses, it increases stress shielding within the upper femur somewhat. This increase in stress shielding is balanced with the reduction in maximum cement stresses. Figure 6.5 and Figure 6.6 show the profile of the stress shielding generated by THA stems with homogeneous and optimally distributed stiffness. Interestingly, stress shielding within the femoral shaft surrounding the stiff portions of THA stems with optimally distributed stiffness is not significant. The bulk of the stress shielding occurs within the upper medial regions of the femoral shaft.

Figure 6.5 and Figure 6.6 show the value of an optimally distributed THA stem stiffness. Stress shielding is significantly reduced in the upper medial and posterior regions of the femoral shaft. Regions of the upper lateral and anterior femoral shaft experience over-stressing relative to the natural intact condition, although importantly this overstressing is not excessive or cause for concern. The THA stem with an optimally distributed stiffness is generally a more satisfactory alternative to the THA stem with homogeneous stiffness causing similar maximum stresses within the cement.

This research has successfully found the distribution of stiffness within the given THA stem geometry that results in minimal stress shielding for a maximum cement stress. Table 6.1 shows the actual values of the stiffness within the discretised THA stem. Although the descretisation of the THA stem is somewhat coarse, refinement would generate more design variables and corresponding increased solution time. If increased resolution is required, many of the sections within the upper regions of the THA stem could have their stiffness values fixed and sections within lower regions may have their sections further divided, providing increased solution accuracy at the transition from low to high stiffness. Unfortunately, time constraints did not allow this.

The distributed THA stem stiffness computed during this research can be considered a sectional stiffness. The grading of THA stem sectional stiffness could be achieved using a number of methods. The THA stem could be manufactured using a 'functionally graded material' where there is spatial variation in material composition or structure that provides a change in characteristics such as stiffness and density. An example of this is foamed titanium alloy with porosity variation. Alternatively, the THA stem could be hollowed, with the internal void geometry controlling the effective sectional stiffness. Manufacturing the THA stem with distributed sectional stiffness is the focus of other researchers, and is not included within this research.

Results obtained for the THA stems with optimally distributed stiffness indicate major reductions in stress shielding primarily in the posterior and medial regions of the upper femoral shaft. It is believed that major reductions in stress shielding occurred in these locations given that most stress shielding caused by the THA stem are exhibited in these positions. Reducing the highest values of stress shielding within the upper femoral shaft is a characteristic of the optimisation technique.

Whilst developing the optimisation analysis, all parameters were manually altered to gain an understanding of the specific variables influence on solution trends. The final parameter definitions reflect a robust response to issues uncovered during this process. Within the optimisation variable definitions there is an opportunity to input a tolerance. These tolerances are small (>2%) and are evident in sectional stiffness solutions such as 20.47 GPa, that could be interpreted as 20 GPa which was the minimum value.

The results generated from this research are relevant to the specific model parameters employed, including load condition, THA stem, cement and femoral geometries and material characteristics. With further refinement and investigation of other loading regimes and THA stem geometries, it may be possible to predict stress shielding and interfacial stressing characteristics of other THA stem designs. It is expected that for the same geometries and material characteristics, other loading regimes that transfer a primarily compressive load along the length of the femur will produce an optimally distributed THA stem stiffness similar to the one found within this study, however the degree of distribution may vary accordingly.

THA stem geometry is an important factor within this research. As previously discovered within this research, maximum cement stresses and stress shielding within the femur occur in the upper medial region. It is possible that reductions in cement stresses at this location could be achieved through design of a superior THA stem geometry that spreads loading more evenly, meaning that when assigned an optimally distributed stiffness major reductions in stress shielding could be achieved whilst not exceeding the limitations of the cement.

Cement stresses are the limitation faced when striving to reduce stress shielding. It has been proven that significant reductions in stress shielding can be achieved without major overstressing of the femur; however complete understanding of the mechanical behaviour of the cement is required. As presented in Figure 6.1, even for a THA stem with homogeneous stiffness distribution, if the cement can reliably withstand double the stresses encountered with a CoCr stem, then the stress shielding within the upper femoral shaft can roughly be halved. If a THA stem with optimally graded stiffness is employed, then stress shielding may be reduced by more than a further 30% going by the resultant trend found within this research.

6.4.4 Conclusion

This research has found that considerable reductions in stress shielding within the upper femoral shaft can be achieved for a maximum allowable stress within the cement through the use of a THA stem with distributed stiffness. For the specific model characteristics used within this investigation, the THA stem with optimally distributed stiffness exhibited a flexible upper section and rigid lower section.

This numerical optimisation process has the potential to significantly increase THA stem service life. Implementing this process within the THA stem design phase would be highly advantageous, as once improvements to THA stem geometry and cement mechanics are accomplished, this process will ensure optimal service life and value to society.

Chapter 7

SUMMARY AND CONCLUSIONS

A preliminary numerical modelling investigation of the intact femoral system was conducted to unearth potential problems (such as poor geometry and required mesh density) without investing major expense, and to gain general understanding of the natural femoral system. This preliminary investigation used femoral geometry sourced from the 'Standardised Femur Program' (Viceconti et al., 1996) and was then modified, although the absence of realistic material property definition and over-simplified geometry limited its value for the purpose of this research. The need to employ a model constructed form CT scan images was established, and an intact left femoral model was sourced from the 'VAKHUM' project (Van Sint Jan, 2002). This model provided detailed material stiffness distribution (based on bone density) and more authentic geometry. The model sourced from the 'VAKHUM' project (Van Sint Jan, 2002) was developed to assess efficiency of, and sensitivity to, loading and restraint conditions. Interestingly, it was confirmed that if results within upper femoral regions (where stress shielding occurs) are of primary interest then only the upper half of the femur need be modelled, with a fully fixed restraint at the distal end sufficing.

Traditionally, modelling femoral loading is often rudimentary. Investigation into the selection of load-step has established that the 45% gait phase (often referred to as toe-off) produced maximum stressing of the femur, and is therefore important when engineering sufficient implant strength. Within this load-step a refined selection of muscular loads were established that significantly reduce computational expense without compromising solution accuracy. Analysis also showed that muscular loading distributed over anatomical attachment areas

eliminated localised and unrealistic regions of overstressing associated with simplistic point loading.

Unfortunately the femoral geometry sourced from the 'VAKHUM' project (Van Sint Jan, 2002) was assessed by an orthopaedic surgeon to suffer from a congenital deformity rendering it inappropriate for use within an implanted femoral study. Although disappointing, much knowledge was gained about requirements for efficient modelling. This disappointment drove the need for a cadaveric specimen-based model with normal healthy geometry, utilising all loading and restraint conditions previously defined. This exercise was thorough, modelling both the left and the right intact and later implanted femora from the same cadaveric donor. This process assessed the effectiveness of differing implant geometry and surface finish, the results of which showed a superior stress shielding outcome associated with a smooth, tapered implant. Although the iterative contact analysis required for modelling the smooth implant surface condition was successful, it was believed to be too time consuming for use within an optimisation analysis. Consequently, the tapered implant with rough surface finish was selected to provide a sound basis for optimisation analysis.

Prior to optimisation analysis, the model's relationship between homogeneous THA stem stiffness, maximum cement stress and stress shielding was ascertained. This exercise revealed that as homogeneous stiffness decreased the stress shielding decreased, however the limiting interfacial stresses (within the cement) increased. This provided a baseline for assessing improvements gained through optimisation.

ANSYS design optimisation was employed to reduce stress shielding as much as possible without increasing interfacial stresses by altering the implants stiffness along its length. Results found that the optimally distributed implant stiffness was able to provide more than a 30% reduction in stress shielding without exceeding the interfacial stress level associated with an identical implant with homogeneous stiffness.

For the THA stem geometry used within this analysis, the optimal stiffness increased in magnitude along the length of the implant from top to bottom. Although this was unexpected and not consistent with previous more rudimentary attempts at implant design with optimum stiffness, it is clear that the specific stiffness distribution is dependant on the implant geometry, here modelled on the 'CPT Hip Prosthesis' (marketed by Zimmer, Inc. Warsaw, Indiana, USA), and also the method of implantation, here a cemented implantation which has the constraint of cement stress levels. This demonstrates the importance of the inclusion of this optimisation analysis during the initial design phases of implant geometry.

The findings of this research indicate a significant reduction in stress shielding by optimally distributing the implant elastic stiffness. The design methods developed in the course of this work can be applied to other implant systems and when used in combination with appropriate engineering materials will be the basis for improved implants.

The benefits of these findings cannot be understated; a patient with a considerably extended THA service life may avoid the cost and pain of revision surgery, enjoying prolonged post-operative functional capacity than the current technology can offer. Indeed, the benefits are not confined to the recipients of the implants. The health system, and therefore wider society, can also be a cost beneficiary due to the reduction of care required for patients with decreased mobility and those requiring the revision surgery.

Chapter 8

FUTURE WORK

The work completed within this research provides a sound foundation for future investigation of intact and implanted numerical femoral modelling and implant optimisation techniques.

Although the optimisation analysis was performed on a cemented THA stem with tapering geometry, generating optimal stiffness distributions for other THA stems with varied geometry would be both useful and interesting (particularly one with minimal tapering). Further, investigation of cementless THA stems using this optimisation analysis with an interfacial bone-THA stem stress rather than a maximum cement stress acting as a State Variable would be informative and valuable.

It may be beneficial to apply differing load regimes to the implanted femoral model with optimal THA stem stiffness distribution to analyse stress shielding performance relative to the standard THA stem stiffness distribution. This may provide more insight into the influence of load regime choice within optimisation analysis (although for safety reasons the THA stem must be designed to withstand maximum loading) and corresponding over-engineering under lesser loads.

The numerical implant optimisation technique developed within this research could be applied to other implants such as those employed in knee replacement surgery. Although implant, anatomical geometry and loading differ from THA conditions, the process can be applied to reduce implant stress shielding and consequently increase service life.

Above all, it is believed that employing this optimisation procedure within the initial implant design stages would provide the greatest benefit. Eventually it will be possible to design a THA stem for an individual that not only exhibited optimal geometry (allowing implantation without excessive material removal) but also contained optimal stiffness distribution.

Glossary

Abductors	The adductors are muscles on the outside of the femur that move the leg away from the midline of the body.
Acetabulum	The hollow, cuplike portion of the pelvis into which the head of the femur fits.
Adductors	The adductors are muscles on the inside of the femur that pull the leg across the centreline of the body.
Anatomical	Referring to anatomy or to the structure of the organism.
Anterior	Toward the front or in front of.
Arthritis	An inflammatory condition that affects joints.
Arthroplasty	The surgical repair of a joint.
Aseptic Loosening	Implant loosening, can be the result of numerous causes.
Bone Landmarks	Locations on bones that are recognisable and common to all individuals.
Cancellous Bone	Bone consisting of mineralised regularly ordered parallel collagen fibres found in the end of long bones.
Collagen	The protein substance in the white fibres of skin, tendon, bone, cartilage and all other connective tissue.
Compact Bone	The compact, non-cancellous, dense portion of bone.
Computer Tomography	A special radiographic technique that uses a computer to assimilate multiple X-ray images into a 2 dimensional cross-sectional image.
Congenital Deformities	A deformity from birth.
Cortex	The cortex of a bone is the dense outer shell that provides strength.
Cortical Bone	See compact bone.
Dislocations	The displacement of any part, more especially of a bone.
Disphyseal	Shaft like region.

Distal	Remote, farther from any point of reference, opposed to proximal.
Femoral Head	The ball like structure located at the top part of the femur.
Femoral Shaft	Long, tubular section of the femur bone.
Femur	The large bone in the thigh that articulates with the pelvis above and the knee below.
Fractures	Breaks in bones or cartilage.
Gastrocnemi	Muscles originating from the femur allowing flexion of the foot.
Hard Bone	See compact bone.
Hydroxyapatite	A calcium phosphate mineral, and component of bone.
Ilio-Tibial Band	A group of muscles that keep the knee extended during upright posture.
Infection	Invasion and multiplication of micro-organisms in body tissues.
Intramedullary Canal	Void within the upper femur.
Lateral	Denoting a position farther from the median plane or midline of the body or of a structure.
Lesser Trochanter	Location on the femur where the psoas major muscle originates.
Ligaments	Bands of fibrous tissue connecting bones and cartilage, serving to support and strengthen joints.
Medial	The side of the body or body part that is nearer to the middle or centre (median) of the body.
Osseointergration	The long-term intimate relationship of ordered living bone fusing to the surface of a load bearing implant.
Osteoporosis	A reduction in the amount of bone mass, leading to fractures after minimal trauma.
Posterior	Situated in back of or in the back part of or affecting the back or dorsal surface of the body.
Pressure Necrosis	Cell damage or death caused by rubbing, scratching and pressure.

Prosthetic	Artificial implant, as in an artificial organ or limb.
Proximal	Nearest to, closer to any point of reference, opposed to distal.
Revision Surgery	Revision surgery is the salvage surgery of previous surgery.
Tendons	A fibrous, strong, connective tissue that connects muscle to bone.
Trabeculae	Individual fibre structures that create cancellous bone.
Trunion	Part of an implant that replicated the femoral head.
Vastii	The vastii muscle group consists of four individual muscles, and are used to extend the leg.

References

ANSYS V5.7.1, 2002. <http://www.ansys.com>.

Ashby, M.F. and Gibson, L.J., 1988. "Cellular solids: structure & properties." Pergamon Press, New York.

Ashby, M.F. and Gibson, L.J., 1997. "Cellular solids: structure & properties." Cambridge University Press, New York.

Automation Creations, Inc. "MatWeb: The Online Materials Information Reference." Available from World Wide Web: <www.matweb.com>, Accessed 8th July 2002.

Baker, D.S., Wang, A.W., Yeo, M.F., Nawana, N.S., Brumby, S.A., Pearcy, M.J. and Howie, D.W., 1999. "The skeletal response to matt and polished cemented femoral stems." Journal of Joint and Bone Surgery, 82-B: 1182-1188.

Baleani, M., Cristofolini, L. and Viceconti, M., 1999. "Endurance testing of hip prostheses: A comparison between the load fixed in ISO 7206 standard and the physiological loads." Clinical Biomechanics, 14(5): 339-345.

Baleani, M., Viceconti, M., Muccini, R. and Ansaloni, M., 2000. "Endurance verification of custom-made hip prostheses." International Journal of Fatigue, 22(10): 865-871.

Barbour, P.S.M., Barton, D.C. and Fisher, J., 1995. "The influence of contact stress on the wear of UHMWPE for total replacement hip prostheses." Wear, 181-183(1): 250-257.

Beaupre, G.S. and Hayes, W.C., 1985. "Finite element analysis of a three-dimensional open-celled model for trabecular bone." Journal of Biomechanical Engineering, 107(3): 249-256.

Bedzinski, R. and Bernakiewicz, M., 1998. "Experimental and numerical investigations in a femur with hip endoprosthesis." Journal of Biomechanics, 31(1): 90.

Bergmann, G., Deuretzbacher, G., Heller, M., Graichen, F., Rohlmann, A., Strauss, J. and Duda, G. N., 2001. "Hip contact forces and gait patterns from routine activities." Journal of Biomechanics, 34(7): 859-871.

Callaghan, J.J., Hip Society (U.S.) and Knee Society (U.S.) (Editors), 1995. "Orthopaedic knowledge update. Hip and knee reconstruction / edited by John J. Callaghan et al.; developed by the Hip Society and the Knee Society." American Academy of Orthopaedic Surgeons, Rosemont.

Carter, D.R. and Hayes, W.C., 1976. "Bone compressive strength: the influence of density and strain rate." Science, 194(4270): 1174-1176.

Chang, P.B., Mann, K.A. and Bartel, D.L., 1998. "Cemented femoral stem performance. Effects of proximal bonding, geometry, and neck length." Clinical Orthopaedics, 355: 57-69.

Cheal, E.J., Spector, M. and Hayes, W.C., 1992. "Role of loads and prosthesis material properties on the mechanics of the proximal femur after total hip arthroplasty." Journal of Orthopaedic Research, 10: 405-422.

Choi, K. and Goldstien, S.A., 1992. "A comparison of the fatigue behaviour of human trabecular and cortical bone tissue." Journal of Biomechanics, 25: 1371-1381.

Collis, D.K., Mohler, C.G., 1998. "Loosening rates and bone lysis with rough finished and polished stems." Clinical Orthopaedics and Related Research, 355: 113-122.

Corwin, S.C., 1997. "Fabric and elastic principal directions of cancellous bone are closely related." Journal of Biomechanics, 30(11): 1191-1192.

Crowninshield, R.D., Brand, R.A., Johnston, R.C. and Milroy, J.C., 1980. "An analysis of femoral component stem design in total hip arthroplasty." Journal of Bone and Joint Surgery, 62(1): 68-78.

Cunningham, D. J. and Romanes, G. J., 1986. "Cunningham's manual of practical anatomy." Oxford University Press, New York.

Duda, G.N., Brand, D., Freitag, S., Lierse, W. and Schneider, E., 1996. "Variability of femoral muscle attachments." Journal of Biomechanics, 29(9): 1185-1190.

Duda, G.N., Heller, M., Albinger, J., Schulz, O., Schneider, E. and Claes, L., 1998. "Influence of muscle forces on femoral strain distribution." Journal of Biomechanics, 31(9): 841-846.

Duda, G.N., Schneider, E. and Chao, E. Y. S., 1997. "Internal forces and moments in the femur during walking." Journal of Biomechanics, 30(9): 933-941.

El-Sheikh, H.F., Macdonald, B.J. and Hashmi, M.S.J., 2002. "Material Selections in the Design of the Femoral Components of Cemented Total Hip Replacement." Journal of Materials Processing Technology, 122(1-2): 309-317.

Goto, T., Sasaki, N. and Hikichi, K., 1999. "Early stage-stress relaxation in compact bone." Journal of Biomechanics, 32(1): 93-97.

Gross, S. and Abel, E.W., 2001. "A finite element analysis of hollow stemmed hip prostheses as a means of reducing stress shielding of the femur." Journal of Biomechanics, 34(8): 995-1003.

Harris, W.H., 1992. "Is it advantageous to strengthen the cement-metal interface and use a collar for cemented femoral components of total hip replacements?" Clinical Orthopaedics and Related Research, 285: 67-72.

Heller, M., Duda, G. and Claes, L., 1998. "Femoral strain distribution under complex thigh muscle loading during gait." Journal of Biomechanics, 31(1): 147.

Heller, M.O., Bergmann, G., Deuretzbacher, G., Dürselen, L., Pohl, M., Claes, L., Haas, N. P. and Duda, G. N., 2001. "Musculo-skeletal loading conditions at the hip during walking and stair climbing." Journal of Biomechanics, 34(7): 883-893.

Hinrichs, F., Kuhl, M., Kuhl, M. and Griss, P., 2003. "A comparative clinical outcome evaluation of smooth (10-13 year results) versus rough surface finish (5-8 year results) in an otherwise identically designed cemented titanium alloy stem." Archives of Orthopaedic and Trauma Surgery, 123: 268-272.

Howie, D.W., Middleton, R.G., Costi, K., 1998. "Loosening of matt and polished cemented femoral stems." Journal of Joint and Bone Surgery, 80-B: 573-576.

Hozack, W.J., Rothman, R.H., Booth, R.E., Balderston, R.A., 1993. "Cemented versus cementless total hip arthroplasty." Clinical Orthopaedics and Related Research, 289: 161-165.

Huiskes, R. and Boeklagen, R., 1989. "Mathematical shape optimization of hip prosthesis design." Journal of Biomechanics, 22(8/9): 793-804.

Jacobs, C. R., Davis, B. R., Rieger, C. J., Francis, J. J., Saad, M. and Fyhrie, D. P., 1999. "The impact of boundary conditions and mesh size on the accuracy of cancellous bone tissue modulus determination using large-scale finite-element modeling." Journal of Biomechanics, 32(11): 1159-1164.

Joshi, M.G., Advani, S.G., Miller, F. and Santare, M.H., 2000. "Analysis of a femoral hip prosthesis designed to reduce stress shielding." Journal of Biomechanics, 33(12): 1655-1662.

Katoozian, H. and Davy, D.T., 2000. "Effects of loading conditions and objective function on three-dimensional shape optimization of femoral components of hip endoprostheses." Medical Engineering & Physics, 22(4): 243-251.

Kaneps, A.J., Stover, S.M. and Lane, N.E., 1997. "Changes in canine cortical and cancellous bone mechanical properties following immobilization and remobilization with exercise." Bone, 21(5): 419-423.

Kuiper, J.H. and Huiskes, R., 1997. "Mathematical optimization of elastic properties: application to cementless hip stem design." Journal of Biomechnical Engineering, 119(2): 166-174.

Lengsfeld, M., Kaminsky, J., Merz, B. and Franke, R.P., 1996. "Sensitivity of femoral strain pattern analyses to resultant and muscle forces at the hip joint." Medical Engineering & Physics, 18(1): 70-78.

Ling, R.S., 1992. "The use of a collar and precoating on cemented femoral stems is unnecessary and detrimental." Clinical Orthopaedics and Related Research, 285: 73-83.

Markov, I.A., Derkach, G.M., Belykh, S.I., Sherepo, K.M. and Gavrushenko, N.S., 1998. "Cementless versus cement fixation (with cyanacrylate) of implants in animal experiment." Journal of Biomechanics, 31: 97.

Mayo Foundation for Education and Research, Available from World Wide Web: <http:// www.mayoclinic.com/health/hip-replacement/ AR00028>, Accessed 2nd December 2005.

Mburu, G., Hutchison, J.D. and Aspden, R.M., 1998. "Cement fixation of the acetabular component during total hip replacement." Journal of Biomechanics, 31(1): 50.

McNamara, B.P., Cristofolini, L., Toni, A. and Taylor, D., 1997. "Relationship between bone-prosthesis bonding and load transfer in total hip reconstruction." Journal of Biomechanics, 30(6): 621-630.

Morgan, E.F. and Keaveny, T.M., 2001. "Dependence of yield strain of human trabecular bone on anatomic site." Journal of Biomechanics, 34(5): 569-577.

Munting, E. and Verhelpen, M., 1995. "Fixation and effect on bone strain pattern of a stemless hip prosthesis." Journal of Biomechanics, 28(8): 949-961.

Niinimäki, T., Puranen, J. and Jalovaara, P., 1994. "Total hip arthroplasty using isoelastic femoral stems. A seven- to nine-year follow-up in 108 patients." Journal of Bone and Joint Surgery, 76: 413- 418.

Norman, T.L., Thyagarajan, G., Saligrama, V.C., Gruen, T.A. and Blaha, J.D., 2001, "Stem surface roughness alters creep induced subsidence and 'taper-lock' in cemented femoral hip prosthesis." Journal of Biomechanics, 34: 1325-1333.

Nuño, N. and Avanzolini, G., 2002. "Residual stresses at the stem-cement interface of an idealized cemented hip stem." Journal of Biomechanics, 35: 849-852.

O'Toole III, R.V., Jaramaz, B., DiGioia III, A.M., Visnic, C.D. and Reid, R.H., 1995. "Biomechanics for preoperative planning and surgical simulations in orthopaedics." Computers in Biology and Medicine, 25(2): 183-191.

Paul, J.P., 1999. "Strength requirements for internal and external prostheses." Journal of

Biomechanics, 32(4): 381-393.

Pawlikowski, M., Skalski, K. and Haraburda, M., 2003. "Process of hip joint prosthesis design including bone remodelling phenomenon." Computers and Structures, 81: 887-893.

Rahman, A., 2000. "Shape Optimization and Material Evaluation of the Hip Prosthesis." Ninth International ANSYS Conference, Pittsburgh, PA.

Rhinoceros V1.1, 2000. <http://www.rhino3d.com>.

Schaldach, M. and Hohmann, D., 1976. "Advances in artificial hip and knee joint technology / edited by M. Schaldach and D. Hohmann, in collaboration with R. Thull and F. Hein." Springer-Verlag, Berlin.

Simões, J.A., Marques, A.T. and Jeronimidis, G., 2000. "Design of a controlled-stiffness composite proximal femoral prosthesis." Composites Science and Technology, 60(4): 559-567.

Sledge, C.B., (Editor) 1998. 'The hip." Lippincott-Raven Publishers, Philadelphia.

Smith & Nephew website, Available from World Wide Web: <http://www.smith-nephew.com> Accessed 1st June 2003.

Solid Edge V9, 2000. <http://www.solidedge.com>.

Speirs, A.D., Slomczykowski, M.A., Orr, T.E., Siebenrock, K. and Nolte, L.P., 2000. "Three dimensional measurement of cemented femoral stem stability: an in vitro cadaver study." Clinical Biomechanics, 15: 248-255.

Stryker, 1999, "Product Overview Brochure." Available from World Wide Web: <http:// www.strykercorp.com> Accessed 12th December 2001.

Stulpner, M.A., Reddy, B.D., Starke, G.R. and Spirakis, A., 1997. "A three-dimensional finite analysis of adaptive remodelling in the proximal femur." Journal of Biomechanics, 30(10): 1063-1066.

Stolk, J., Verdonschot, N. and Huiskes, R., 1998. "Sensitivity of failure criteria of cemented total hip replacements to finite element mesh density." 11th Conference of ESB, Toulouse, France, pp. 165.

Stolk, J., Verdonschot, N. and Huiskes, R., 2001. "Hip-joint and abductor-muscle forces adequately represent in vivo loading of a cemented total hip reconstruction." Journal of Biomechanics, 34(7): 917-926.

Taylor, M.E., Tanner, K.E., Freeman, M.A.R. and Yettram, A.L., 1996. "Stress and strain distribution within the intact femur: Compression or bending?" Medical Engineering & Physics, 18(2): 122-131.

Trick, L.W., 2001. "The Total Guide to Total Primary Hips" Orthopaedic Special Edition, 7: 49-68.

Van Rietbergen, B., Muller, R., Ulrich, D., Ruegsegger, P. and Huiskes, R., 1999. "Tissue stresses and strain in trabeculae of a canine proximal femur can be quantified from computer reconstructions." Journal of Biomechanics, 32(2): 165-173.

Van Sint Jan, 2002. "The VAKHUM Project - Virtual Animation of the Kinematics of the Human." Available from World Wide Web: <http://www.vakhum.com>.

Verdonschot, N., Tanck, E., Huiskes, R., 1998, "Effects of prosthesis surface roughness on the failure process of cemented hip implants after stem-cement debonding." Journal of Biomedical Materials Research, 42-4: 554-559.

Verdonschot, N., Huiskes, R., 1997. "The effects of cement-stem debonding in THA on the long-term failure probability of cement." Journal of Biomechanics, 30: 795-802.

Viceconti, M., Casali, M., Massari, B., Cristofolini, L., Bassini, S. and Toni, A., 1996. "The 'Standardized Femur Program' proposal for a reference geometry to be used for the creation of finite element models of the femur." Journal of Biomechanics, 29(9): 1241.

Viceconti, M., Muccini, R., Bernakiewicz, M., Baleani, M. and Cristofolini, L., 2000. "Large-sliding contact elements accurately predict levels of bone-implant micromotion relevant to

osseointegration." Journal of Biomechanics, 33(12): 1611-1618.

Weinans, H., Sumner, D., Igloria, R. and Natarajan, R. N., 2000. "Sensitivity of periprosthetic stress-shielding to load and the bone density-modulus relationship in subject-specific finite element models." Journal of Biomechanics, 33(7): 809-817.

Wirtz, D.C., Schiffers, N., Pandorf, T., Radermacher, K., Weichert, D. and Forst, R., 2000. "Critical evaluation of known bone material properties to realize anisotropic FE-simulation of the proximal femur." Journal of Biomechanics, 33(10): 1325-1330.

Wolff, J., 1836-1902, 1986. "The law of bone remodelling / Julius Wolff; translated by P.G.J. Maquet and R. Furlong." Springer-Verlag, Berlin.

Yoon, Y.S., Jang, G.H. and Kim, Y.Y., 1989. "Shape optimal design of the stem of a cemented hip prosthesis to minimize stress concentration in the cement layer." Journal of Biomechanics, 22(11-12): 1279-1284.

Appendix A

Data & Figures

Table A.1: Mechanical properties of 'wet' compact human and bovine bone (Ashby et al., 1997).

Mechanical Property	Human	Bovine
Density, ρ_s (kg/m^3).	1800 - 2000	2060
Young's Modulus, E (GPa).		
Longitudinal	17	22.6
Radial	11.5	10.2
Tangential	11.5	10.2
Shear Modulus, G (GPa).		
Longitudinal-Radial (LR)	3.3	3.6
Longitudinal-Tangential (LT)	3.3	3.6
Radial-Tangential (RT)	-	-
Poisson's Ratio, υ_s.		
$\upsilon_{s\,(LR)}$	-	0.36
$\upsilon_{s\,(LT)}$	0.41	0.36
$\upsilon_{s\,(RT)}$	0.41	0.51
Compressive Strength, σ_{yC} (MPa).		
Axial	193	254
Normal	133	146
Tensile Yield Strength, σ_{yT} (MPa).		
Axial	148	144
Normal	49	46
Toughness, G_{CS} (J/m^2).		
Axial	-	1690
Normal	-	4330
Fracture Toughness, K_{ICs} (MN/m$^{3/2}$).		
Axial	-	3.5
Normal	-	6.1

Table A.2: Muscular loading magnitudes and directions developed by Cheal et al. (1992), and modified by Duda et al. (1998) to give a more accurate four-phase gait cycle.

Name of force	Attachment [mm]			Force at 10% gait cycle [N]			Force at 30% gait cycle [N]			Force at 45% gait cycle [N]			Force at 70% gait cycle [N]		
	x	y	z	x	y	z	x	y	z	x	y	z	x	y	z
Joint contact hip	-7.93	-56.60	433.42	-510.63	665.76	-1131.89	-399.59	812.50	-1435.34	-466.34	962.62	-1911.22	-68.12	4.94	-47.79
Joint contact patella	27.71	-10.70	13.40	-123.18	65.61	-27.03	-14.32	2.73	5.42	-342.94	-34.41	164.95	-15.95	-8.09	30.49
Joint contact knee :															
posterio-lateral1	-5.12	20.99	0.03	0.00	0.00	718.30	0.00	0.00	807.00	0.00	0.00	1287.38	0.00	0.00	-22.08
anterio-medial1	2.85	-20.04	-0.14	0.00	0.00	239.43	0.00	0.00	269.00	0.00	0.00	429.13	0.00	0.00	-7.36
central	0.00	0.00	0.00	-99.66	60.75	-0.01	-98.36	108.58	-0.01	-134.61	113.43	-0.02	-14.49	-34.95	-0.01
posterio-lateral2	2.67	24.96	-0.53	-339.36	0.00	0.00	-280.31	0.00	0.00	-137.02	0.00	0.00	-22.84	0.00	0.00
anterio-medial2	2.89	-29.98	-0.29	476.24	0.00	0.00	475.18	0.00	0.00	797.97	0.00	0.00	56.00	0.00	0.00
posterio-medial	-13.16	-16.08	-0.97	0.00	-339.36	0.00	0.00	-280.31	0.00	0.00	-137.02	0.00	0.00	25.71	0.00
anterio-lateral	24.92	12.84	1.58	0.00	110.34	0.00	0.00	-19.90	0.00	0.00	-119.14	0.00	0.00	22.84	0.00
Gluteus maximus 1	-5.72	10.25	407.51	71.13	-71.72	75.19	50.18	-87.92	90.85	35.10	-87.87	90.95	0.00	0.00	0.00
Gluteus maximus 2	-13.13	2.57	349.89	27.33	-58.78	75.97	10.05	-69.16	85.76	0.08	-57.73	70.32	0.20	-0.45	0.55
Gluteus maximus 3	-11.63	10.88	392.17	36.06	-12.13	-27.76	0.00	0.00	0.00	0.00	0.00	0.00	0.00	0.00	0.00
Gluteus medius 1, 2, 3	-4.53	8.61	410.56	161.10	-118.59	149.10	128.07	-164.71	201.36	111.23	-179.68	221.40	3.57	-4.89	5.53
Gluteus minimus 1, 2, 3	0.00	0.00	413.68	136.50	-92.37	36.25	152.51	-177.49	78.50	186.22	-193.69	92.98	22.29	28.45	7.97
Tensor fasciae latae	6.34	15.38	393.23	3.23	-51.09	-18.95	35.26	-20.26	-26.34	51.42	-40.70	-40.04	6.43	-3.00	-5.58
Piriformis	1.70	-7.48	413.66	22.71	-47.98	42.95	15.17	-77.90	68.03	5.35	-77.90	67.03	2.89	-6.42	5.44
Obturator externus	-5.70	-11.09	407.19	0.00	0.00	0.00	0.00	0.00	0.00	0.00	0.00	0.00	0.55	-0.41	0.07
Quadratus femoris	-17.75	-29.26	367.18	20.34	-22.79	32.46	0.00	0.00	0.00	0.00	0.00	0.00	0.00	0.00	0.00
Obturator internus, Gemellus superior & inferior	0.86	-10.42	410.57	11.96	-18.98	20.66	12.43	-36.77	39.19	7.07	-35.18	37.20	2.15	-3.92	4.14
Pectineus	-16.52	-11.14	339.48	0.00	0.00	0.00	0.00	0.00	0.00	1.30	-1.01	1.12	2.38	-1.06	1.32
Vastus medialis	15.54	-21.93	180.83	82.90	-6.10	-259.22	0.00	0.00	0.00	2.93	0.18	-8.09	0.00	0.00	0.00
Vastus intermedius	21.31	-16.80	199.26	0.00	0.00	0.00	0.00	0.00	0.00	9.13	5.01	-62.06	0.00	0.00	0.00
Vastus lateralis	16.70	1.23	217.30	0.00	0.00	0.00	0.00	0.00	0.00	69.58	-25.73	-215.72	0.00	0.00	0.00
Gastrocnemius lateralis	-17.85	26.80	11.43	-22.75	5.96	-52.93	-126.98	21.72	-159.16	-292.75	-37.74	-247.83	-19.04	-3.33	-4.72
Gastrocnemius medialis	-24.70	-24.50	10.28	0.00	0.00	0.00	-6.77	2.30	-8.42	-5.71	0.04	-4.77	0.00	0.00	0.00
Biceps femoris, caput breve	-0.91	-1.59	204.26	-0.10	9.17	-48.81	-4.00	10.97	-60.16	-15.09	11.31	-90.02	-0.64	0.17	-2.21
Adductor magnus caudal	3.59	-27.65	41.85	6.44	-7.45	61.20	0.00	0.00	0.00	0.00	0.00	0.00	0.00	0.00	0.00
Adductor magnus cranial	1.42	-23.97	276.17	30.22	-49.77	63.83	0.00	0.00	0.00	0.00	0.00	0.00	0.00	0.00	0.00
Adductor minimus	7.39	-21.54	174.37	9.53	-20.47	51.26	0.00	0.00	0.00	1.86	-1.90	2.81	11.45	-7.62	13.25
Adductor longus	-3.18	-5.67	216.09	0.00	0.00	0.00	0.00	0.00	0.00	0.00	0.00	0.00	0.40	-0.29	0.26
Adductor brevis 1	-15.62	-6.94	339.59	0.00	0.00	0.00	0.00	0.00	0.00	0.00	0.00	0.00	0.37	-0.28	0.31
Adductor brevis 2	-11.37	-11.32	311.71	0.00	0.00	0.00	0.00	0.00	0.00	0.00	0.00	0.00	0.37	-0.28	0.31
Psoas major, illacus	-12.22	-33.50	370.43	0.00	0.00	0.00	51.47	-24.37	44.32	115.24	-62.89	114.51	32.41	-7.41	20.43

Loading conditions at 10, 30, 45 and 70% gait cycle according to the coordinate system given in the text with x pointing ventrally, y pointing laterally and z pointing proximally.

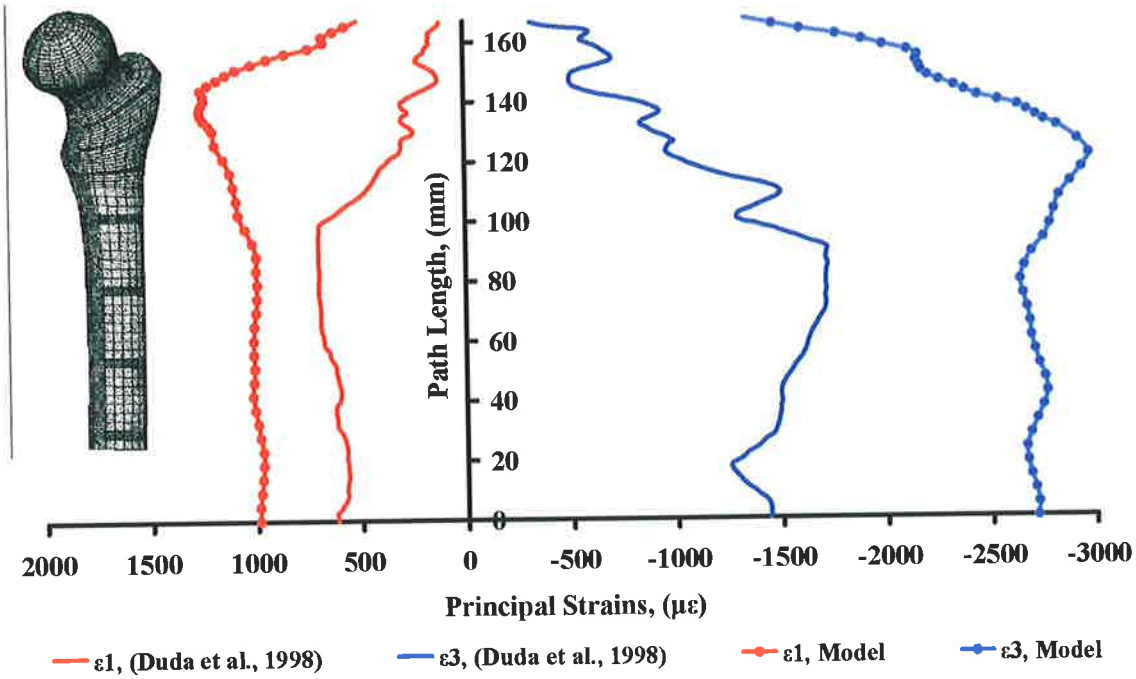


Figure A.1: Comparison of model resultant principal strains along a medial path with those obtained from Duda et al. (1998).

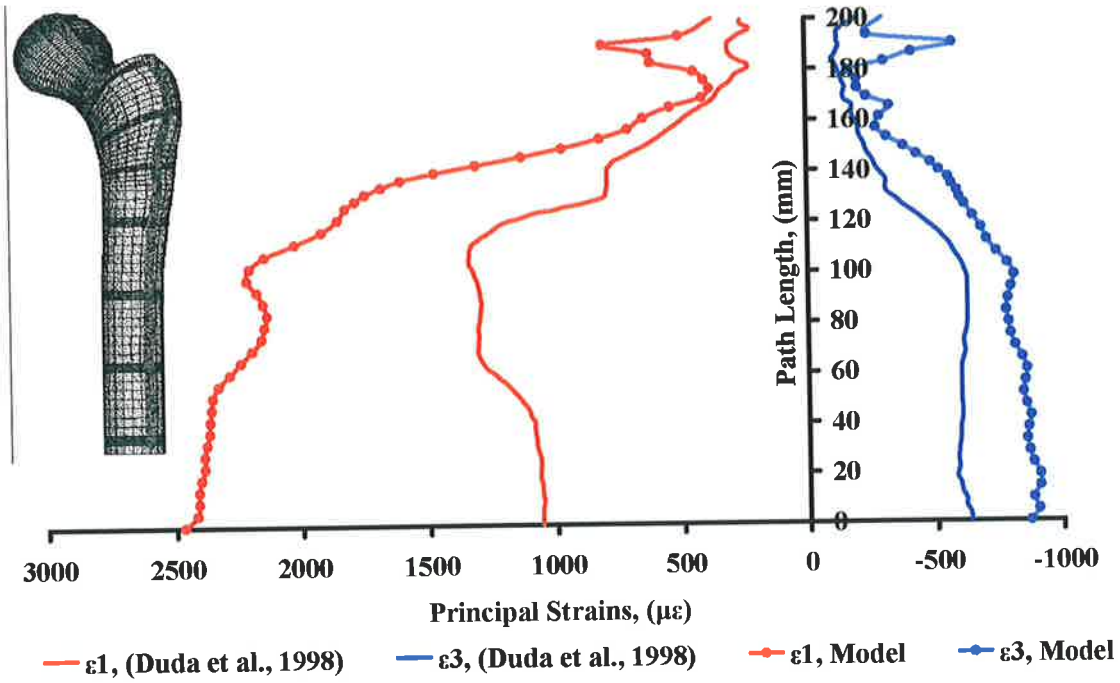


Figure A.2: Comparison of model resultant principal strains along a lateral path with those obtained from Duda et al. (1998).

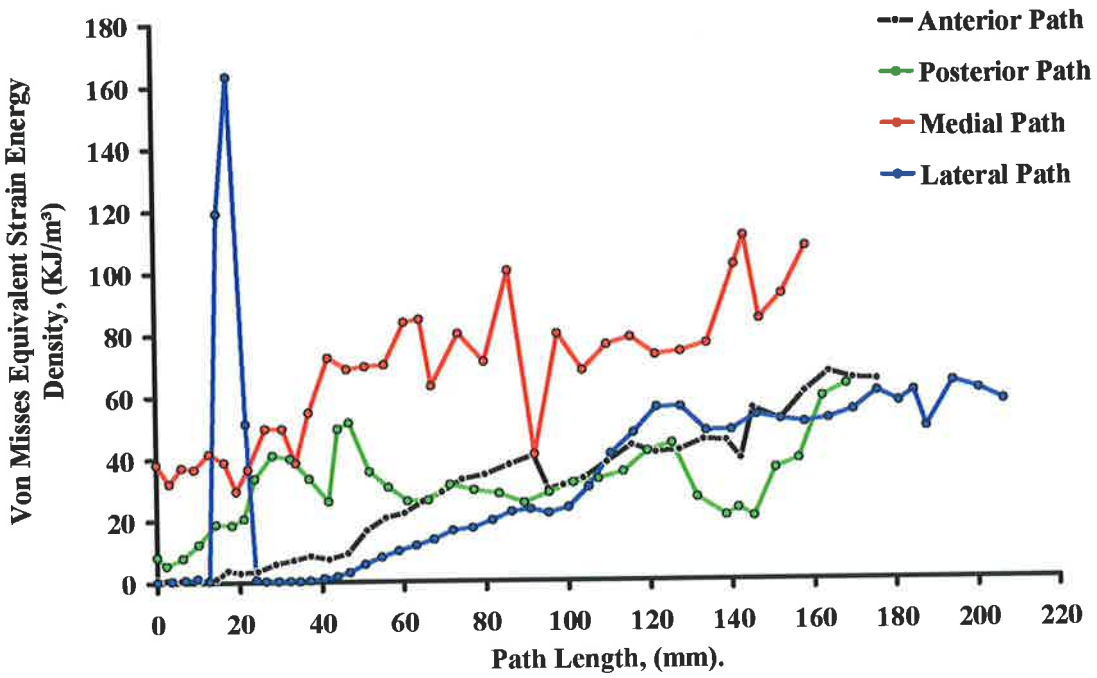


Figure A.3: Von Mise's Equivalent Strain Energy Density along paths of interest for 10 % gait cycle load regime.

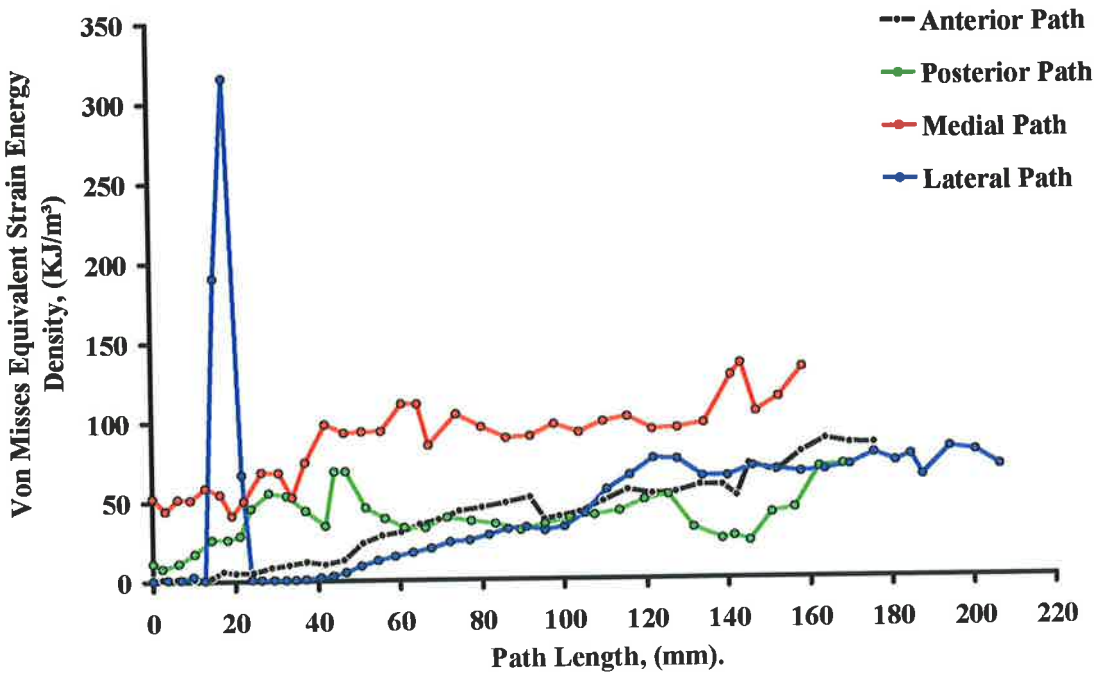


Figure A.4: Von Mise's Equivalent Strain Energy Density along paths of interest for 30 % gait cycle load regime.

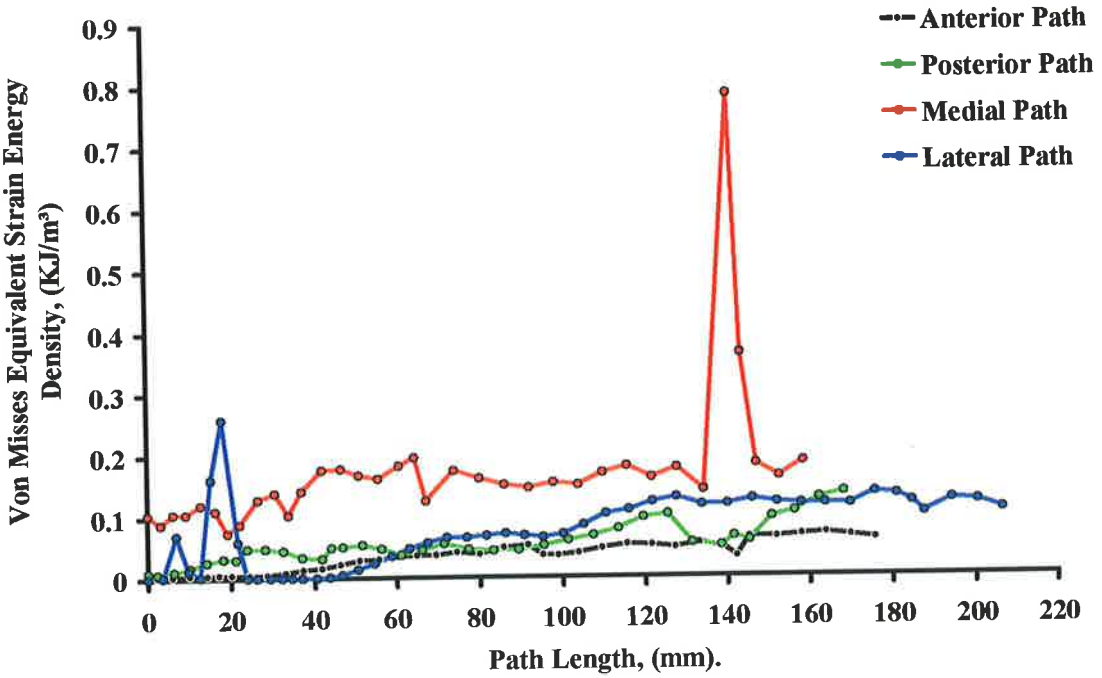


Figure A.5: Von Mise's Equivalent Strain Energy Density along paths of interest for 70 % gait cycle load regime.

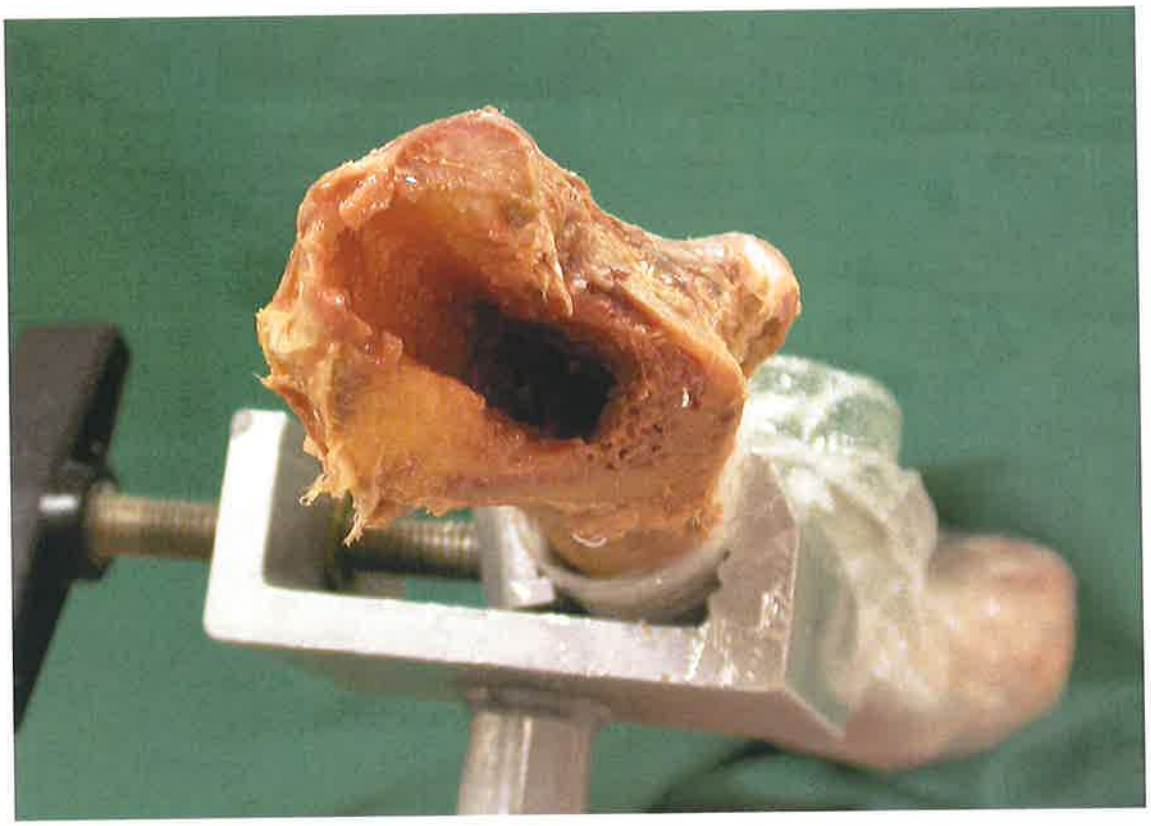


Figure A.6: Preparation of the femoral canal allowing implantation of stem 'A' (the CPT THA stem).



Figure A.7: Cement filling the cavity within the femoral canal.



Figure A.8: Implantation of stem 'B' (the Spectron THA stem).

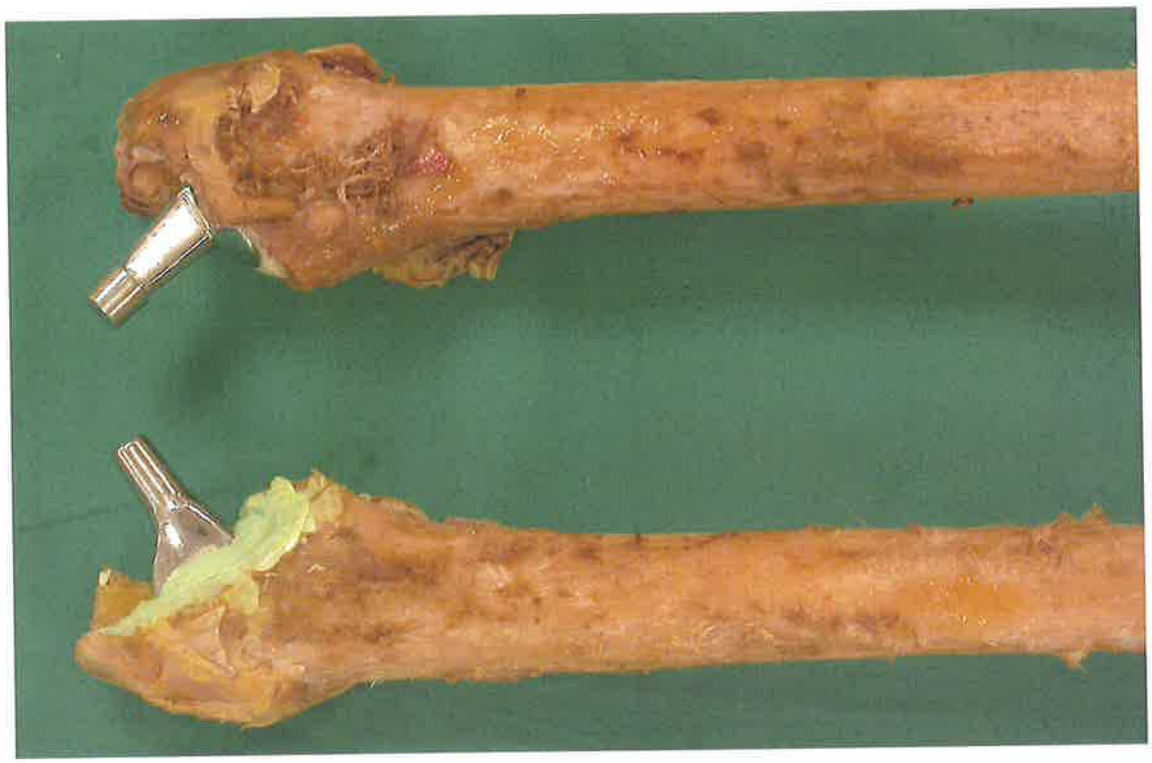


Figure A.9: Implanted cadaveric femora.

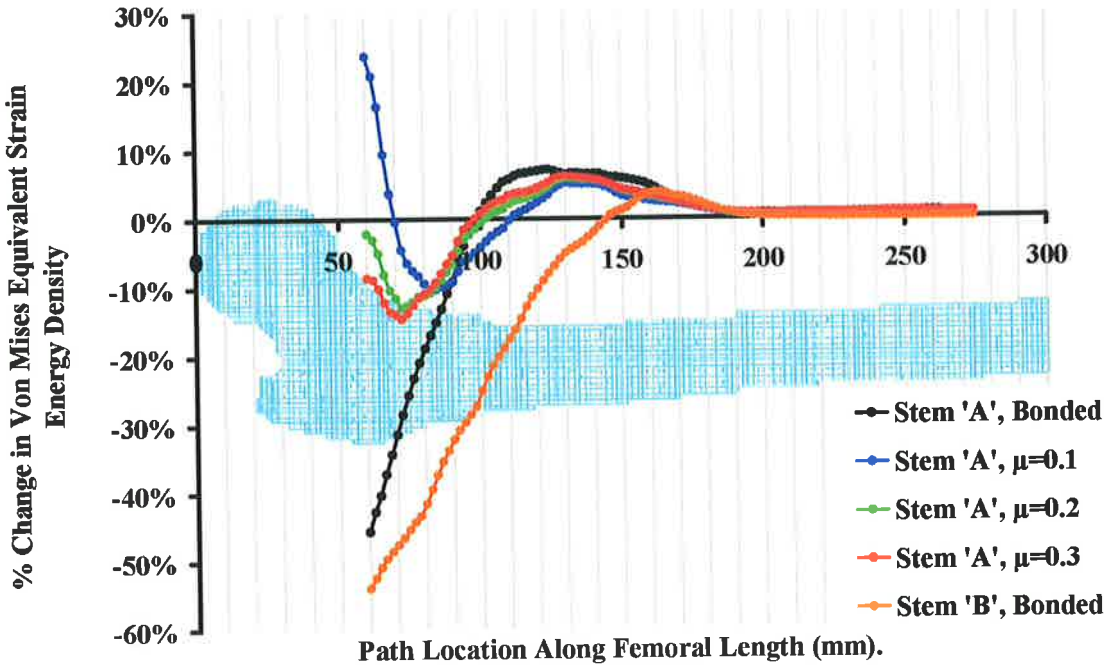


Figure A.10: Comparison of percentage change in Von Mises Equivalent Strain Energy Density distribution along the Anterior path.

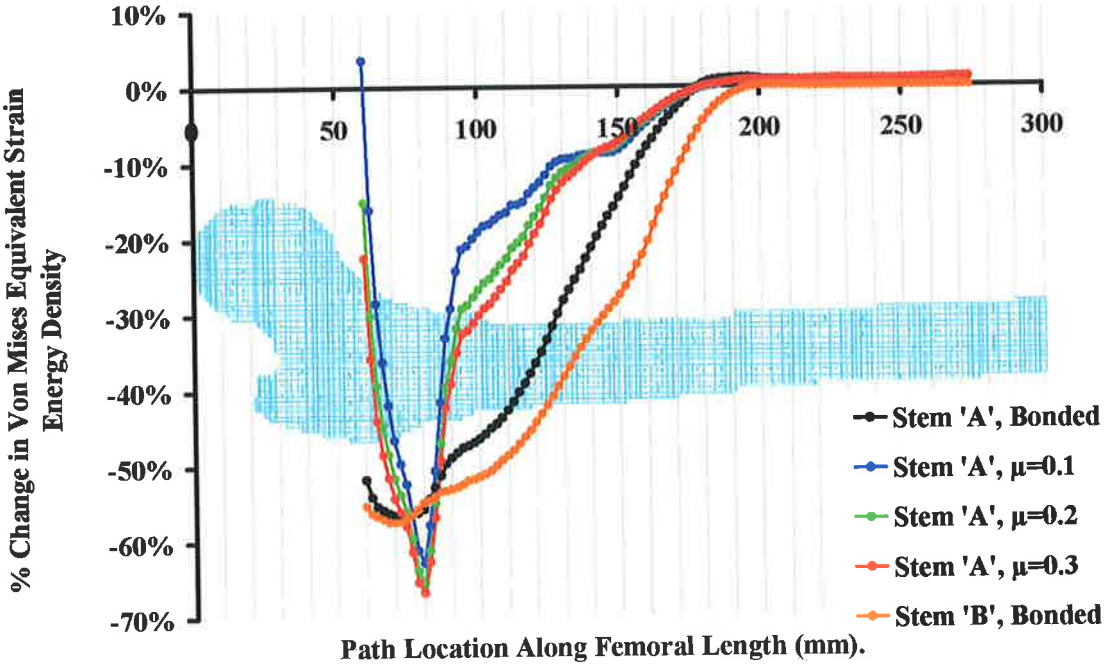


Figure A.11: Comparison of percentage change in Von Mises Equivalent Strain Energy Density distribution along the Posterior path.

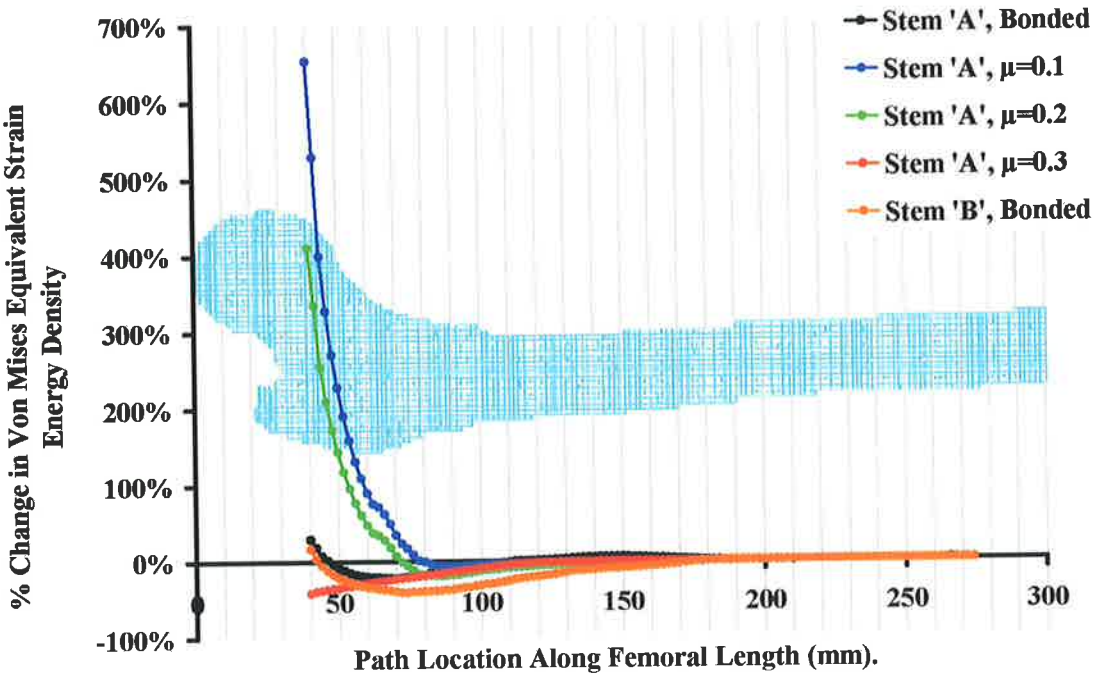


Figure A.12: Comparison of percentage change in Von Mises Equivalent Strain Energy Density distribution along the Lateral path.

Appendix B

ANSYS DESIGN OPTIMISATION

Taken from the ANSYS 7.0 Theory Reference with corrections and additions.

Introduction to Design Optimisation

The optimisation module is an integral part of the ANSYS program that can be employed to determine the optimum design. This optimum design is the best design in some predefined sense. Among many examples, the optimum design for a frame structure may be the one with minimum weight or maximum resonance; in heat transfer, the minimum temperature; or in magnetic motor design, the maximum peak torque. In many other situations minimisation of a single function may not be the only goal, and attention must also be directed to the satisfaction of predefined constraints placed on the design (e.g., limits on stress, geometry, displacement, heat flow).

While working towards an optimum design, the ANSYS optimisation routines employ three types of variables that characterise the design process: design variables, state variables, and the objective function. These variables are represented by scalar parameters in ANSYS Parametric Design Language (APDL). The use of ADPL is an essential step in the optimisation process.

The independent variables in an optimisation analysis are the design variables. The vector of design variables is indicated by:

$$x = [x_1 x_2 x_3 \ldots x_n] \tag{B.1}$$

The independent variables in an optimisation analysis are the design variables. The vector of design variables is indicated by:

$$\underline{x}_i \le x_i \le \bar{x}_i \qquad (i = 1, 2,3,\ldots,n) \tag{B.2}$$

where: n = number of design variables, the under-bar indicates lower bound, and the over-bar indicates the upper bound.

The design variable constraints are often referred to as side constraints and define what is commonly called feasible design space.

Now, minimise

$$f = f(x) \tag{B.3}$$

subject to

$$g_i(x) \le \bar{g}_i \qquad (i = 1,2,3,\ldots m_1) \tag{B.4}$$

$$\underline{h}_i \le h_i(x) \qquad (i = 1,2,3,\ldots m_2) \tag{B.5}$$

$$\underline{w}_i \le w_i(x) \le \bar{w}_i \qquad (i = 1,2,3,\ldots m_3) \tag{B.6}$$

where:

f = objective function,

g_i, h_i, w_i = state variables containing the design, and

$m_1 + m_2 + m_3$ = number of state variables constraints with various upper and lower limit values.

The state variables can also be referred to as dependent variables in that they vary with the vector x of design variables.

Equation B.3 through Equation B.6 represent a constrained minimisation problem whose aim is the minimisation of the objective function f under the constraints imposed by Equation B.2, Equation B.4, Equation B.5, and Equation B.6.

Feasible Versus Infeasible Design Sets

Design configurations that satisfy all constraints are referred to as feasible designs. Design configurations with one or more violations are termed infeasible. In defining feasible design space, a tolerance is added to each state variable limit. So if x° is a given design set defined as

$$x^\circ = [x^\circ_1 x^\circ_2 x^\circ_3 \ldots x^\circ_n] \tag{B.7}$$

The design is deemed feasible only if

$$g_i^\circ = g_i(x^\circ) \leq \bar{g}_i + \alpha_i \qquad (i = 1,2,3,\ldots m_1) \tag{B.8}$$

$$\underline{h}_i - \beta_i \leq h_i^\circ = h_i(x^\circ) \qquad (i = 1,2,3,\ldots m_2) \tag{B.9}$$

$$\underline{w}_i - \gamma_i \leq w_i^\circ = w_i(x^\circ) \leq \bar{w}_i + \gamma_i \qquad (i = 1,2,3,\ldots m_3) \tag{B.10}$$

where: α_i, β_i, and γ_i = tolerances and

$$\underline{x}_i \leq x_i^{\circ} \leq \bar{x}_i \qquad (i = 1, 2, 3, \ldots, n) \qquad \textbf{(B.11)}$$

(since no tolerances are added to design variable constraints)

Equation B.8 to Equation B.11 are the defining statements of a feasible design set in the ANSYS optimisation routines.

The Best Design Set

As design sets are generated by methods or tools and if an objective function is defined, the best design set is computed and its number is stored. The best set is determined under one of the following conditions.

1. If one or more feasible sets exist the best design set is the feasible one with the lowest objective function value. In other words, it is the set that most closely agrees with the mathematical goals expressed by Equation B.3 to Equation B.6.

2. If all design sets are infeasible, the best design set is the one closest to being feasible, irrespective of its objective function value.

Subproblem Approximation Method

This method of optimisation can be described as an advanced, zero-order method in that it requires only the values of the dependent variables (objective function and state variables) and not their derivatives. The dependent variables are first replaced with approximations by means of least squares fitting, and the constrained minimisation problem converted to an unconstrained problem using penalty functions. Minimisation is then performed every iteration on the

approximated, penalised function (called the subproblem) until convergence is achieved or termination is indicated. For this method each iteration is equivalent to one complete analysis loop.

Since the method relies on approximation of the objective function and each state variable, a certain amount of data in the form of design sets is needed. This preliminary data can be directly generated by the user using any of the other optimisation tools or methods. If not defined, the method itself will generate design sets at random.

Function Approximations

The first step in minimising the constrained problem expressed by Equation B.3 to Equation B.6 is to represent each dependent variable by an approximation, represented by the ^ notation. For the objective function,

$$\hat{f}(x) = f(x) + \text{error} \tag{B.12}$$

And similarly for the state variables,

$$\hat{g}(x) = g(x) + \text{error} \tag{B.13}$$

$$\hat{h}(x) = h(x) + \text{error} \tag{B.14}$$

$$\hat{w}(x) = w(x) + \text{error} \tag{B.15}$$

The most complex form that the approximations can take on is a fully quadratic representation with cross terms. Using the example of the objective function,

$$\hat{f} = a_0 + \sum_{i}^{n} a_i x_i + \sum_{i}^{n}\sum_{j}^{n} b_{ij} x_i x_j \qquad \textbf{(B.16)}$$

The actual form of each fit varies from iteration to iteration and are mostly determined by the program, but some user control is available. A weighted least squares technique is used to determine the coefficient, a_i and b_{ij}, in Equation B.16. For example, the weighted least squares error norm for the objective function has the form

$$E^2 = \sum_{j=i}^{n_d} \phi^{(j)} (f^{(j)} - \hat{f}^{(j)})^2 \qquad \textbf{(B.17)}$$

where: $\phi^{(j)}$ = weight associated with design set j, and n_d = current number of design sets.

Similar E^2 norms are formed for each state variable. The coefficients in Equation B.17 are determined by minimising E^2 with respect to the coefficients. The weights used above are computed in one of the following ways:

1. Based on objective function values, where design sets with low objective function values have high weights.

2. Based on design variable values, where the design sets closer to the best design receive high weights.

3. Based on feasibility, where feasible sets have high weights and infeasible sets low weights.

4. Based on a combination of the three weights described above.

5. All weights are unity: $\phi^{(j)} = 1$, for all j.

A certain number of design sets must exist in order to form the approximations; otherwise random designs sets will be generated until the required number is obtained. This can be expressed as

$$\begin{aligned} n_d < n+2 &\rightarrow \text{generates random design variables} \\ n_d \geq n+2 &\rightarrow \text{forms the approximations} \end{aligned} \qquad \textbf{(B.18)}$$

where:

n = number of design variables

n_d = number of design sets

As more data (design sets) is generated, the terms included in Equation B.16 increase.

Minimising the Subproblem Approximation

With function approximations available, the constrained minimisation problem is recast as follows.

Minimise

$$\hat{f} = \hat{f}(x) \qquad \textbf{(B.19)}$$

subject to

$$\underline{x}_i \le x_i \le \bar{x}_i \qquad (i = 1, 2, 3, \ldots, n) \qquad \textbf{(B.20)}$$

$$\hat{g}_i(x) \le \bar{g}_i + \alpha_i \qquad (i = 1, 2, 3, \ldots m_1) \qquad \textbf{(B.21)}$$

$$\underline{h}_i - \beta_i \le \hat{h}_i(x) \qquad (i = 1, 2, 3, \ldots m_2) \qquad \textbf{(B.22)}$$

$$\underline{w}_i - \gamma_i \le \hat{w}_i(x) \le \bar{w}_i + \gamma_i \qquad (i = 1, 2, 3, \ldots m_3) \qquad \textbf{(B.23)}$$

The next step is the conversion of Equation B.19 to Equation B.23 from a constrained problem to an unconstrained one. This is accomplished by means of penalty functions, leading to the following subproblem statement.

Minimise

$$F(x, p_k) = \hat{f} + f_0 p_k \left(\sum_{i=1}^{n} X(x_i) + \sum_{i=1}^{m_1} G(\hat{g}_i) + \sum_{i=1}^{m_2} H(\hat{h}_i) + \sum_{i=1}^{m_3} W(\hat{w}_i) \right) \qquad \textbf{(B.24)}$$

in which X is the penalty function used to enforce design variable constraints; and G, H, and W are penalty functions for state variable constraints. The reference objective function value, f_0, is introduced in order to achieve consistent units. Notice that the unconstrained objective function (also termed a response surface), $F(x, p_k)$, is seen to vary with the design variables and the quantity p_k, which is a response surface parameter. A sequential unconstrained minimisation technique (SUMT) is used to solve Equation B.24 each design iteration. The subscript k above reflects the use of subiterations performed during the subproblem solution, whereby the response surface parameter is increased in value ($p_1 < p_2 < p_3$ etc.) in order to achieve accurate, converged results.

All penalty functions used are of the extended-interior type. For example, near the upper limit, the design variable penalty function is formed as

$$X(x_i) = \left\{ \begin{array}{l} c_1 + c_2/(\bar{x} - x_i) \text{ if } x_i < \bar{x} - \varepsilon(\bar{x} - \underline{x}) \\ c_3 + c_4/(x_i - \bar{x}) \text{ if } x_i \geq \bar{x} - \varepsilon(\bar{x} - \underline{x}) \end{array} \right\} \qquad (i = 1, 2, 3, \ldots, n) \qquad \textbf{(B.25)}$$

where: c_1, c_2, c_3, and c_4 = constants that are internally calculated, and ε = very small positive number.

State variable penalties take a similar form. For example, again near the upper limit,

$$W(w_i) = \left\{ \begin{array}{l} d_1 + d_2/(\bar{w} - \hat{w}_i) \text{ if } \hat{w}_i < \bar{w}_i - \varepsilon(\bar{w}_i - \underline{w}_i) \\ d_3 + d_4/(\hat{w}_i - \bar{w}) \text{ if } \hat{w}_i \geq \bar{w}_i - \varepsilon(\bar{w}_i - \underline{w}_i) \end{array} \right\} (i = 1, 2, 3, \ldots, n) \qquad \textbf{(B.26)}$$

where: d_1, d_2, d_3, and d_4 = constants that are internally calculated, and similarly for G and H.

The SUMT algorithm is employed to reach the minimum unconstrained objective function, $\tilde{F}^{(j)}$, at design iteration j; that is,

$$x^{(j)} \rightarrow \tilde{x}^{(j)} \qquad \text{as} \qquad F^{(j)} \rightarrow \tilde{F}^{(j)} \qquad \textbf{(B.27)}$$

where: $\tilde{x}^{(j)}$ is the design variable vector corresponding to $\tilde{F}^{(j)}$.

The final step performed during each design iteration is the determination of the design variable vector to be used in the next iteration $(j + 1)$. Vector $x^{(j+1)}$ is determined according to the following equation;

$$x^{(j+1)} = x^{(b)} + C(\tilde{x}^{(j)} - x^{(b)}) \quad \textbf{(B.28)}$$

where: $x^{(b)}$ = best design set constants , and

C = internally chosen to vary between 0.0 and 1.0, based on the number of infeasible solutions.

Convergence

Subproblem approximation iterations continue until either convergence is achieved or termination occurs. These two events are checked only when the current number of design sets, nd, equals or exceeds the number required for the approximations (see Equation B.18).

Convergence is assumed when either the present design set, $x^{(j)}$, or the previous design set, $x^{(j-1)}$, or the best design set, $x^{(b)}$, is feasible; and one of the following conditions is satisfied.

$$\left|f^{(j)} - f^{(j-1)}\right| \leq \tau \quad \textbf{(B.29)}$$

$$\left|f^{(j)} - f^{(b)}\right| \leq \tau \quad \textbf{(B.30)}$$

$$\left|x_i^{(j)} - x_i^{(j-1)}\right| \leq \rho_i \qquad (i = 1, 2, 3, \ldots, n) \quad \textbf{(B.31)}$$

$$\left|x_i^{(j)} - x_i^{(b)}\right| \leq \rho_i \qquad (i = 1, 2, 3, \ldots, n) \quad \textbf{(B.32)}$$

where: τ and ρ_i = objective function and design variable tolerances.

Equation B.29 and Equation B.30 correspond to differences in objective function values; Equation B.31 and Equation B.32 to design variable differences.

If satisfaction of Equation B.29 to Equation B.32 is not realised, then termination can occur if either of the below two conditions is reached.

$$n_s = N_s \tag{B.33}$$

$$n_{si} = N_{si} \tag{B.34}$$

where:

n_s = number of subproblem iterations,

n_{si} = number of sequential infeasible design sets,

N_s = maximum number of iterations, and

N_{si} = maximum number of sequential infeasible design sets.